UNIVERSITÀ DEGLI STUDI DI PADOVA

DIPARTIMENTO DI TECNICA E GESTIONE DEI SISTEMI INDUSTRIALI
CORSO DI LAUREA MAGISTRALE IN INGEGNERIA MECCATRONICA

TESI DI LAUREA MAGISTRALE

IL SOVRACAMPIONAMENTO DELLE CORRENTI PER IL CONTROLLO DI MOTORI ELETTRICI IN ALTERNATA

-

CURRENT OVERSAMPLING ANALYSIS FOR ADVANCED CONTROL OF ELECTRIC AC DRIVES

Relatore: Ch.mo Prof. Mauro Zigliotto

Correlatore: Ch.mo Prof. Luca Peretti
(KTH Royal Institute of Technology - Stockholm)

Laureando: Marco Giuliato
1163258-IMC

ANNO ACCADEMICO: 2018-19

Considerate la vostra semenza:
fatti non foste a viver come bruti,
ma per seguire virtute e canoscenza

Dante

C'é una giusta misura nelle cose, ci sono giusti confini al di qua e al di lá dei quali non puó sussistere ció che é retto.

–

Est modus in rebus, sunt certi denique fines quos ultra citraque nequit consistere rectum.

Orazio

A tutti coloro che,
con il loro amore, ogni giorno
mi incoraggiano e sostengono.

Marco Giuliato

SOMMARIO

Lo scopo principale di questa tesi è quello di sviluppare un controllo sensorless per un motore sincrono a riluttanza utilizzando la misurazione della pendenza del ripple di corrente introdotto dalla Space Vector Modulation. La stima della posizione viene eseguita ad ogni periodo di SVPWM e si basa sulla stima delle derivate di corrente, la quale viene effettuata utilizzando una regressione ricorsiva ai minimi quadrati (RLS), che è stata implementata su un FPGA, sulle correnti sovracampionate a 10 MHz.

Sono stati sviluppati due diversi osservatori di posizione: il primo si basa sul calcolo delle derivate di corrente durante il tempo di applicazione più lungo di un singolo vettore di tensione di SVPWM. Il secondo, invece, è un osservatore indipendente dalla resistenza elettrica del motore, ma che richiede la stima delle derivate di corrente durante due diversi vettori di tensione.

Le prestazioni dell'algoritmo di stima ai minimi quadrati e degli osservatori di posizione sono stati analizzate sia in simulazione che mediante test sperimentali a velocità diverse, durante variazioni di velocità e con una coppia di carico applicata.

La principale fonte di errore della stima di posizione sono le oscillazioni di corrente ad alta frequenza, che impediscono una stima accurata delle derivate di corrente. Queste oscillazioni sono dovute alla commutazione degli IGBT e alla presenza di elementi parassiti nel cavo, nell'inverter e nel motore. Poichè tali oscillazioni sono presenti subito dopo le commutazioni, la stima delle derivate di corrente è stata ritardata di alcuni μs al fine di ridurre l'errore di stima. Tuttavia, tale tecnica riduce la finestra temporale durante la quale viene eseguita la regressione lineare, riducendo così la sua precisione.

Pertanto, è stato condotto uno studio più approfondito sulle cause e gli effetti delle oscillazioni ad alta frequenza ed è stato sviluppato un modello dell'azionamento, in cui sono stati considerati anche gli elementi parassiti, utilizzando *Matlab Simscape.*

ABSTRACT

The main purpose of this thesis is to develop a sensorless control for a synchronous reluctance motor by using the slope measurement of the current ripple introduced by the Space Vector Modulation.

The position estimation is performed at each Space Vector Pulse Width Modulation period and it relies on the estimation of current derivatives.

The current derivative estimation was carried out using a recursive least squares regression (RLS), which was implemented on an FPGA, on the currents oversampled at 10 MHz.

Two different position observers were developed: the first is based on the calculation of current derivatives during the longest application time of a single SVPWM voltage vector. The second, instead, is an observer independent of the electrical resistance of the motor, but which requires the current derivatives estimation during two different voltage vectors.

The RLS regression algorithm and position observers performances were analysed both in simulation and by experimental tests at different speeds, during speed variations and with applied load torque.

The main source of position estimation errors are the high-frequency current oscillations, which prevent an accurate estimation of current derivatives. These oscillations are due to IGBT switching and to the presence of parasitic elements in the cable, in the inverter and in the motor.

Since these oscillations are present just after a switch commutation, the estimation of current derivatives has been delayed by some μs in order to reduce the estimation error. However, this technique reduces the time window during which the linear regression is performed, thus reducing its precision.

Therefore, a more in-depth study was carried out on the causes and effects of high frequency oscillations, and a model of the drive, in which the parasitic elements were also considered, was realized using *Matlab Simscape.*

SAMMANFATTNING

Det huvudsakliga syftet med denna examensarbete är att utveckla en sensorlös regulator för en synkron reluktansmotor medelst mätningar av derivatan/lutningen hos strömripplet som introduceras vid användandet av s.k. space-vector-pulsbreddsmodulering (SVPWM). Positionsberäkningen utförs varje SVPWM-period och förlitar sig på uppskattningen av strömderivatan. Strömderivatberäkningen utfördes med en rekursiv minsta kvadratmetod (RLS), som implementerades på en FPGA, på strömmar som översamplades vid 10 MHz.

Två olika positionsobservatörer utvecklades: den första baseras på beräkningen av strömderivator under den SVPWM-spänningsvektor vars enskilda appliceringstid är längst. Den andra är istället en observatör som är oberoende av maskinlindningens resistans, men som å andra sidan kräver att strömderivatan uppskattas utifrån två olika spänningsvektorer.

RLS-regressionsalgoritmen och positionsobservatörernas prestanda utvärderades genom såväl simuleringar som experimentella tester vid olika hastigheter, hastighetsvariationer och med applicerat lastvridmoment. Den huvudsakliga källan till positionsuppskattningsfel är högfrekventa strömoscillationer, som förhindrar en exakt beräkning av strömderivatorna. Dessa oscillationer beror på på- och avkoppling av växelriktar-IGBTerna och på förekomsten av parasitiska element i växelriktaren, maskinen och kabeln däremellan.

Eftersom oscillationerna är närvarande strax efter en switchkommutering fördröjs uppskattningen av strömderivatan med några μs för att minska uppskattningsfelet. Denna teknik minskar emellertid tidsfönstret under vilket den linjära regressionen utförs, vilket i sin tur minskar dess precision.

Därför genomfördes en mer djupgående studie av orsakerna till och effekterna av högfrekventa oscillationer och en modell av frekvensomriktaren, där de parasitiska elementen också beaktades, realiserades i *Matlab Simscape*.

ACKNOWLEDGEMENTS

I would sincerely like to thank my primary supervisor, Professor Mauro Zigliotto, who has guided me throughout this work with availability and transmitting me passion for the subject. I would also like to thank my co-supervisor, Professor Luca Peretti, who gave me the opportunity to complete my thesis at the KTH Royal Institute of Technology, and my examiner at KTH Professor Oskar Wallmark. I would also like to thank my friends Dott. Ing. Fabio Tinazzi, Dott. Ing. Ludovico Ortombina, Ing. Dario Pasqualotto within the UNIPD-EDLAB group and Ing. Giovanni Zanuso within the KTH-EMaDLab group, who have been a source of help with advices, encouragement and friendly conversations during all my MsC thesis period. Finally, I would like to thank my girlfriend, my family and all my friends who have been fundamental and very supportive through all my study period.

CONTENTS

Appendix

LIST OF FIGURES

LIST OF TABLES

LISTINGS

ACRONYMS

LVO	Longest Vector Observer
SynRM	Synchronous Reluctance Motor
SVPWM	Space Vector Pulse Width Modulation
RSIO	Resistance and Speed Independent Observer
PMSM	Permanent Magnet Synchronous Motor
IPM	Internal Permanent Magnet Synchronous Motor

1

INTRODUCTION

1.1 BACKGROUND

The Synchronous Reluctance Motor (SynRM) motors has been developed since the first decades of the XX century, although nowadays its usage is still very limited, as Induction Motors and Permanent Magnet Synchronous Motor (PMSM) are more used. In fact, nowadays PMSM are preferred, thanks to their high power density and efficiency. However, this type of motors requires the procurement of magnetic materials, which are made of rare earths, whose extraction has a very high environmental impact. Moreover, the uneven distribution of rare earths makes their market and availability subject to strong fluctuations, generating a serious issue for companies that produce and/or use electric motors. Furthermore, the continuous increase in the consumption of electricity and the global emissions of greenhouse gases that is taking place in these years, is causing a increasing environmental damage. In order to reduce this issue, the European Union legislation is pushing to increase the efficiency of electrical motors. The SynRM is an interesting alternative which has characteristics compatible with both these issues, i.e. they do not require magnets but they have a high efficiency (the most recent SynRMs have an efficiency of 90% or more, depending on the size of the motor) [1].

In order to implement efficient drives using synchronous electrical motors, a closed loop control is required, for which the rotor position information is needed. The rotor position can be measured using resolvers and encoders, which nowadays can have very high resolution and accuracy. Anyway, these components are very expensive and often require additional electronic circuitry, then increasing the cost of the whole drive, and they are sensitive to mechanical stress, reducing the drive's robustness and reliability, especially in harsh environmental conditions.

To eliminate these drawbacks, sensorless control techniques has been developed, which estimate the position using particular algorithms starting from the measurement of electrical quantities, eliminating the need of a mechanical position sensor. In this way, the drive's cost can be reduced or the position measurement can be made redundant, thus increasing the reliability of the drive: an example of a block diagram for a sensorless control system is reported in figure 1.1. Such techniques rely on observers, which can be divided in two main categories:

- the open-loop observers, which use only the electrical measurements to estimate the rotor position;

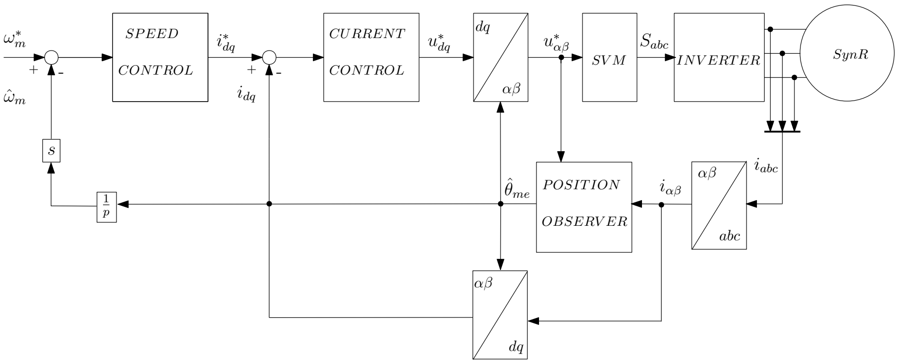

Figure 1.1: Sensorless control schematic.

- the closed-loop observers, in which, at each step of the discrete-time control system, the position and speed estimations are entered into a model which, reproducing the electrical system, derives the expected values of quantities that are measured. The comparison of these latter variables with their estimated values is used to correct the position estimation at the next step, by means of a regulator.

The sensorless control techniques are based on two different types of electrical phenomena directly related to the position, which are:

- magnetic salience (i.e. the spatial distribution of inductance seen from non-uniform stator phases) in anisotropic motors or due to saturation in isotropic ones;
- induced voltage (bemf = back-electromotive force).

Then, for the synchronous reluctance motors the magnetic salience techniques are used, which can be realized using the Fundamental PWM excitation or the high frequency signal injection. The first is based on the analysis of the current response to the voltage vectors applied in a Space Vector Pulse Width Modulation (SVPWM) period, while the second type of techniques injects voltage or current signals to exploit the position information [2][3]. Anyway, the main drawbacks of these sensorless techniques are their lower estimation bandwidth in comparison to encoders, the machine's parameter dependency of some observers, and the bandwidth reduction of the current controller required by some injection-based methods.

In order to eliminate these drawbacks, in recent years, various researches on the development of sensorless techniques based on the use of current oversampling in electric drives have been carried out. It consists of sampling the current several times in a SVPWM period, thus at a higher frequency in comparison to the regular sampling used for normal control. Different results have been achieved and some of them have never been realized in practice. Most of these techniques have been applied only to Internal Permanent Magnet Synchronous Motor (IPM) or

PMSM, and only in few cases using the Fundamental PWM technique. Nowadays the costs and the complexity of the hardware involved are prohibitive for industrial production, however the increasing number of publications and the possible future developments of these techniques may lead to a reduction of these costs.

1.2 RELATED WORKS

Current oversampling has been proposed for the first time using Rogovski - type current derivative sensors by Wolbank et al. [4],[5] in 2010, analysing switching transients to capture the machine winding recharge. In a later publication [6] the anisotropy information obtained from the current derivatives was used to obtain the rotor position, but it has not been realized a closed-loop sensorless control. In 2011, the Rogovski - type current derivative sensors were used even by Bolognani et al. [7], who proposed to average multiple high frequent samples in order to reduce the noise introduced by the high frequency oscillations due to the inverter's parasitic elements, but still a quite high injection magnitude was required. Moreover, both above approaches are based on current derivative sensors, i.e. additional expensive hardware with respect to a conventional drive setup.

The Least Squares approximation to a straight line of the oversampled current signals has been proposed by Sumner et al. [8] in 2012, using the current derivative estimation to obtain the anisotropy information. Anyway, the proposed estimating technique was too much affected by the high frequency oscillations during active voltage vectors of reasonable injection magnitudes, making it impossible to obtain a correct position estimation. Guan et al.[9], in 2014, used a sliding mode observer for joint stator flux and rotor speed estimation at all speeds: at low speeds, the sliding mode observer was enhanced by the fundamental PWM excitation technique, which is used to correct the direction of flux vector estimate of the observer. In the same year Landsmann [3] proposed a technique, based on Arbitrary Injection, that, at low speed, exploited the anisotropy of the inductance reconstructing the current slope during the Active Switching States (ASS) from the Passive Switching States (PSS) information. At high speed, indeed, the bemf orientation was used to estimate the rotor position in a parameter-free way from the PSS current slope, obtained from the ASS coefficients.

In Landsmann's work, a Recursive Least Square regression was used to estimate the current derivatives and the high frequency oscillations were avoided delaying the start of the linear fitting. However, when the PWM pulse width was too short to obtain a good current derivative estimation during average active vector, it was estimated approximating it to a straight line from the start and end points of the current in adjacent null vectors.

Due to the difficulties of obtaining correct measurements of the current

derivatives, in 2013 Sumner et al. [10] and Hind in 2015 [11] replaced the RLS estimation using an Artificial Neural Network (ANN). The oversampled current data during the ASS are used to estimate the ripple slope in a more precise and reliable way: the position estimation precision is increased, but at the cost of a much greater implementative and computational effort. In the end, Weber et al. in 2017 [12] presented a reduced observer, based on a least mean squares regression of the current samples during the inverter's passive switching states, to estimate the current slopes during active voltage vectors and using them for position estimation.
All the above mentioned researches implemented sensorless techniques for IPM or PMSM, except that Landsmann in [3], who proposed a hybrid sensorless control scheme for the SynRM based on a stabilized flux estimator, obtaining although an observer with a low bandwidth. Moreover all the presented techniques relied on the measurement of the current derivatives during two or three vectors of the SVPWM. Anyway, It is impossible to estimate the current derivative during voltage vectors too short, i.e. when pulse width violations occur at low voltage references and when crossing SVPWM boundaries. Then, in order to overcome the acquisition issues due to short application times of voltage vector, the above mentioned techniques required different strategies, which are a PWM modification, an high frequency injection or the reconstruction of missing current derivatives from the start and endpoints of current samples in adjacent vectors.

1.3 PROPOSED TECHNIQUES AND THESIS OBJECTIVES

This thesis aims to develop a position observer for a reluctance motor using current oversampling, performed using a 10 MHz ADC and a FPGA to perform a Recursive Least Square regression, approximating the current ripple to a straight line. Two different position observers are developed, both based on the Fundamental PWM technique, using the analytical relationship between electrical measurements, stator-frame inductances and rotor position.
The first observer uses these measurements to exploit the position estimation during the application of the longest of the three vectors applied during a SVPWM period. This vector is chosen because, having a longer analysis time, it is more likely that the estimation will converge, thus obtaining values of the current derivatives less affected by high frequency disturbances. The main drawback of this observer is that it requires the knowledge of the electrical resistance and of the estimated electro-mechanical speed $\hat{\omega}_{me}$. The second observer realizes the position estimation comparing the current derivative response to two different space vectors, during a SVPWM period, and is independent from the electric resistance. However, this observer needs two vectors to be long enough to correctly estimate the current derivatives.

In this work a particular focus is made on the current derivatives measurement: the current evolution during every Space Vector Modulation switching state is linearly approximated (neglecting the resistive term in the motor's equations), and the slope of the linear current ripple (i.e. the approximated current derivative) is estimated. Moreover, the high frequency oscillations of the phase currents, due to the parasitic elements of the inverter, prevent the convergence of the current slopes' estimation to the correct value. To avoid this problem, the relationship between these oscillations and the switching elements is carefully analysed and two different solutions are proposed.

The first solution was to delay the beginning of the RLS regression after the decay of the oscillation, however reducing the regression time window, while the second solution was based on filtering the high frequency oscillation, causing a position estimation's delay. In figure 1.2 are reported the problems and motivations underlying the work carried out in this thesis.

In conclusion, the distinctive features of this work are the absence of any high-frequency current injection or PWM modification, the use of a recursive least square algorithm, on data obtained using standard current sensors, the use of the longest voltage vectors applied at each SVPWM period. As an implementation hint, all of the three phase currents are measured, in order to increase the accuracy of the position estimation.

1.4 THESIS OVERVIEW

After this introduction, the second chapter describes the synchronous reluctance machine model and the current oversampling based technique. The position observer equations are obtained starting from the motor model. In Chapter 3 the simulations used to develop the current derivatives estimation and the sensorless control algorithms are reported. In Chapter 4, the hardware setup designed for this thesis is described and the experimental results are reported. In particular, the main differences between simulative and experimental results are analysed, and the different sensorless techniques are compared. Chapter 5 focuses on the current ripple analysis and investigates a more accurate way to estimate the current derivatives. In the end, the conclusions are reported in Chapter 6 and possible future studies are proposed.

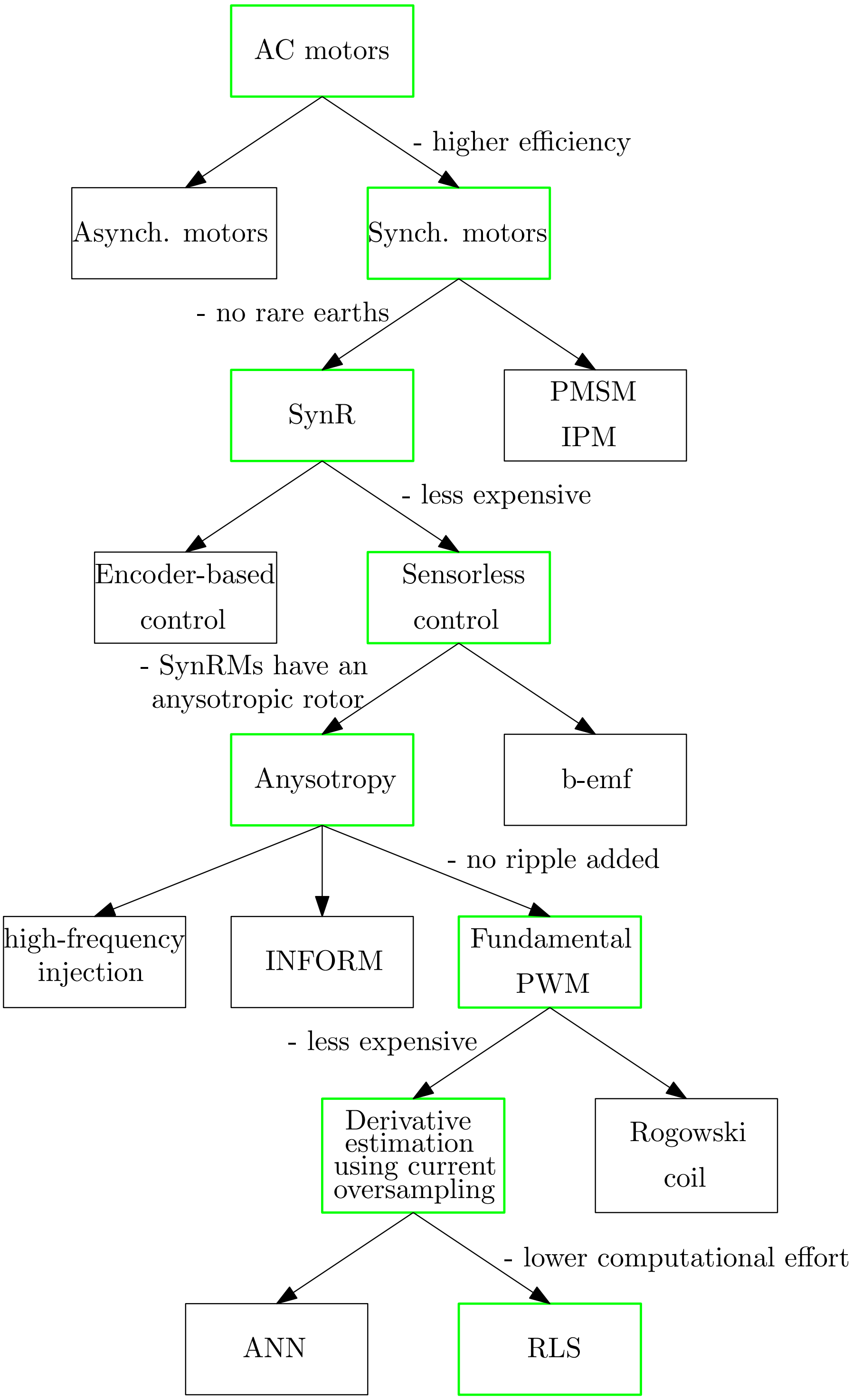

Figure 1.2: Flow chart of this thesis motivations.

2

THEORETICAL INTRODUCTION

2.1 SYNCHRONOUS RELUCTANCE MOTORS

2.1.1 *Introduction*

Nowadays, SynR motors are becoming increasingly used in the industrial sector, thanks to recent studies that are leading to an improvement in their performance. One of the main advantages of using SynR motors is that they don't have magnets, avoiding procurement of permanent magnetic materials issues, such as their availability, price fluctuation and environmental impact for extraction. In fact, the rare earth market is predominantly from China, which satisfies the world's needs for rare earths and possesses 48% of world reserves. This causes a strong variability in the prices of permanent magnets and their availability. Furthermore, rare earth mines often contain radioactive elements such as uranium and thorium. The rare earth veins produce around a million tons of sewage (figure 2.1), mostly acid or radioactive, almost all untreated, every year [13].
The other main reason why the number of SynR motors used in industrial applications is increasing it is their high efficiency, which can be greater than 90%. Indeed, about 45% of the electric power produced worldwide is directly consumed by electric motors, of which around 90% are three-phase induction motors. As a result, the global effort to reduce energy use and greenhouse gas emissions can be significantly implemented with the use of high efficiency electric motors. Moreover, the directive (2012/24 / EC), issued by EU legislators, which requires industrial engines to have an efficiency compliant with the latest IEC 60034 - 30 efficiency standards, established by the International Electrotechnical Commission, contributed to increment the diffusion of SynR motors.

Figure 2.1: Pipes pouring polluted water from a rare earth smelting plant dump.

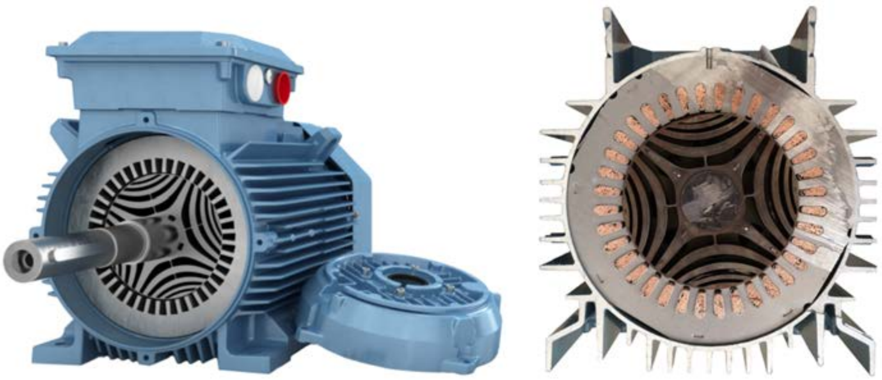

Figure 2.2: SynRM produced by ABB and SynRM section. Courtesy of [1].

Indeed, the most recent SynRMs, although they require more current than permanent magnets synchronous motors, are becoming in many applications a viable alternative to the induction motor, which are inadequate to meet the European directive's efficiency standards.

2.1.2 *Structure and operating principle* [1]

The SynRM exploits the principle of reluctance systems for torque generation. Basically, it is based on the variation of magnetic energy stored as a function of the reciprocal position of an anisotropic stator-rotor system. The stator's structure is identical to that of an induction motor, as shown in figure 2.2. In the stator there are three windings, whose conductors are arranged in such a way as to produce a cosinusoidal magnetic flux in the air gap, if supplied with three sinusoidal voltages phase-shifted respectively by $\frac{2}{3}\pi$ between them. The rotor is instead made up of an anisotropic structure, without magnets and windings. The rotor salience is obtained with the introduction of internal flux barriers, consisting of holes, which direct the magnetic flux along the direct axis. Generally, there are three main types of rotor structures, as shown in figure 2.3. The first structure is called salient pole (*salient pole rotor*) and is derived removing material in the cross sections (reported in figure 2.3 (a)). The axial laminated rotor or ALA rotor (*axially laminated anisotropic rotor*) is the second type of rotor structure. This consists of laminations packs of ferromagnetic material with interposed aluminium sheets having a thickness of 1-5 mm, of appropriate size and shape, arranged parallel (axially) to the rotor shaft. Depending on how the laminations are shaped, rotors are obtained with a different number of polar pairs p. The resulting pile of lamellas is connected to the central region, which in turn is coupled to the shaft, through the polar supports (reported in figure 2.3 (b)). In the third type of rotor, called *transversally laminated anisotropic rotor*, lamination is conventional

---

[1] This paragraph is mainly the translation of part of [1], with the permission of the Author.

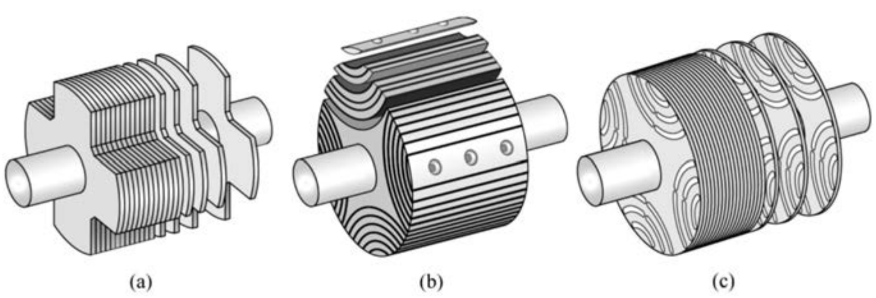

Figure 2.3: Main types of rotor: (a) Rotor with salient poles (SP), (b) Rotor with axial lamination (ALA), (c) Transverse lamination rotor (TLA). Courtesy of [1].

and the laminations are specially drilled so as to create flux barriers (air). The latter are then stacked on top of each other in a direction perpendicular to the axis of the rotor (shown in figure 2.3 (c)). The development of rotor structure design focuses on the transversally laminated one, as it is more suited to industrial production, involves less iron losses than other types and, moreover, its very simple structure leads it to be overall cheaper also of the induction motor, in perspective.

2.1.3 *Mathematical model of the SynR motor*

The stator equations in natural coordinates can be expressed directly in vector form, in general, as follows:

$$\boldsymbol{u}_{abc}(t) = \boldsymbol{R}\boldsymbol{i}_{abc}(t) + \frac{d\boldsymbol{\lambda}_{abc}(t)}{dt} \tag{2.1}$$

where $\boldsymbol{R}$ is the diagonal matrix of the stator resistances and the vectors of the voltages, currents and fluxes are defined as follows:

$$\boldsymbol{u}_{abc}(t) = \begin{bmatrix} u_a(t) \\ u_b(t) \\ u_c(t) \end{bmatrix}; \quad \boldsymbol{i}_{abc}(t) = \begin{bmatrix} i_a(t) \\ i_b(t) \\ i_c(t) \end{bmatrix}; \quad \boldsymbol{\lambda}_{abc}(t) = \begin{bmatrix} \lambda_a(t) \\ \lambda_b(t) \\ \lambda_c(t) \end{bmatrix} \tag{2.2}$$

In general, each flux is a non-linear function of time, stator currents and of the rotor position. To express the actual quantities according to a synchronous reference system ($dq0$) rotating with the rotor, a complete matrix relation can be used, which uses the transformation matrix of coordinates $\boldsymbol{T} = \boldsymbol{T}_{abc/dq0}$, reported here for convenience:

$$\boldsymbol{T} = \frac{2}{3}\begin{bmatrix} cos(\theta_{me}) & cos(\theta_{me} - 2\pi/3) & cos(\theta_{me} - 4\pi/3) \\ -sin(\theta_{me}) & -sin(\theta_{me} - 2\pi/3) & -sin(\theta_{me} - 4\pi/3) \\ 1/\sqrt{2} & 1/\sqrt{2} & 1/\sqrt{2} \end{bmatrix} \tag{2.3}$$

Multiplying left 2.1 by 2.3 we have:

$$\begin{aligned}\boldsymbol{u}_{dq0} &= \boldsymbol{R}\boldsymbol{i}_{dq0} + \boldsymbol{T}\frac{d(\boldsymbol{T}^{-1}\boldsymbol{\lambda}_{dq0})}{dt} \\ &= \boldsymbol{R}\boldsymbol{i}_{dq0} + \frac{d\boldsymbol{\lambda}_{dq0}}{dt} + \boldsymbol{T}\frac{d(\boldsymbol{T}^{-1})}{dt}\boldsymbol{\lambda}_{dq0}\end{aligned} \tag{2.4}$$

where

$$\boldsymbol{\lambda}_{dq0} = \begin{bmatrix}\lambda_d(t)\\ \lambda_q(t)\\ \lambda_0(t)\end{bmatrix} \; ; \quad \boldsymbol{T}\frac{d\boldsymbol{T}^{-1}}{dt} = \begin{bmatrix}0 & -\omega_{me} & 0\\ \omega_{me} & 0 & 0\\ 0 & 0 & 0\end{bmatrix} \tag{2.5}$$

By breaking down equation 2.4 into the three components, the following system is obtained, which describes the dynamics of the synchronous reluctance motor even in presence of saturation:

$$\begin{aligned} u_d &= Ri_d + \frac{\lambda_d}{dt} - \omega_{me}\lambda_q \\ u_q &= Ri_q + \frac{\lambda_q}{dt} + \omega_{me}\lambda_d \\ u_0 &= Ri_0 + \frac{\lambda_\sigma}{dt}\end{aligned} \tag{2.6}$$

Through a simple energy balance, in conservative system hypothesis, it is possible to obtain the following torque equation:

$$\tau = \frac{3}{2}p(\lambda_d i_q - \lambda_q i_d) \tag{2.7}$$

The peculiarity of the expressions 2.6 and 2.7 is that no specific relationship between the magnetic flux linkage and current has been assumed. It should also be noted that the torque does not depend on the component i_0, therefore usually the third equation in 2.6 is abandoned and the usual notation of space vectors can be used again for voltages, currents and fluxes:

$$\boldsymbol{u}_{dq} = u_d + ju_q; \quad \boldsymbol{i}_{dq} = i_d + ji_q; \quad \boldsymbol{\lambda}_{dq} = \lambda_d + j\lambda_q \tag{2.8}$$

The voltages balance, which can be obtained directly from the first two equations of 2.6, becomes, in compact vector form:

$$\boldsymbol{u}_{dq} = R_s\boldsymbol{i}_{dq} + \frac{d\boldsymbol{\lambda}_{dq}}{dt} + j\omega_{me}\boldsymbol{\lambda}_{dq} \tag{2.9}$$

The equivalent electrical circuit is shown in Figure 2.4. The variable inductance $\boldsymbol{L}_{dq}$ is actually a matrix. It is only a way to graphically represent the flux vector generation by the current vector.

The choice of the orientation of the synchronous reference system (d, q) with respect to the rotor anisotropy remains an open discussion. Deriving a SynRM from an anisotropic permanent magnet motor (IPM), the d axis remains the original one, and it follows that $L_d < L_q$.

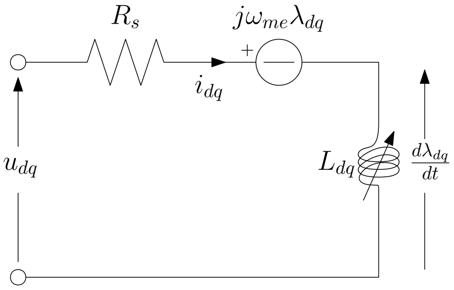

Figure 2.4: Equivalent electrical circuit of a SynR motor.

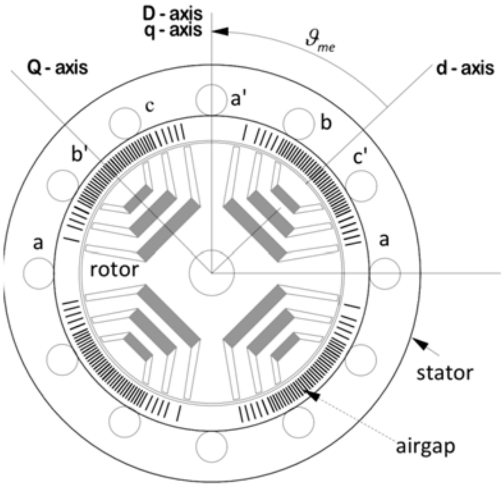

Figure 2.5: Possible choices of orientation of the reference system in a transversal rolling rotor. [14]

Instead, if we consider the SynR autonomously, follow the concept of placing the D-axis aligned with that of the main flow, i.e. the one with the minimum reluctance, then the new system (D, Q) is translated counter-clockwise by $\frac{\pi}{2}$ compared to the previous system, as reported in figure 2.5, while in figure 2.6 the flux lines of the d and q axis fluxes are reported. In this discussion the first convention will be adopted, i.e. the d-axis as in an IPM motor, with $L_d < L_q$.

Since part of the magnetic paths is common both to the direct axis and to the quadrature axis flux, the saturation of these portions of ferromagnetic material, due to one of the two currents, causes flux variations also on the other axis, although the current on this axis remains constant. This phenomenon is called $cross - saturation$. Consequently, as already mentioned, the linkage fluxes are non-linear functions $(\boldsymbol{f}_{dq})$ of the currents :

$$\boldsymbol{\lambda}_{dq} = \boldsymbol{f}_{dq}(\boldsymbol{i}_{dq}) = [\lambda_d(i_d, i_q) + j\lambda_q(i_d, i_q)] \tag{2.10}$$

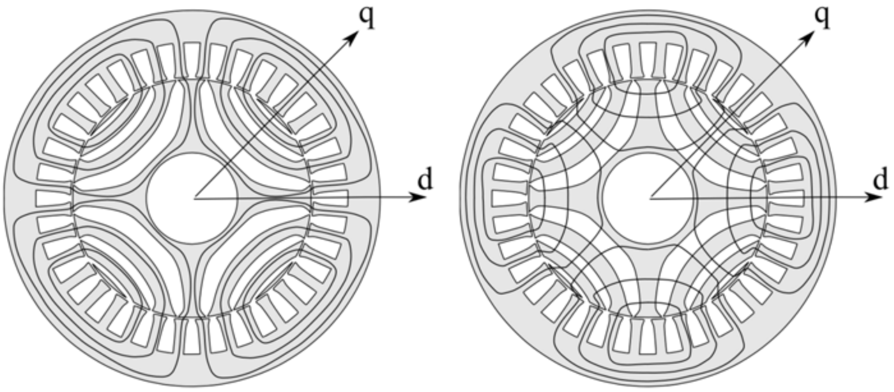

Figure 2.6: Sketch of a synchronous reluctance motor with (a) d–axis flux lines and (b) q–axis flux lines. [14]

For completeness, is also referred to below the definition of Jacobian matrix $\boldsymbol{L}_{dq}$ associated with the function $\boldsymbol{f}_{dq}$:

$$\boldsymbol{L}_{dq} = \begin{bmatrix} L_d^{diff} & L_{dq}^{diff} \\ L_{dq}^{diff} & L_q^{diff} \end{bmatrix} = \begin{bmatrix} \frac{\partial\lambda_d}{\partial i_d} & \frac{\partial\lambda_d}{\partial i_q} \\ \frac{\partial\lambda_q}{\partial i_d} & \frac{\partial\lambda_q}{\partial i_q} \end{bmatrix} \tag{2.11}$$

where the differential inductances have been made explicit.

The observers implemented in this thesis work use the mathematical model of the SynR motor in the stationary reference systems $\alpha\beta$, which will be hereafter presented. Moreover the cross-coupling inductances and the effect of magnetic iron saturation is neglected for seek of simplicity. These neglects introduce a higher position estimation error when the motor works in saturation conditions, e.g. heavy load conditions, and in cross-coupling areas; further studies will may consider these aspects and introduce corrections to the observers described in the following paragraphs. However, considering the linear inductances L_d and L_q and neglecting the cross-saturation, the expression of L_{dq} 2.11 can be rewritten in the following way:

$$\boldsymbol{L}_{dq} = \begin{bmatrix} L_d & 0 \\ 0 & L_q \end{bmatrix} \tag{2.12}$$

then equation 2.10 becomes :

$$\boldsymbol{\lambda}_{dq} = \boldsymbol{L}_{dq}\boldsymbol{i}_{dq} \tag{2.13}$$

and the resulting motor's equation 2.4 is:

$$\boldsymbol{u}_{dq} = \boldsymbol{R}\boldsymbol{i}_{dq} + \boldsymbol{L}_{dq}\frac{d\boldsymbol{i}_{dq}}{dt} + \boldsymbol{T}\frac{d(\boldsymbol{T}^{-1}\boldsymbol{L}_{dq})}{dt}\boldsymbol{i}_{dq} \tag{2.14}$$

Figure 2.7 shows the block diagram of the SynR motor, derived using the equations 2.12 and 2.14.

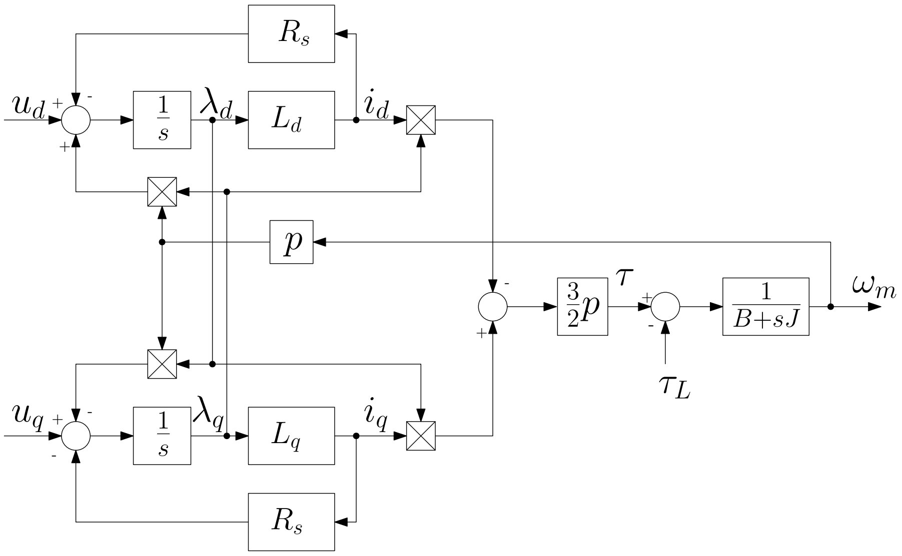

Figure 2.7: Block diagram of the SynR motor.

In the stationary reference system $\alpha\beta$, the motor model can be written in vectorial form as follows:

$$\boldsymbol{u}_{\alpha\beta} = R\boldsymbol{i}_{\alpha\beta} + \frac{d\boldsymbol{\lambda}_{\alpha\beta}}{dt} \tag{2.15}$$

where the magnetic flux due to the stator currents can be written as:

$$\boldsymbol{\lambda}_{\alpha\beta} = \boldsymbol{L}_{\alpha\beta}\boldsymbol{i}_{\alpha\beta} \tag{2.16}$$

Replacing 2.16 in 2.15 we obtain:

$$\boldsymbol{u}_{\alpha\beta} = R\boldsymbol{i}_{\alpha\beta} + \frac{d\boldsymbol{L}_{\alpha\beta}}{dt}\boldsymbol{i}_{\alpha\beta} + \boldsymbol{L}_{\alpha\beta}\frac{d\boldsymbol{i}_{\alpha\beta}}{dt} \tag{2.17}$$

The matrix $\boldsymbol{L}_{\alpha\beta}$ can be obtained by considering that 2.13 can be expressed in the reference system $\alpha\beta$ using the transformation matrix $\boldsymbol{T}_{\alpha\beta/dq}$

$$\boldsymbol{T}_{\alpha\beta/dq} = \begin{bmatrix} cos(\theta_{me}) & sin(\theta_{me}) \\ -sin(\theta_{me}) & cos(\theta_{me}) \end{bmatrix} \tag{2.18}$$

multiplying both members of the equation 2.13 as follows:

$$\boldsymbol{T}_{dq/\alpha\beta}\boldsymbol{\lambda}_{dq} = \boldsymbol{T}_{dq/\alpha\beta}\boldsymbol{L}_{dq}\boldsymbol{i}_{dq} \tag{2.19}$$

obtaining

$$\boldsymbol{\lambda}_{\alpha\beta} = \boldsymbol{T}_{dq/\alpha\beta}\boldsymbol{L}_{dq}\boldsymbol{T}_{\alpha\beta/dq}\boldsymbol{i}_{\alpha\beta} \tag{2.20}$$

From the comparison of equation 2.20 and 2.16, we get:

$$\boldsymbol{L}_{\alpha\beta} = \boldsymbol{T}_{dq/\alpha\beta}\boldsymbol{L}_{dq}\boldsymbol{T}_{\alpha\beta/dq} \tag{2.21}$$

Carrying out all the matrix products and defining the following two inductances :

$$L_\Sigma = \frac{L_q + L_d}{2}\,;\;\; L_\Delta = \frac{L_q - L_d}{2} \tag{2.22}$$

the following inductance matrix is obtained:

$$\boldsymbol{L}_{\alpha\beta} = \begin{bmatrix} L_\Sigma - L_\Delta cos(2\theta_{me}) & -L_\Delta sin(2\theta_{me}) \\ -L_\Delta sin(2\theta_{me}) & L_\Sigma + L_\Delta cos(2\theta_{me}) \end{bmatrix} \tag{2.23}$$

Finally, substituting 2.23 in 2.15 and explicating the α and β components, we obtain:

$$\begin{cases} u_\alpha = R\, i_\alpha + \dfrac{di_\alpha}{dt}\,(L_\Sigma - L_\Delta\, cos(2\theta_{me})) - L_\Delta\,\dfrac{di_\beta}{dt}\, sin(2\theta_{me}) + \\ \qquad - 2\, L_\Delta\, cos(2\theta_{me})\, i_\beta\, w_{me} + 2\, L_\Delta\, i_\alpha\, sin(2\theta_{me})\, w_{me} \\ u_\beta = R\, i_\beta + \dfrac{di_\beta}{dt}\,(L_\Sigma + L_\Delta\, cos(2\theta_{me})) - L_\Delta\,\dfrac{di_\alpha}{dt}\, sin(2\theta_{me}) + \\ \qquad - 2\, L_\Delta\, cos(2\theta_{me})\, i_\alpha\, w_{me} - 2\, L_\Delta\, i_\beta\, sin(2\theta_{me})\, w_{me} \end{cases} \tag{2.24}$$

which is the motor's linear model in stator-frame reference system $\alpha\beta$, used to derive the observers' equations.

2.2 SENSORLESS CONTROL

2.2.1 *Introduction*

The purpose of sensorless algorithms is to obtain a position estimation starting from the measurements of the electrical quantities, as DC-voltage and phase currents, which are always available for current control and for safety reasons. In this way, it is possible to remove the mechanical position sensors, i.e. encoder and resolver: it is from this removal that the *sensorless* name derives. The removal of these sensors reduces the cost of the drive and increases fault tolerance, as mechanical sensors are subject to electrical and mechanical stress. In position estimation algorithms both voltage and current measurements can be used, and in some cases also the current derivatives. Normally, the various sensorless techniques have different preferential operating regions, i.e. zero or low speed and medium-high speed, according to the physical principle on which they are based. As reported previously in figure 1.1, in synchronous motors the estimated position is used both for current and speed control, which can be estimated directly from the sensorless algorithm or obtained by derivation of the estimated position.
The various sensorless control techniques available today can be further divided into two groups, according to the type of motor on which they can be applied. For motors with an isotropic rotor they are based on the recognition of the counter-electromotive force, which depends on

the position of the rotor. However, these techniques fail to estimate the position at low speeds, since the induced bemf is too small. Instead, for anisotropic rotor motors, sensorless algorithms use the injection of voltages or currents in the stator winding, thus using the motor itself as a position transducer. The possible excitation modes are called *rotating* or *pulsating flux*, and, from the acquisition of the currents, informations on the inductance of the stator phases are obtained and from them the rotor position, contained within the inductances matrix $L_{\alpha\beta}$, is deduced. Anyway all the motor's non idealities, like inductances' saturation, non-sinusoidally distributed windings, slotting effects and stator asymmetries, cause position estimation error, reducing in this way the observers' accuracy, and could even lead to instability if not correctly considered.

The work presented in this thesis uses a synchronous reluctance motor, with a highly anisotropic rotor, therefore only the saliency-based techniques are considered. An alternative method to the injection of high frequency signals is to extract the information on motor's anisotropy, and therefore on the rotor's position, from the high frequency current ripple introduced by the PWM modulation. This method can be implemented with two different techniques: the first, called Indirect Flux Detection by Online Reactance Measurement (INFORM), is based on the addition of voltage pulses of opposite sign, during the application of null vectors. The second technique, called Fundamental PWM technique, instead uses only the frequency signals introduced by the normal SVPWM vector modulation. In fact, the voltage pulses generate a current ripple closely related to the $\boldsymbol{L}_{\alpha\beta}$ inductances, from which it is therefore possible to extract the information on the position, without modifying in any way the current control of the motor or the vector modulation. Theoretically, with the use of this technique, it is possible to estimate the rotor position both at low and high speeds. In this thesis it has been chosen to implement a sensorless control based on the Fundamental PWM technique, in order not to introduce any torque ripple due to the injection of current or voltage signals. Furthermore, it was decided to measure the current derivatives by estimating the slope of the ripple using a recursive least squares regression on the oversampled current measurements, so as not to have to add Rogowski sensors, which would increase the drive's price and circuit complexity.

2.2.2 *Current derivatives estimation*

The Fundamental PWM technique uses the mathematical relation between the rotor position and the derivative of the current ripple due to the standard SVPWM. To obtain the current derivative, Rogowski coils can be used, which produce a voltage proportional to the derivative of the current flowing through their section. Even if this type of sensor is very accurate, it is expensive and requires additional electronic circuitry. A cheaper way to measure the current derivatives is to calculate them analytically, using a fitting of the current samples with the theoretical current ripple trend. In order to do that, many current samples are required for each voltage vector applied during a PWM period. In the next paragraphs, the spatial vector of the current ripple will be analysed, which is affected by the chosen modulation technique. Moreover the high frequency oscillations, introduced by the IGBTs switching, and the ripple distortions, due to the inverter's dead times, will be described.

2.2.2.1 *Theoretical current ripple analysis* [2]

For the current ripple analysis it's assumed that, for a motor connected to a converter, the following generic voltage vector equation can be written:

$$\boldsymbol{u} = R\boldsymbol{i} + L\frac{d\boldsymbol{i}}{dt} + \boldsymbol{e} \tag{2.25}$$

where $\boldsymbol{e}$ is the spatial vector of counter-electromotive force, L and R are respectively equivalent inductance and motor phase resistance, $\boldsymbol{u}$ and $\boldsymbol{i}$ the spatial vector of voltage and current of the motor. In a discrete-time voltage control system, as in the space vector modulation, T_c is the switching period.

If the resistive term is neglected, for the seek of simplicity, the trajectory of the current space vector is immediately found by direct integration:

$$\boldsymbol{i}(t) = \frac{1}{L}\int_0^t (\boldsymbol{u}(\tau) - \boldsymbol{e}(\tau))\,d\tau\,,\; 0 \leq t \leq T_c \tag{2.26}$$

The generation of the supply voltage is carried out using a vector modulator, which creates the reference vector as the mean, in T_c, of three state vectors. Therefore, to the average component $\bar{\boldsymbol{u}}$ a component $\tilde{\boldsymbol{u}}$ is added, which has zero mean on T_c. The equation 2.26 can then be rewritten as:

$$\boldsymbol{i}(t) = \frac{1}{L}\int_0^t (\bar{\boldsymbol{u}}(\tau) - \boldsymbol{e}(\tau))\,d\tau + \frac{1}{L}\int_0^t \tilde{\boldsymbol{u}}(\tau)d\tau = \bar{\boldsymbol{i}} + \tilde{\boldsymbol{i}} \tag{2.27}$$

In 2.27 it has been assumed that the counter-electromotive force $\boldsymbol{e}$ is not affected by the voltage harmonics related to the switching frequency of the vector modulation and therefore that it has no alternate components. The current components $\bar{\boldsymbol{i}}$ and $\tilde{\boldsymbol{i}}$ are those produced by the voltages $\bar{\boldsymbol{u}}$ and $\tilde{\boldsymbol{u}}$, respectively. However, it must be emphasized that the average of the component $\tilde{\boldsymbol{i}}$ depends on the modulation technique adopted, and therefore does not necessarily have a zero mean value, even if the voltage producing it has this characteristic.

An example of the trajectory of the ripple space vectors of $\tilde{\boldsymbol{u}}$ and $\tilde{\boldsymbol{i}}$ for

---

[2] This paragraph is mainly the translation of part of [1], with the permission of the Autor.

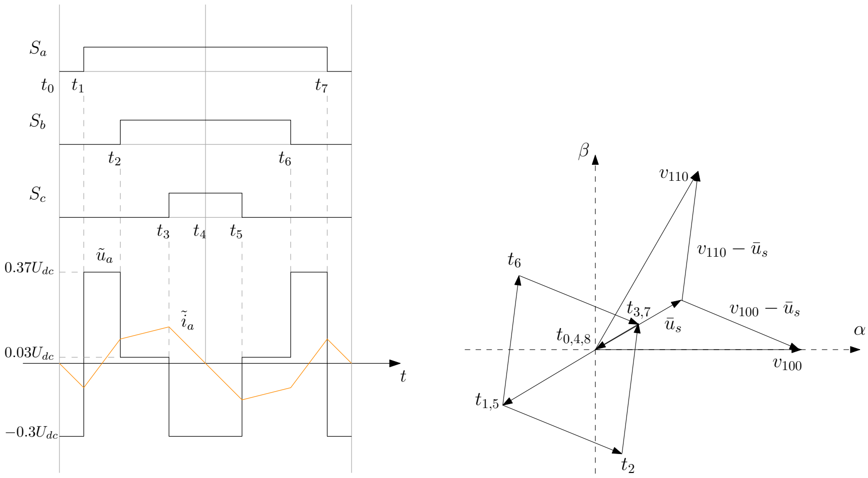

(a) (b)

Figure 2.8: 2.8a Symmetrical SVM and ripple on phase a, 2.8b trajectory of the space vector of the ripple of current.

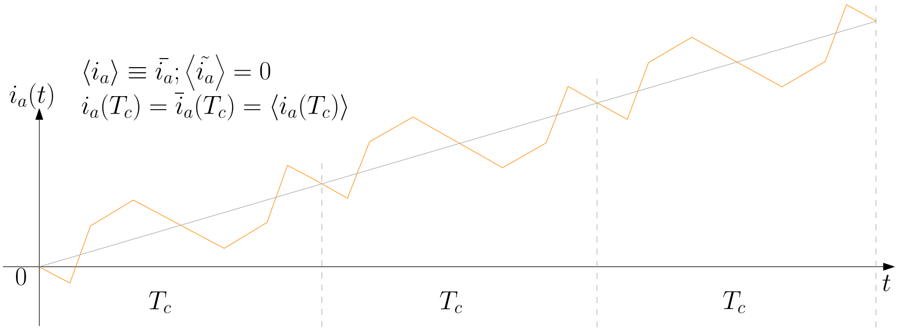

Figure 2.9: Phase current, symmetrical modulation.

the symmetric modulation technique is reported in figure 2.8, considering a duty cycle $\delta_1 = 0.2$ for the state vector v_{100} and $\delta_2 = 0.5$ for the state vector v_{110}. The trajectory of the current vector $\tilde{\boldsymbol{i}}$ is plotted using the equation 2.27, which implicitly indicates that its trend is equal to that of $\tilde{\boldsymbol{u}}$ divided by $\frac{1}{L}$. It can be noticed that the current vector $\tilde{\boldsymbol{i}}$ runs through a cycle composed of two mirror parts, because a symmetrical space vector modulation is used, therefore the current ripple is mirror symmetrical. However, the macroscopic evolution of each phase current consists of the increments (linear within T_c) of $\bar{\boldsymbol{i}}$ due to $\bar{\boldsymbol{u}}$ (constant in T_c), to which are added the variations of $\tilde{\boldsymbol{i}}$, which are alternated by the symmetric and average non-zero modulation for single-sided modulation: figure 2.9 summarizes what is outlined.

The fact that $\tilde{\boldsymbol{i}}$ is zero at the ends of the sampling period derives directly from the fact that $\tilde{\boldsymbol{u}}$ has, by construction, zero mean. In fact, during the $k-th$ of the N intervals in which the period T_c is subdivided according to the chosen modulation technique, the vector $\tilde{\boldsymbol{u}}_k$ is applied, and the relative variation of the current vector, on the basis

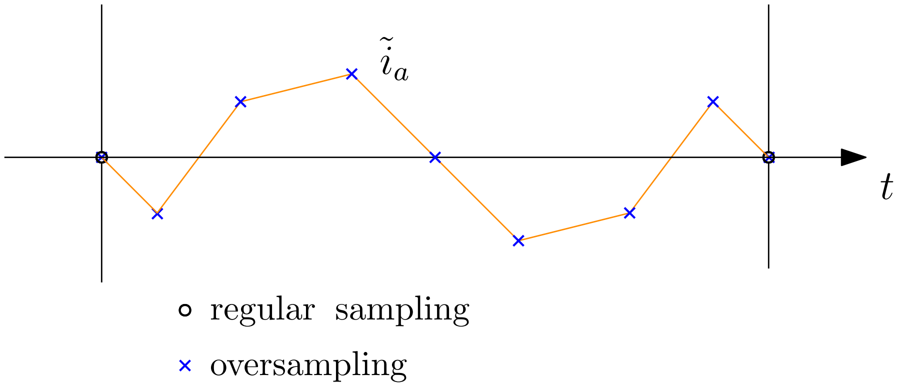

Figure 2.10: PWM with regular sampling and oversampling.

of the equation 2.27, is calculated as $\frac{1}{L}\tilde{\boldsymbol{u}}_k\Delta T_k$. The total variation of current $\Delta\tilde{\boldsymbol{i}}$ in T_c is then:

$$\begin{aligned}
\Delta\tilde{\boldsymbol{i}} &= \sum_{k=1}^{N} \Delta\tilde{\boldsymbol{i}}_k \\
&= \sum_{k=1}^{N} \left(\frac{1}{L}\tilde{\boldsymbol{u}}_k\Delta T_k\right) = \frac{T_c}{L}\sum_{k=1}^{N}\frac{\tilde{\boldsymbol{u}}_k\Delta T_k}{T_c} \qquad (2.28)\\
&\triangleq \frac{T_c}{L}\left\langle\tilde{\boldsymbol{u}}\right\rangle
\end{aligned}$$

Given that at the beginning of each sampling period $\tilde{\boldsymbol{i}} = 0$, the average value of each phase current can be acquired directly through a synchronous sampling with modulation. This is an important result and widely used in industrial practice, because it allows to avoid the interposition of low-pass filters in the acquired current signal, necessary if the overlapping ripple has to be eliminated.

2.2.2.2 *Current oversampling*

With this approach, data sampling is synchronized with PWM pulses and this technique is known as *regular sampling*: *oversampling* therefore means sampling with a higher frequency, in order to obtain further information about the current ripple. Theoretically, it is possible to obtain the approximated coefficients of the linear current evolution during each switching state using the current samples measured at the end of the voltage vectors. A comparison between normal sampling and oversampling is reported in figure 2.10.

The approximation by means of a line of the current evolution during each switching state will provide two coefficients: the offset and the slope, which can be assumed as the current derivative, needed for the position estimation algorithms. Anyway, the current samples are subject to noise due to the measurement quantization, EMC disturbances and to the presence of high frequency oscillations caused by the parasitic elements of the drive. Consequently, the measured current evolution is much different from the theoretical one reported in figure 2.9,

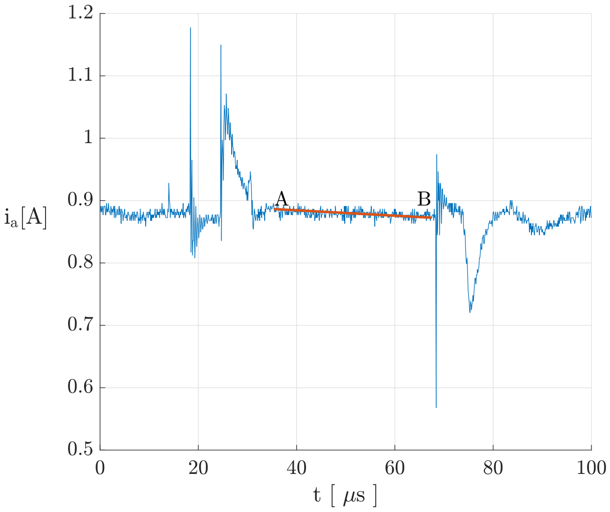

Figure 2.11: Sampled phase current, symmetrical modulation.

and the current derivatives cannot be measured by a simple interpolation of the current samples at the beginning and at the end of the switching periods. An example of the current samples obtained with a sampling frequency of 10 MHz during a PWM period is reported in figure 2.11. In this figure, segment $\overline{AB}$ is the current stretch during the longest application time of a voltage vector, whose ripple is estimated. The current derivative estimation beginning is delayed of $6\mu s$ after the application of the longest voltage vector, to let the high-frequency oscillations decay, thus improving the estimation accuracy. In this picture the high frequency oscillations can be observed: a more in-depth study of these disturbances will be carried out in Chapter 5.

Due to these disturbances, the current derivatives can be estimated using a linear Least-Squares (LS) regression on the oversampled current-time pairs measured during each voltage vector. In this way the current derivatives estimation error, due to the aforementioned disturbances, is reduced and the position observers accuracy is improved.
In order to elaborate the oversampled data measured at a high sample rate (which in our experimental setup is 10 MHz), an FPGA is needed. To reduce the computational effort, the LS regression is implemented in a recursive way, i.e. using a Recursive Least Square (RLS) regression, which is described in the next paragraph. Moreover, in order to reduce the noise introduced by the high frequency oscillations, in this work the RLS was delayed after the decay of these current harmonics. Anyway, thanks to further studies, these oscillations could be eliminated with mathematical methods, allowing to perform a better current derivative estimation.

2.2.2.3 *Recursive Least Squares regression*

Let's consider the quantity y, which depends in a known way on n unknown parameters according to the following linear regression model:

$$y = \phi_1(x)\alpha_1 + \phi_2(x)\alpha_2 + ... + \phi_n(x)\alpha_n \tag{2.29}$$

where ϕ_j, with $j = 1, ..., n$, are known functions of the variable x and α_j are unknown parameters. Equation 2.29 constitutes a model that describes the quantity y. Let's assume now that we have N noisy measures of y:

$$y_k = \phi_1(x_k)\alpha_1 + \phi_2(x_k)\alpha_2 + ... + \phi_n(x_k)\alpha_n + e_k \quad k = 1, ..., N \tag{2.30}$$

where e_k can be interpreted as the model error. The *least squares estimation* problem is to determine the coefficients α_j by solving the following minimization problem:

$$\underset{\alpha_j}{min} V = \underset{\alpha_j}{min} \sum_{k=1}^{N} e_k^2 \tag{2.31}$$

Approximating the current evolution i as a straight line, as reported in the previous paragraph, we can consider a 2 parameters case (i.e. estimating the current slope and offset), rewriting then equation 2.29 in the following way:

$$f(x) = \alpha_1 x + \alpha_0 = y \tag{2.32}$$

and than we have:

$$e^2 = \sum_{k=1}^{N}(y_k - f(x_k))^2 = \sum_{k=1}^{N}(y_k - \alpha_1 x_k - \alpha_0) \tag{2.33}$$

Imposing the conditions

$$\begin{aligned} \frac{\partial e^2}{\partial \alpha_1} &= 0 \\ \frac{\partial e^2}{\partial \alpha_0} &= 0 \end{aligned} \tag{2.34}$$

we finally obtain (with the mathematical reported in A.1):

$$\alpha_1 = \frac{\sum_{k=1}^{N}(x_k y_k - \overline{xy})}{\sum_{k=1}^{N}(x_k^2 - \bar{x}^2)} \tag{2.35}$$

However, the standard LS regression equation 2.35 can be computed only at the end of each voltage vector, i.e. after all necessary data have

been collected. This means that all the samples must be stored, thus requiring a large memory, and elaborated all together at the end of every PWM period. In order to eliminate these drawbacks, the Recursive Least Squares regression equation is derived from 2.35.
Replacing the generic variable y with the current i in the equation 2.29, we can write:

$$i = \frac{di}{dt} \cdot t + i_0 \tag{2.36}$$

and equation 2.30 becomes:

$$i_k = \frac{di_k}{dt} \cdot t + i_{0,k} + e_k \tag{2.37}$$

After some mathematical steps reported in A.1, we obtain the current derivative estimation formula:

$$\frac{\hat{di}}{dt} = \frac{\overline{i \cdot t} - \bar{i} \cdot \bar{t}}{\overline{t^2} - \bar{t}^2} \tag{2.38}$$

In our experimental setup the sample time T_c is constant, so we have:

$$t_k = T_c \cdot k \tag{2.39}$$

with $k = 1, ..., N$, where N is the sample number. Using the following equations:

$$\begin{aligned}
\bar{t} &= \frac{1}{N} \sum_{k=1}^{N} t_k = \frac{1}{N} \sum_{k=1}^{N} T_c \cdot k = \frac{1}{N} T_C \sum_{k=1}^{N} k = \frac{1}{N} T_c \frac{N(N+1)}{2} \\
&= \frac{T_c(N+1)}{2} \\
\overline{t^2} &= \frac{1}{N} \sum_{k=1}^{N} t_k^2 = \frac{T_c^2(N+1)(2N+1)}{6} \\
\bar{i} &= \sum_{k=1}^{N} i_k \\
\overline{i \cdot t} &= \frac{1}{N} \sum_{k=1}^{N} i_k \cdot t_k = \frac{T_c}{N} \sum_{k=1}^{N} k \cdot i_k
\end{aligned} \tag{2.40}$$

we obtain the final current derivative recursive estimation formula:

$$\frac{\hat{di}}{dt} = \frac{12}{T_c N(N^2-1)} \left(\sum_{k=1}^{N} k \cdot i_k - \frac{N+1}{2} \sum_{k=1}^{N} i_k \right) \tag{2.41}$$

The implementation of this formula requires a very low computational effort, because it only consists in two accumulations, computed by the FPGA, and one division, performed by the microcontroller (μC) at the end of the sampling period. The block diagram of the implemented

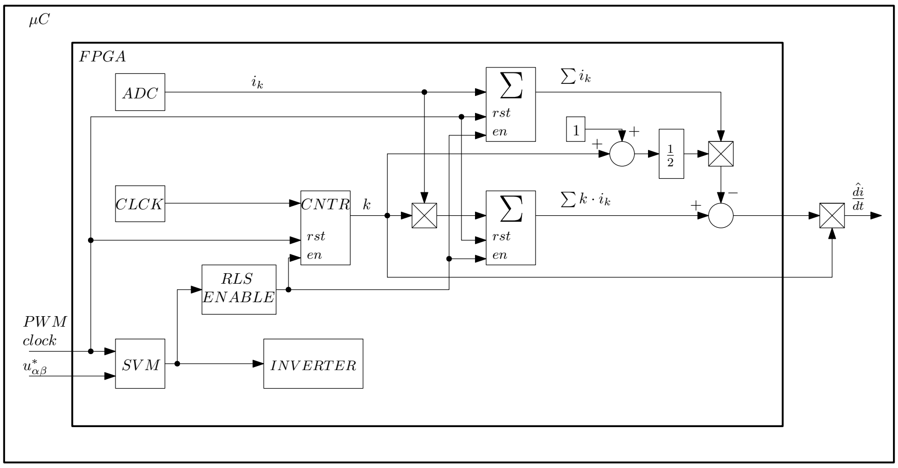

Figure 2.12: Block diagram of the current derivative estimation algorithm.

algorithm is reported in figure 2.12. In this figure the μC and the FPGA are reported: the first sends to the latter the reference voltage vector and the PWM clock signal. Then, the FPGA generates the IGBTs commands, inside the Space Vector Modulation block, that are sent to the inverter and to the *RLS ENABLE* block. This block identifies the longest voltage vector applied, and generates a signal which enables the *RLS* regression during its application time. The PWM clock signal resets the *CNTR* block and the accumulators at the beginning of every SVPWM period. The *ADC* block acquires the current samples i_k, while the *CLCK* block increases the *CNTR* output k at every sample instant. These two signals are used as inputs for the following accumulators, which, together with the other following blocks, compute the second term of formula 2.41. At the end of the PWM period, the generated signal and the value of k are sent to the μC, which performs the division of formula 2.41, thus generating the current derivative estimation.

2.2.3 *Position observers*

In this work two different open-loop position observers are developed and implemented. In both of them, the position estimation is based on measurements of the current ripple due to the standard SVPWM voltage vectors. The position observers are tested using an open-loop configuration, i.e. using the measured position for the current and speed control while comparing it to the estimated position, in order to avoid stability problems during the algorithm testing. The block diagram used for these tests is reported in figure 2.13.

The position is estimated with a $\pi\, rad\, el$ modulo, because of the $2\theta_{me}$ dependency, but using an initial position algorithm the rotor position is correctly retrieved. The stator resistance R is assumed to be known and updated by an online tracking algorithm, as that proposed in [15].

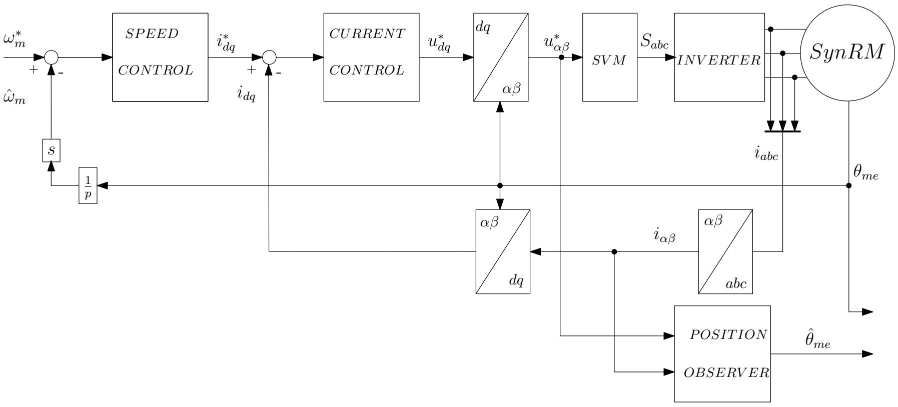

Figure 2.13: Block diagram of the openloop position estimation.

2.2.3.1 *Longest Vector analysis based Observer (LVO)*

The first type of observer uses the electrical measurements obtained during the longest vector of the SVPWM. In order to obtain the position estimation, SynR motor's equations 2.24 are solved, introducing some hypothesis to simplify it. First, we can assume that in standard AC drives the electrical speed is much lower than the PWM frequency:

$$2\pi f_{\text{PWM}} \gg \omega_{me} \tag{2.42}$$

which implies:

$$f_{\text{PWM}} \gg \frac{d\theta_{me}}{dt} \cdot \frac{1}{2\pi} \tag{2.43}$$

Therefore we can write:

$$\theta_{me,(k+1)T_{\text{PWM}}} - \theta_{me,kT_{\text{PWM}}} \simeq 0 \tag{2.44}$$

where $k = 1, ..., n$, T_{PWM} is the SVPWM period and $\theta_{me,kT_{\text{PWM}}}$ is the sampled position at the beginning of this period. For this reason, θ_{me} can be assumed to be constant during a single SVPWM period, and in this was even $cos(2\theta_{me})$ and $sin(2\theta_{me})$ result to be constant during T_{PWM}.

Moreover, as shown in paragraph 2.2.2.1, we can approximate the current derivatives as linear during the application time of a single voltage vector. Thanks to this approximation, $\frac{di_\alpha}{dt}$ and $\frac{di_\beta}{dt}$ can be considered constant during the application of a single voltage vector. Therefore, system 2.24 becomes a linear system, rewritten replacing $cos(2\theta_{me})$ and $sin(2\theta_{me})$ with c and s respectively, which are the only unknown variables:

$$\begin{cases} u_\alpha = R\, i_\alpha + \dfrac{di_\alpha}{dt}\,(L_\Sigma - L_\Delta\, c) - L_\Delta\, \dfrac{di_\beta}{dt}\, s - 2\, L_\Delta\, c\, i_\beta\, w_{me} + 2\, L_\Delta\, i_\alpha\, s\, w_{me} \\ u_\beta = R\, i_\beta + \dfrac{di_\beta}{dt}\,(L_\Sigma + L_\Delta\, c) - L_\Delta\, \dfrac{di_\alpha}{dt}\, s - 2\, L_\Delta\, c\, i_\alpha\, w_{me} - 2\, L_\Delta\, i_\beta\, s\, w_{me} \end{cases}$$

$$\tag{2.45}$$

Solving this system, with the mathematical steps reported in A.2, we obtain the expressions of $cos(2\theta_{me})$ and $sin(2\theta_{me})$, which are used to calculate θ_{me} with the $atan2$ operator:

$$\begin{aligned}\widehat{sin}(2\theta_{me}) =& \,2\,L_\Sigma\,\frac{di_\beta}{dt}\,\frac{di_\alpha}{dt} - \frac{di_\alpha}{dt}\,u_\beta - \frac{di_\beta}{dt}\,u_\alpha + R\,\frac{di_\beta}{dt}\,i_\alpha + R\,\frac{di_\alpha}{dt}\,i_\beta + \\ &+ 2\,i_\alpha\,u_\alpha\,\hat{w}_{me} - 2\,i_\beta\,u_\beta\,\hat{w}_{me} - 2\,R\,{i_\alpha}^2\,\hat{w}_{me} + 2\,R\,{i_\beta}^2\,\hat{w}_{me} + \\ &- 2\,L_\Sigma\,\frac{di_\alpha}{dt}\,i_\alpha\,\hat{w}_{me} + 2\,L_\Sigma\,\frac{di_\beta}{dt}\,i_\beta\,\hat{w}_{me}\end{aligned} \tag{2.46}$$

$$\begin{aligned}\widehat{cos}(2\theta_{me}) =& \,\frac{di_\beta}{dt}\,u_\beta - \frac{di_\alpha}{dt}\,u_\alpha - L_\Sigma\,\frac{di_\beta}{dt}^2 + L_\Sigma\,\frac{di_\alpha}{dt}^2 + R\,\frac{di_\alpha}{dt}\,i_\alpha + \\ &- R\,\frac{di_\beta}{dt}\,i_\beta - 2\,i_\alpha\,u_\beta\,\hat{w}_{me} - 2\,i_\beta\,u_\alpha\,\hat{w}_{me} + 2\,L_\Sigma\,\frac{di_\beta}{dt}\,i_\alpha\,\hat{w}_{me} + \\ &+ 2\,L_\Sigma\,\frac{di_\alpha}{dt}\,i_\beta\,\hat{w}_{me} + 4\,R\,i_\alpha\,i_\beta\,\hat{w}_{me}\end{aligned} \tag{2.47}$$

$$\hat{\theta}_{me} = \frac{1}{2}\mathrm{atan2}\left(\frac{\widehat{sin}(2\theta_{me})}{\widehat{cos}(2\theta_{me})}\right) \tag{2.48}$$

This position estimation can be done during each of the seven voltage vectors applied in a SVPWM period, because it just requires electrical measurements, which are available at every sampling instant. Anyway it is performed only at the end of the longest one, in order to have a larger time window to compute the current derivative estimation. A large time window is required because the phase currents are affected by high frequency oscillations, due to motor and drive's parasitic elements, increasing the required RLS regression's converging time. Indeed, the switching transients of inverter's IGBTs result in current waveforms being affected by high frequency oscillations which prevent accurate measurement of the current derivative. Then, by performing the position estimation during the longest application time of a SVPWM vector, it's ensured that the estimated values of the current derivatives are as close as possible to the real ones. Moreover, using this technique the minimum pulse violations are avoided, i.e. there's always a voltage vector long enough to perform the derivative estimation. However this observer has a high parameter dependency, because it requires L_Σ and L_Δ, the electrical resistance R and the electro-mechanical speed estimated at the previous step $\hat{w}_{me,k-1}$. The block diagram used to implement the LVO is reported in figure 2.14.

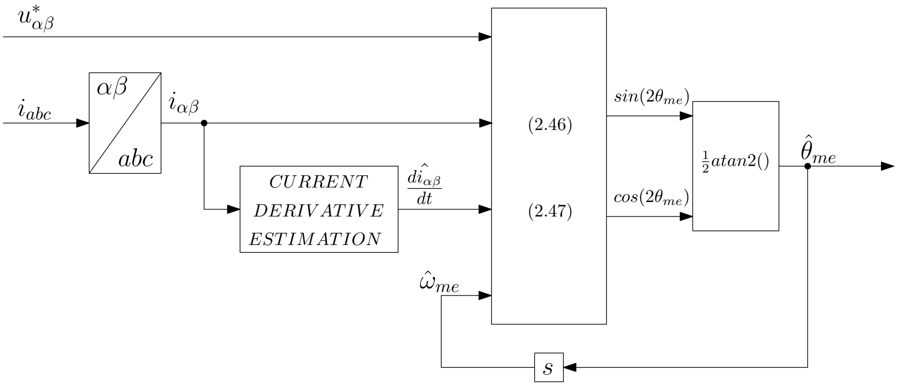

Figure 2.14: Block diagram of the Longest Vector analysis based Observer.

2.2.3.2 *Resistance and Speed Independent Observer (RSIO)*

The second observer implemented uses the electrical measurements obtained during two different vectors applied in a SVPWM period, which will hereafter be called $\boldsymbol{u}_{\alpha\beta,m}$ and $\boldsymbol{u}_{\alpha\beta,m1}$. Then,we can write equation 2.17 for both these two vectors, obtaining the two equations reported below:

$$\begin{aligned}\boldsymbol{u}_{\alpha\beta,m} &= R\boldsymbol{i}_{\alpha\beta,m} + \frac{d\boldsymbol{L}_{\alpha\beta}}{dt}\boldsymbol{i}_{\alpha\beta,m} + \boldsymbol{L}_{\alpha\beta}\frac{d\boldsymbol{i}_{\alpha\beta,m}}{dt} \\ \boldsymbol{u}_{\alpha\beta,m1} &= R\boldsymbol{i}_{\alpha\beta,m1} + \frac{d\boldsymbol{L}_{\alpha\beta}}{dt}\boldsymbol{i}_{\alpha\beta,m1} + \boldsymbol{L}_{\alpha\beta}\frac{d\boldsymbol{i}_{\alpha\beta,m1}}{dt}\end{aligned} \tag{2.49}$$

In a SVPWM period the resistive voltage drop $\boldsymbol{R}\boldsymbol{i}_{\alpha\beta}$ and the bemf $\frac{d\boldsymbol{L}_{\alpha\beta}}{dt}\boldsymbol{i}_{\alpha\beta}$ can be considered constant. Using these hypotheses, when subtracting the second equation of 2.49 to the first one, the terms $\boldsymbol{R}\boldsymbol{i}_{\alpha\beta}$ and $\frac{d\boldsymbol{L}_{\alpha\beta}}{dt}i_{\alpha\beta}$ are simplified, so we obtain the following equation:

$$\boldsymbol{u}_{\alpha\beta,m} - \boldsymbol{u}_{\alpha\beta,m1} = \boldsymbol{L}_{\alpha\beta}(\frac{d\boldsymbol{i}_{\alpha\beta,m}}{dt} - \frac{d\boldsymbol{i}_{\alpha\beta,m1}}{dt}) \tag{2.50}$$

which can be rewritten in a more compact form:

$$\boldsymbol{u}_{\alpha\beta,m-m1} = \boldsymbol{L}_{\alpha\beta}\frac{d\boldsymbol{i}_{\alpha\beta,m-m1}}{dt} \tag{2.51}$$

Doing some mathematical steps, reported in A.3, similar to those reported in the previous paragraph, we can obtain the following position estimation's formula:

$$\hat{\theta}_{\mathrm{me}} = \frac{1}{2}\mathrm{atan2}\left(\frac{num}{den}\right) \tag{2.52}$$

where:

$$\begin{aligned}num = &\frac{di_{\beta,m-m1}}{dt}\,u_{\alpha,m-m1} + \frac{di_{\alpha,m-m1}}{dt}\,u_{\beta,m-m1} + \\ &- 2\,L_{\Sigma}\,\frac{di_{\beta,m-m1}}{dt}\,\frac{di_{\alpha,m-m1}}{dt}\end{aligned} \tag{2.53}$$

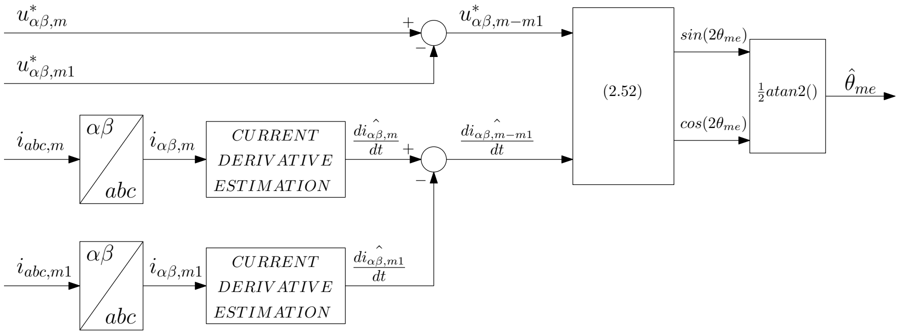

Figure 2.15: Block diagram of the Resistance and Speed Independent Observer.

$$den = L_\Sigma \frac{di_{\beta,m-m1}}{dt}^2 - u_{\beta,m-m1}\frac{di_{\beta,m-m1}}{dt} - L_\Sigma \frac{di_{\alpha,m-m1}}{dt}^2 + \\ + u_{\alpha,m-m1}\frac{di_{\alpha,m-m1}}{dt} \tag{2.54}$$

Analysing this formula, it can be seen that it is independent from the electrical resistance and from the estimated speed, reducing in this way the observer's parameter sensitivity. The block diagram used to implement the RSIO is reported in figure 2.15.

However this technique requires to estimate the current derivatives during two different vectors, which becomes a difficult or impossible task if there is only one vector applied for enough time. This critical situation happens when the vector's application time is too short, i.e. when there is not a sufficient amount of time to allow the oscillations to decay. In this situations, also called *minimum pulse width violations*, the RLS regression doesn't converge, and therefore the estimated current derivatives are incorrect. These minimum pulse width violations occur at low voltage references (only the null vector is long enough) and when crossing SVPWM boundaries (only one active vector is long enough). Figure 2.16 illustrates the areas in the SVPWM plane where the position cannot be estimated using the RSIO.

In order to reduce these areas, among the three voltage vectors applied in a SVPWM period, the two vectors analysed with this technique are the longest two, increasing the time window during which the current derivative estimation is computed. Anyway, even if the longest vectors are chosen, there are many situations in which the current derivative of these two vectors is not correctly estimated, due to their short application time, as will be further discussed in the next chapters. For this reason the RSIO observer can estimate the electro-mechanical position θ_{me} more difficultly than the LVO observer.

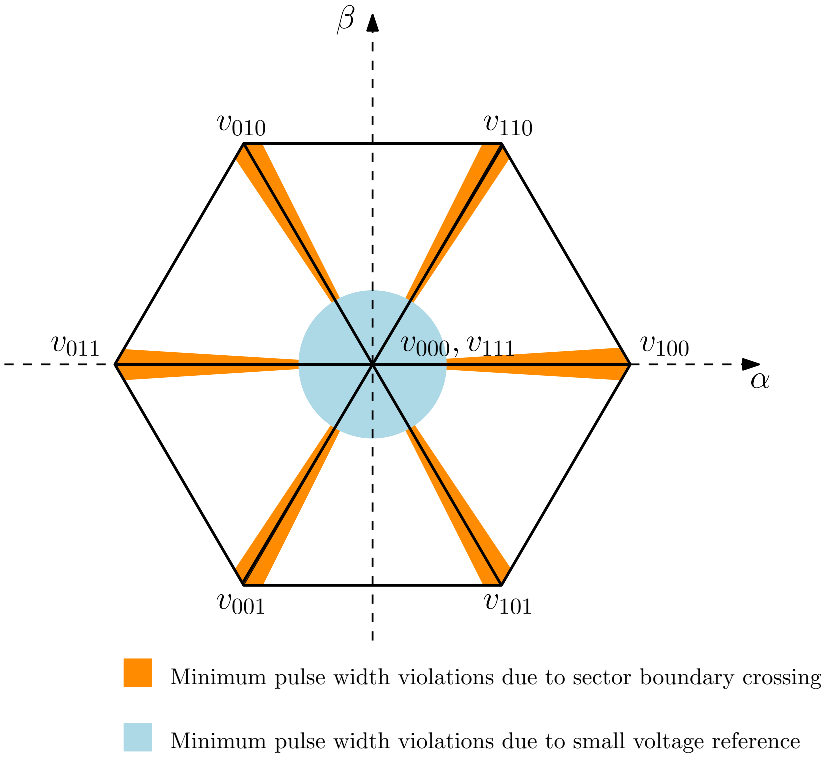

Figure 2.16: The locations on the SVPWM plane where minimum pulse width violations occur.

3

SIMULATIONS

3.1 RIPPLE SLOPE ESTIMATION

After the theoretical development of the RLS algorithm and of the position observers, the RLS regression was simulated in Matlab Simulink, in order to verify formula 2.41 and the accuracy of the slope estimation algorithm reported in 2.12.

3.1.1 *Model description*

To obtain significant results, the acquisition system was simulated using the parameters of the real one, which is a *MicroLabBox* (μLB) from *dSpace*. This system is composed of a μC and an FPGA, which can communicate with each other, and several ADCs and DACs. The parameters of the acquisition system are reported in table 3.1, while an image of the μLB is reported in figure 3.1.

The Simulink model, reported in figure 3.2, was simulated using a simulation time step equal to the FPGA clock period, i.e. 10 ns. In order to test the RLS regression algorithm, a saw-tooth signal with a constant slope voltage was used as input, and its slope was estimated and compared with the reference one (whose value is generated inside the *INPUT SLOPE* block).

Table 3.1: MicroLabBox parameters

Component	Frequency	Resolution	Input - Output
μC	100 kHz	64 bit	-
FPGA	100 MHz	64 bit	-
ADC	10 MHz	14 bit	$\pm 10V$
DAC	1 MHz	16 bit	$\pm 10V$

Figure 3.1: MicroLabBox. [16]

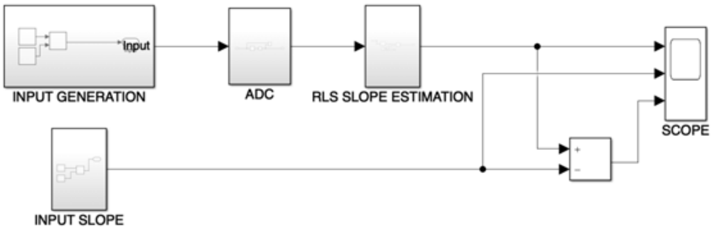

Figure 3.2: Simulink schematic used to simulate voltage slope estimation.

3.1.2 *Results*

The ADC input, generated by the block *INPUT GENERATION*, and its output, affected by quantization, are reported in figure 3.3 and 3.4. The quantization step is of $\frac{10V}{2^{13}} = 1.22 \cdot 10^{-3}\,V$.

The voltage slope is estimated by the block *RLS SLOPE ESTIMATION*, which was previously described in paragraph 2.2.2.3. The estimated slope is then compared with the reference input signal slope, as reported in figure 3.5: a small estimation error is observed, always under $0.2\,V/s$ out of a $245.5\,V/s$ reference slope, i.e. an error equal to 0.08%. Therefore, the slope estimation algorithm, under ideal conditions, can be considered accurate.

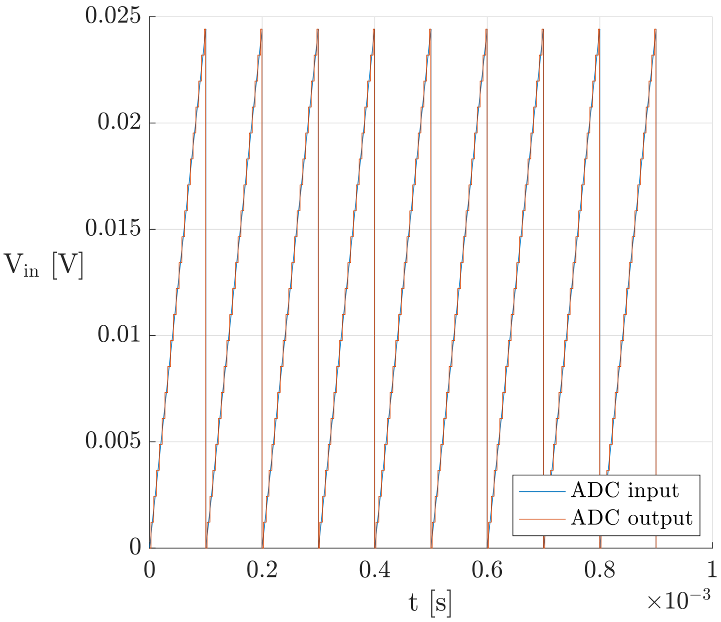

Figure 3.3: Input voltage.

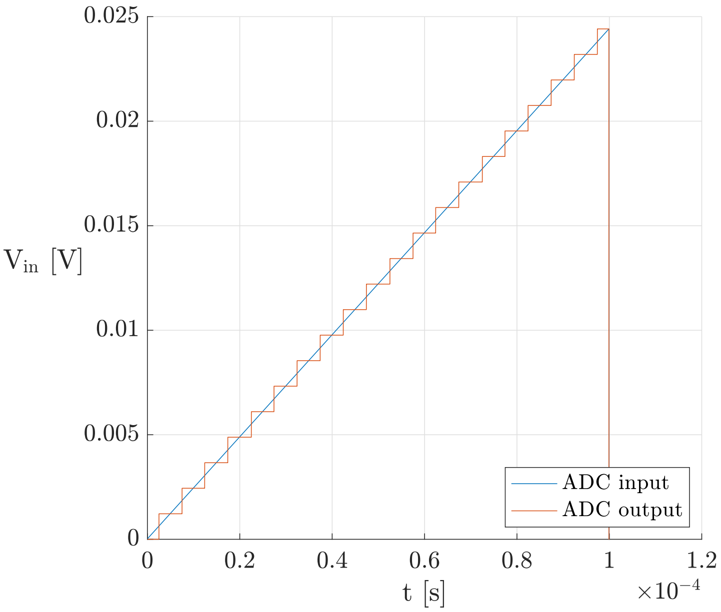

Figure 3.4: Zoom of input voltage.

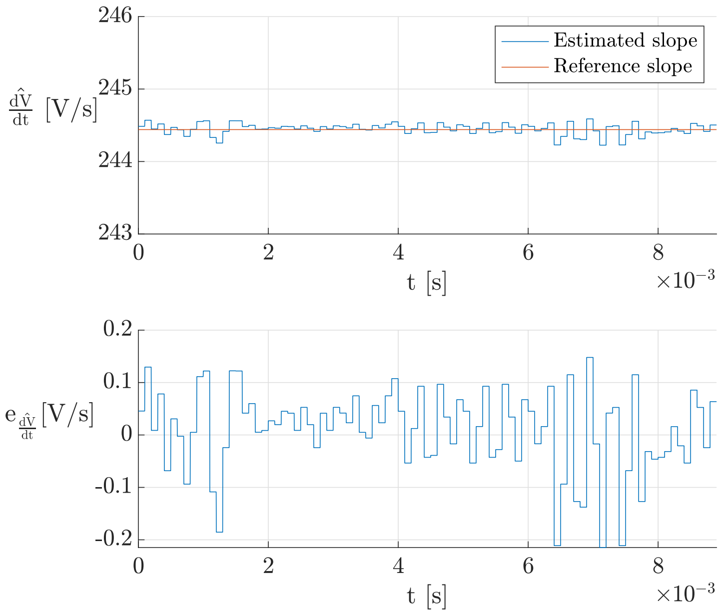

Figure 3.5: Input voltage slope.

3.2 POSITION OBSERVERS

In order to simulate the position observers, the schematic reported in figure 2.13 was modelled in Simulink. Both the Longest Vector Observer (LVO) and the Resistance and Speed Independent Observer (RSIO) were tested, to verify their stability and feasibility.

3.2.1 *Model description*

The Simulink schematic used to simulate the position observers is reported in figure 3.6. The SVPWM was implemented inside the block *INVERTER CONTROL*, and its frequency is equal to the real drive one, i.e. 10 kHz. Therefore one thousand samples are collected during every T_{PWM} period. The SynRM model implemented was the one reported in figure 2.7, with the parameters of the motor used for experimental tests, which are reported in table 3.2.

None of the parasitic elements was simulated, thus phase currents were non affected by high frequency oscillations. Therefore, the RLS regression was computed during all the application time of the chosen voltage vectors. The speed and current control were realised using PI controllers: the current controller bandwidth and the phase margin were set at 300 Hz and 70°, respectively, while the speed controller was tuned manually, obtaining a bandwidth and a phase margin of 3 Hz and about 60°, respectively.

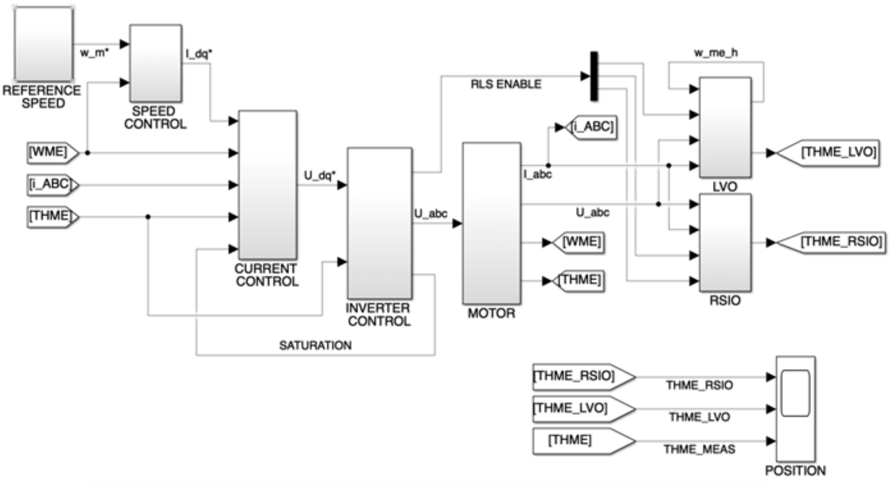

Figure 3.6: Simulink schematic used to simulate the position observers.

Table 3.2: SynRM parameters

Parameter	Symbol	Value
Nominal current	I_N	$4\,A$
Nominal speed	ω_N	$1500\,rpm$
Nominal torque	τ_N	$5.5\,Nm$
Pole pairs	p	2
Stator resistance	R	$4.76\,\Omega$
Direct synchronous inductance	L_d	$380\,mH$
Quadrature synchronous inductance	L_q	$85\,mH$
Inertia	J	$0.002\,kg\,m^2$
Viscous friction	B	$0.001\,Nms/rad$

3.2.2 *Results*

The observers performances were analysed using a trapezoidal speed reference, reported in figure 3.7, because it is a typical reference profile in standard AC drives applications. In this figure, also real and estimated position (both with LVO and RSIO), and their respective errors, are reported.

This simulation validates the observer accuracy: it can be noticed that the position error is always less than $\pm 0.2\,rad$, i.e. a good estimation is performed. The position estimation is correct also during transients, except for some spikes of the position estimated by the LVO, which happen after fast reference speed variations.

These variations generate abrupt current transients which, due to quantization and sampling, generate rapid step changes in the current values, used for the position estimation. Therefore, also the estimated position will be affected by step changes, which in turn generate spikes of the estimated speed, calculated in discrete time, used as a feedback for the next position estimations. Figure 3.8 shows an example of this situation.

Anyway, the position estimation oscillations settle quickly and, in a real drive, the spikes can be filtered.

These results also show that the LVO position estimation error decreases as speed increases. This is due to the gradual dominance of the speed-related terms in the equations 2.47 and 2.47. It is found that they are less dependent on the current derivatives than the others, which are more affected by noise.

For the RSIO, instead, the position estimation error slightly increases with speed: indeed the hypothesis that bemf and resistance losses are constant in a SVPWM (which was used to obtain equation 2.50 from 2.49), generates an estimation error which becomes more relevant as speed increases.

Moreover, it can be seen in figure 3.9 that, at constant speed, the position estimation accuracy is high: the error is less than $15 \cdot 10^{-3}\,rad$ and it is mainly due to the the position estimation updating only at the end of a SVPWM period.

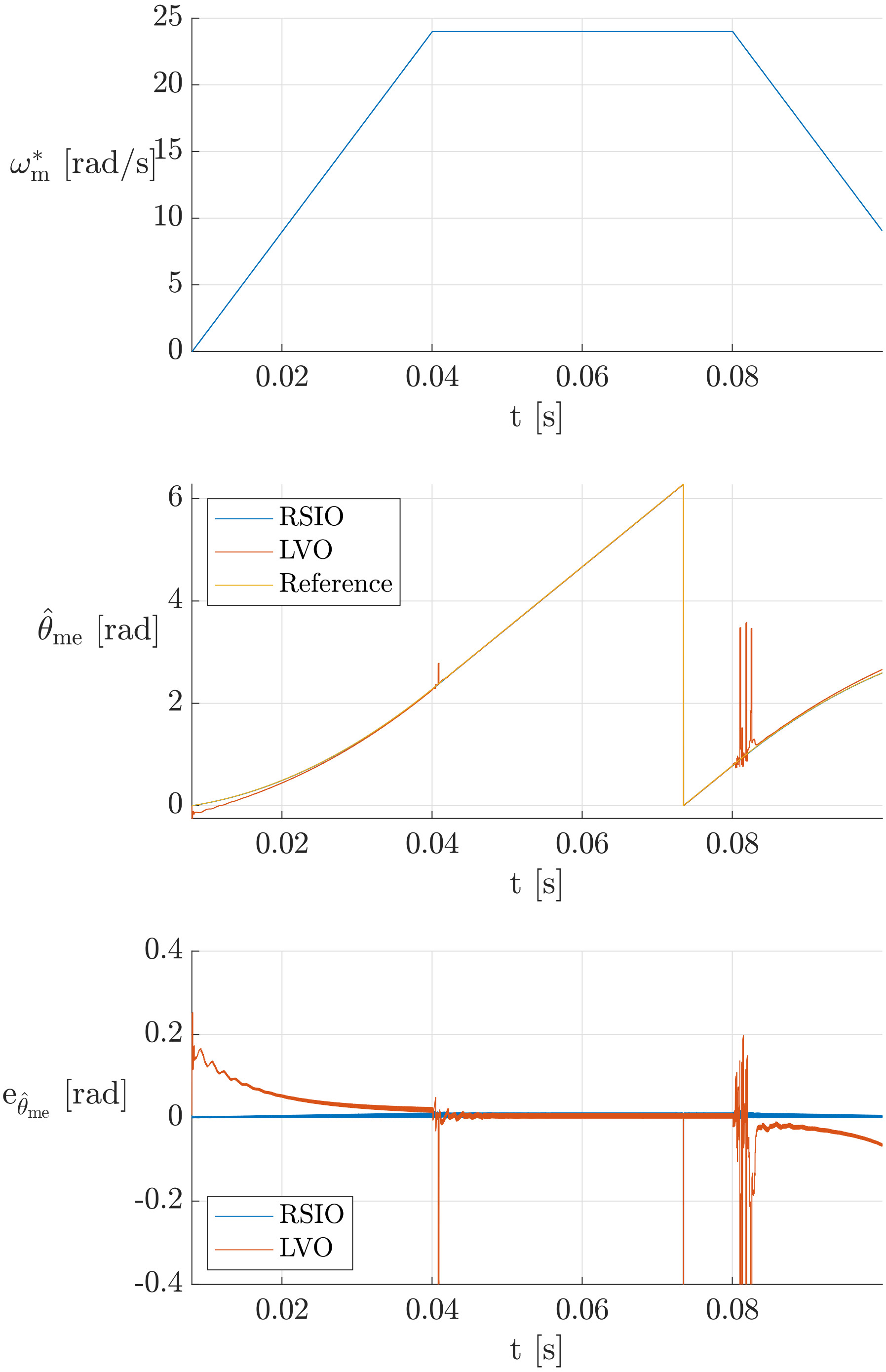

Figure 3.7: Reference rotor speed, real and estimated position (both with LVO and RSIO), and position estimation errors.

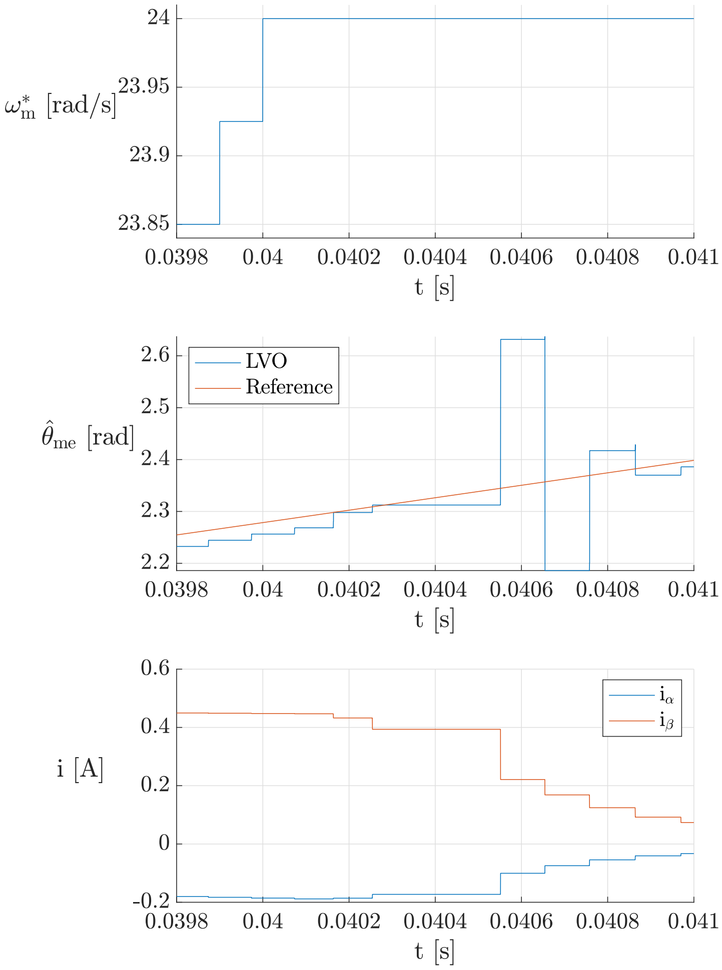

Figure 3.8: Reference rotor speed, real and estimated position, i_{ff} and i_{fi}.

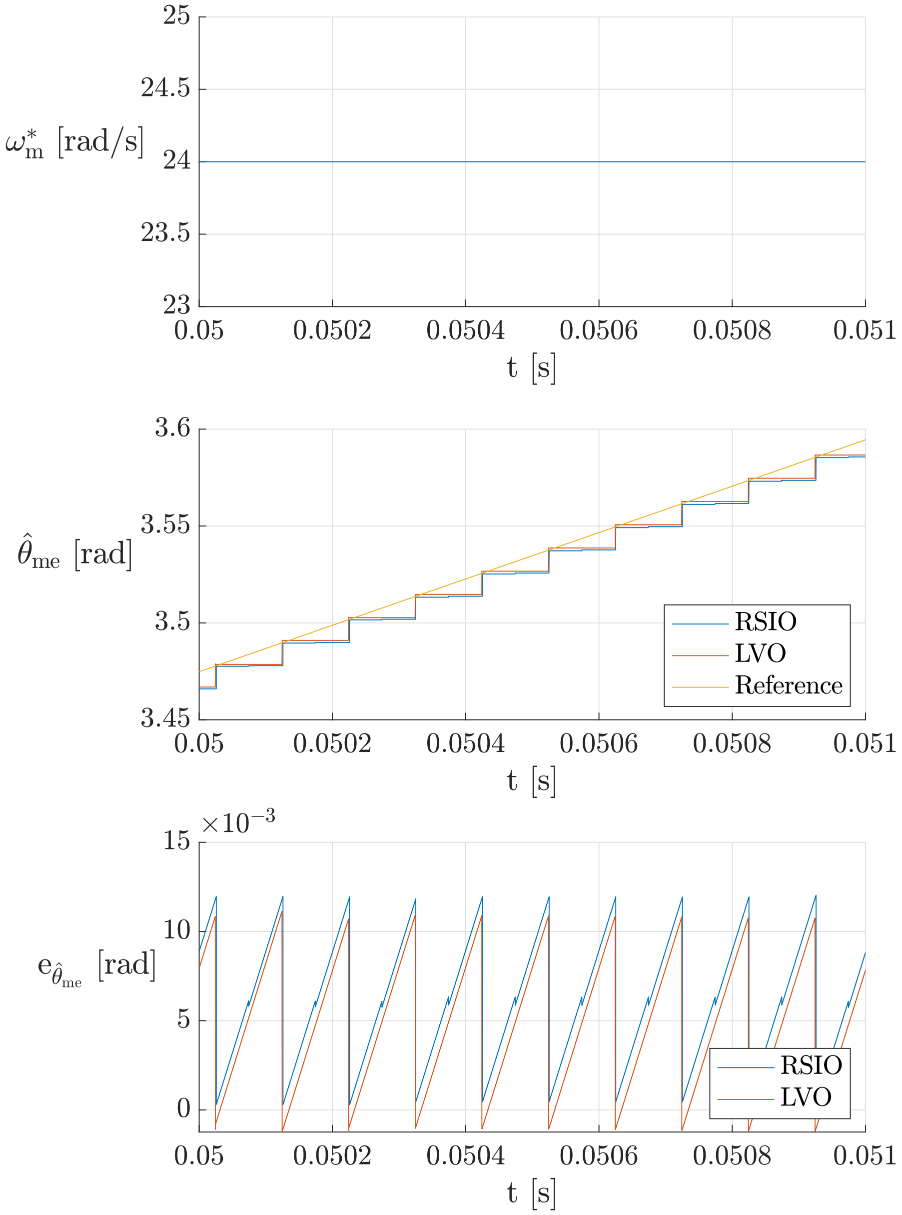

Figure 3.9: Zoom of reference rotor speed, real and estimated position (both with LVO and RSIO), and position estimation errors, at constant rotor speed of $30\, rad/s$.

4

EXPERIMENTAL TESTS

4.1 EXPERIMENTAL SETUP

The experimental tests were carried out using the setup reported in figure 4.1: the references and control parameters are sent, using an ethernet connection, from the PC to the μLB, described in 3.1.1, while the measured data are sent from the latter to the former and the estimated position is sent to the data-logger. The μLB delivers the switching signals to a *dSpace* inverter (INV), which is used to feed the SynRM, described in 3.2.1. The rotor position is measured using an encoder with a resolution of 1024 pulses per revolution, and it is used for closed-loop control and to compare measured and estimated position. The currents are measured using LEM sensors with a bandwidth of 150 kHz (-1dB). Images of inverter and data-logger are reported in figures 4.2 and 4.3, respectively. The data-logger was a *YOKOGAWA - DL850EV*, with two channels with a sample rate of 10 MHz and four channels at 1 MHz. The μLB was programmed using a tool of *VIVADO-XILINX* for *Simulink-Matlab*.

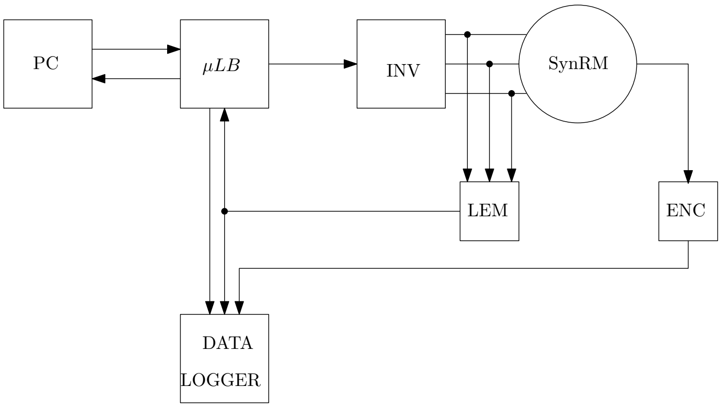

Figure 4.1: Block diagram of the experimental setup.

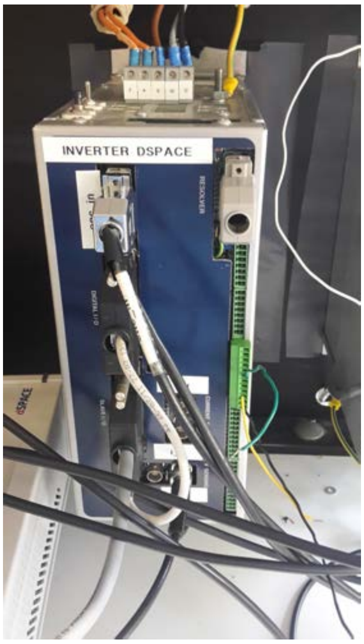

Figure 4.2: Inverter used for the experimental tests.

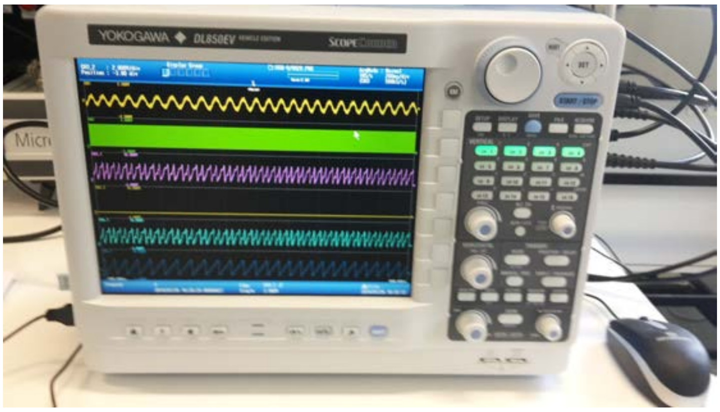

Figure 4.3: Data logger used for the experimental tests.

4.2 RIPPLE SLOPE ESTIMATION

The first experimental test carried out was the RLS regression validation, in order to verify the right implementation of schematic 2.12, the accuracy of the implemented slope estimation algorithm and the noise introduced by quantization. The sawtooth input voltage, reported in figure 4.4 and in figure 4.5, was generated using the DAC of μLB.

The reference and estimated voltage slopes are reported in figure 4.6: a good estimation is performed, which is affected by a random noise, mainly due to measurements disturbances and quantization errors. However, the estimation error is always less than $200\,V/s$ out of $3000\,V/s$, i.e. it is less than 7%. This error is higher than the one obtained in simulations due to the real-system non-idealities, measurements noise, and lower computational precision.

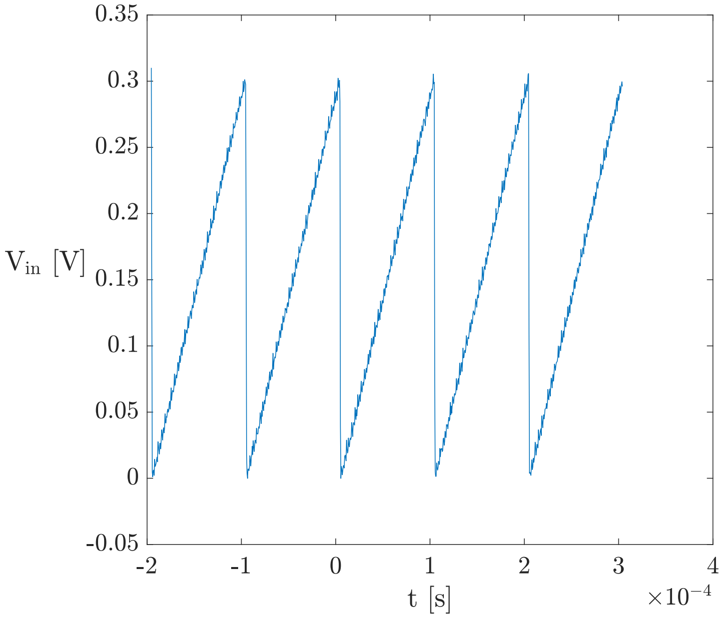

Figure 4.4: Input voltage.

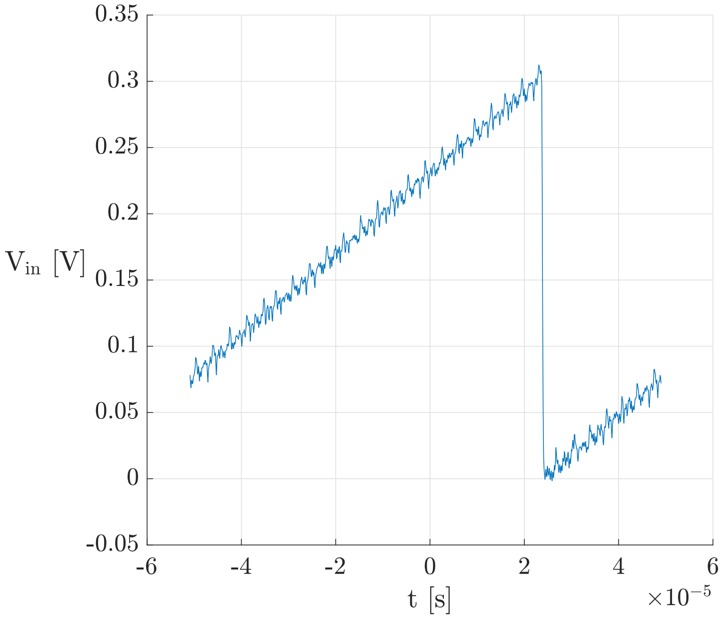

Figure 4.5: Input voltage zoom.

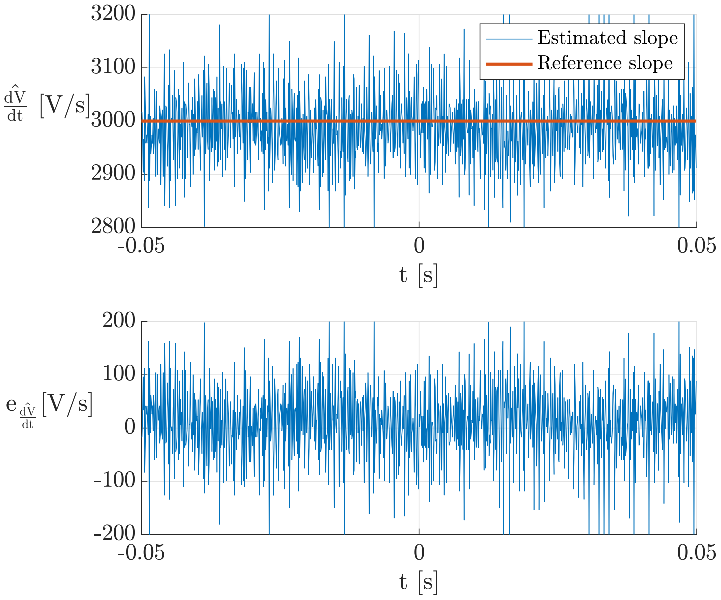

Figure 4.6: Input voltage slopes.

4.3 POSITION OBSERVERS

Before implementing the position observers in the μLB, the LVO feasibility was tested using the oversampled current data, measured during a steady-state motor operation, as an input for the Simulink model described in Chapter 3. This procedure is denominated as *post-processing estimation*. Then both the position observers have been implemented and tested on the real drive.

4.4 POST-PROCESSING ESTIMATION

4.4.1 *Input data*

At the beginning, in order to implement in an accurate way the post-processing estimation, the phase currents i_a and i_b were sampled at 10 MHz, while the upper IGBTs command signals and the measured position were sampled at 1 MHZ. The collected data are reported in figures 4.7 and 4.8.

From these figures it can be noticed that phase currents are affected by high frequency oscillations, previously described in paragraph 2.2.2.2, and the measured position is affected by encoders quantization and measurements disturbances.
The current derivative estimation enable signal was then generated using the IGBTs signals, as reported in figure 4.10: this logic signal is high during the application time of a voltage vector, excluding the dead times application instants, which were 4 μs in our experimental setup. In figure 4.9 are reported the dead times introduced by the inverter, necessary to avoid short-circuiting of the legs. RLS beginning

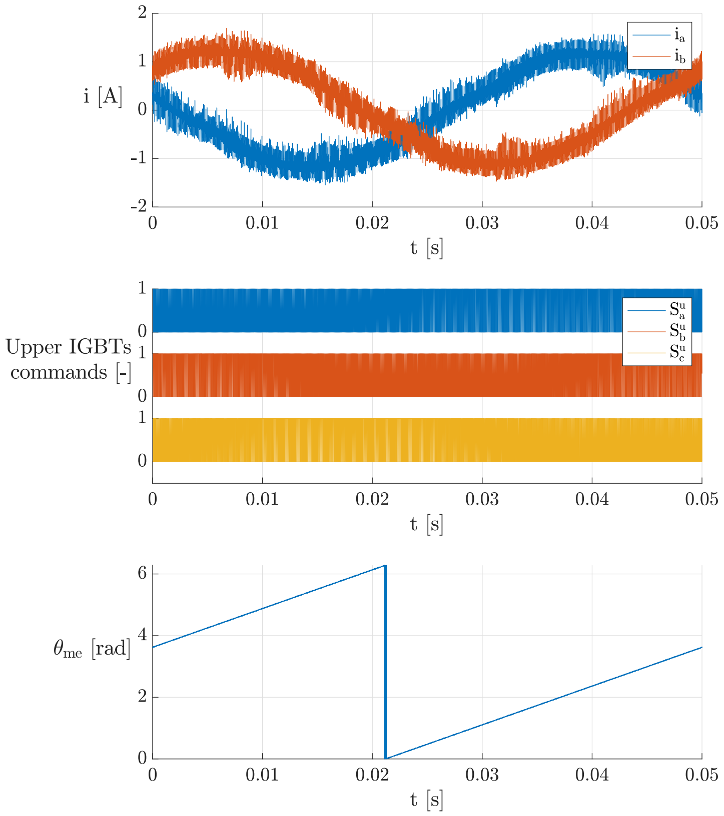

Figure 4.7: Measured data used as input for post-processing.

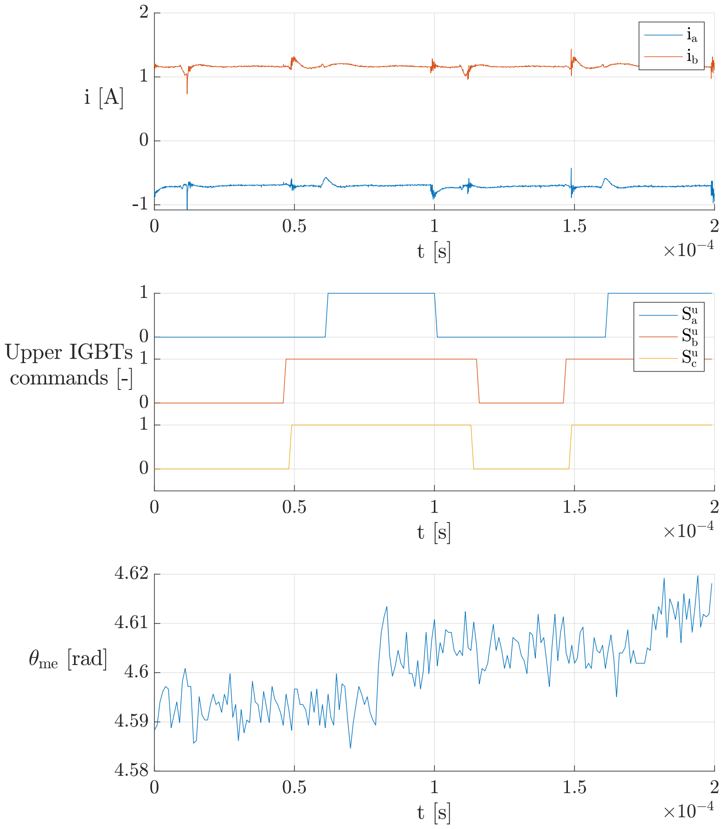

Figure 4.8: Measured data zoom.

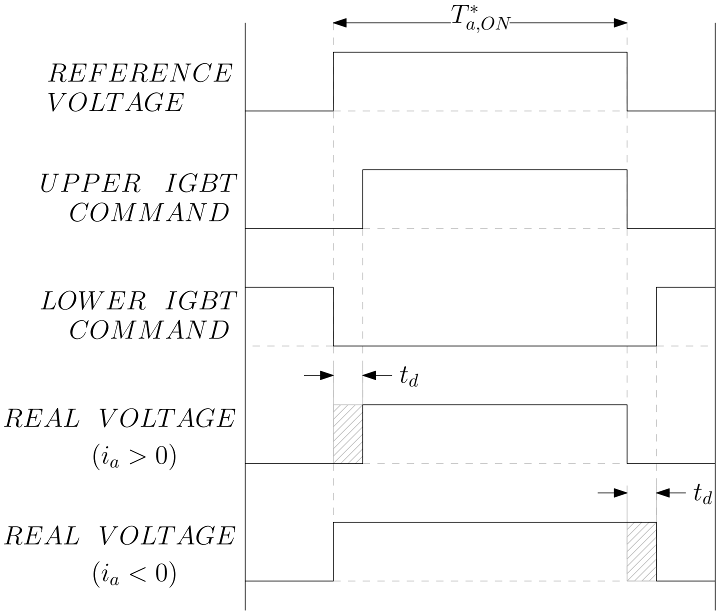

Figure 4.9: Introduction of dead times in switching the voltage inverter.

is delayed by introducing an estimation dead time, called $\mathrm{t_{wait}}$, after the application of the chosen voltage vector, to let the high-frequency oscillations decay, thus improving the position estimation accuracy. As previously described in paragraph 2.2.2.2, for the LVO the chosen vector is the longest one, while for the RSIO the two longest voltage vectors are chosen.

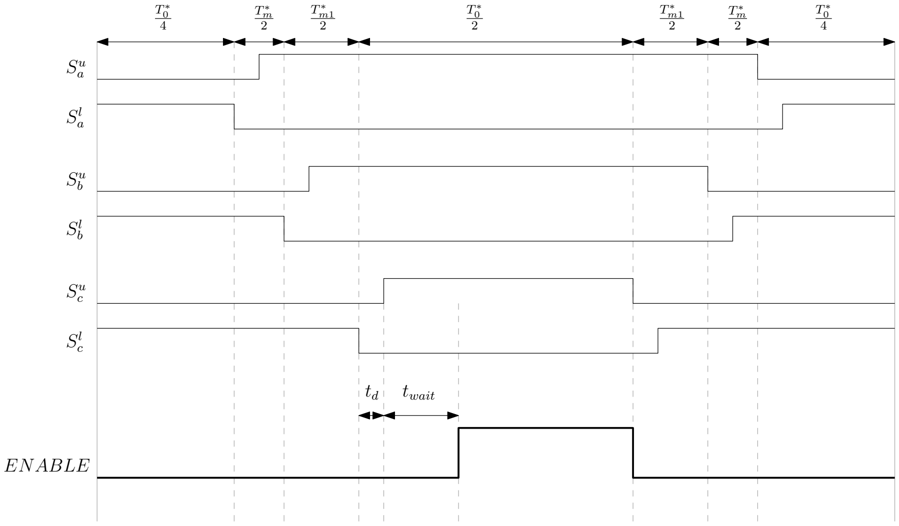

Figure 4.10: RLS regression enable signal.

4.4.2 *Three or two currents measurements*

In this work, all of the three phase currents were measured, to reduce the estimation noise. The three currents can be considered as ramp-

like signals with an added disturbance. This is due to the presence of parasitic elements in the converter, cables and motor windings that influence the current behaviour just after the IGBTs switching. Due to the current dispersion in the parasitic elements, the sum of the three currents is not zero.
If only two currents are measured and the third one is obtained as the opposite of the sum of the first two, its disturbance is amplified. This phenomenon is reported in figure 4.11, in which can be noticed that the derivative estimation accuracy is reduced and then the position observer precision is decreased.
The error reduction is more evident when the longest vector is the null one, because its current ripple is lower, resulting then more affected by parasitic elements disturbances and quantization.
Figure 4.12 shows that the high frequency oscillations on measured i_c

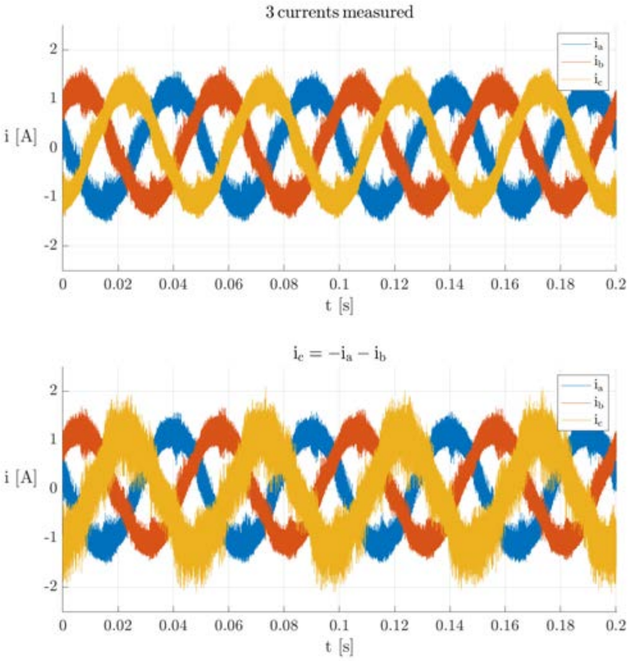
3 currents measured

$i_c = -i_a - i_b$

Figure 4.11: Phase currents obtained measuring two or three of them.

are completely different form the one of $i_c = -i_a - i_b$: this is mainly due to the current dispersions through parasitic circuits. The relationship between the oscillations on the different phase currents will be explained in details in Chapter 5.

The experimental results obtained measuring either three or two currents are reported in figure 4.13. From these graphs, it can be observed that, measuring all the three phase currents, the position estimation error is reduced.
This figure also shows that, when measuring only two currents, posi-

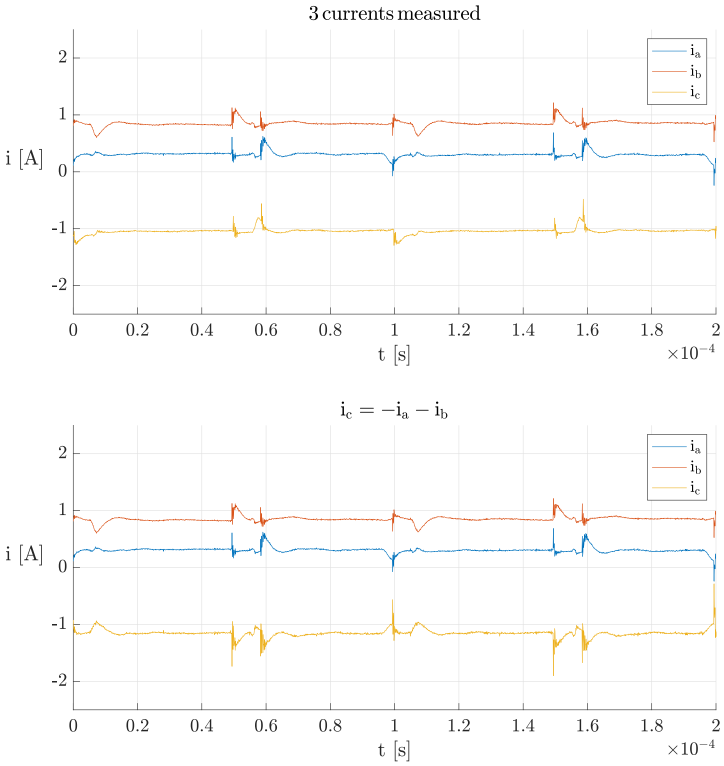

Figure 4.12: Zoom of phase currents obtained measuring two or three of them.

tion estimation spikes occur at around 4 ms, due to a great current derivative regression error, as reported and described in figure 4.16. In this situation, the derivative estimation error affects both $\frac{di_b}{dt}$ and $\frac{di_c}{dt}$, because, if only two currents are measured, i_c id affected by the same disturbances of i_b, increasing then the position estimation error.

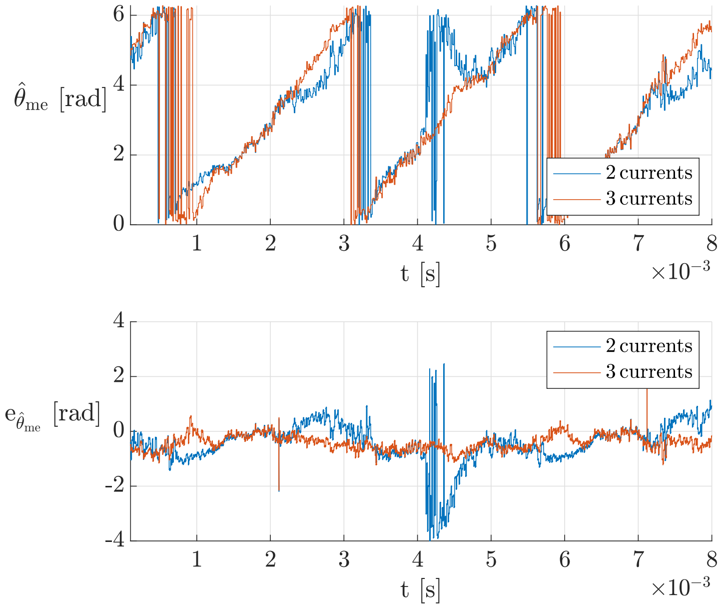

Figure 4.13: Estimated and measured rotor position, rotor position estimation error in steady state, measuring 2 or 3 phase currents.

4.4.3 *RLS regression enable signal tuning*

Different tests were carried out varying the value of the RLS delay (t_{wait}), in order to find its value which reduces as much as possible the estimation noise due to high-frequency oscillations, without reducing too much the regression time window.

In fact, oscillations modify the measured current ripple, thus affecting the RLS input signal, but even a short regression time window can cause an incorrect estimation convergence. Many values of t_{wait} were tried, but in figures 4.14 and 4.15 only the values of 2, 4 and $6\,\mu s$ are reported. It can be noticed that the value of t_{wait} that minimizes the position estimation error, during the post-processing analysis, is around $4\,\mu s$.

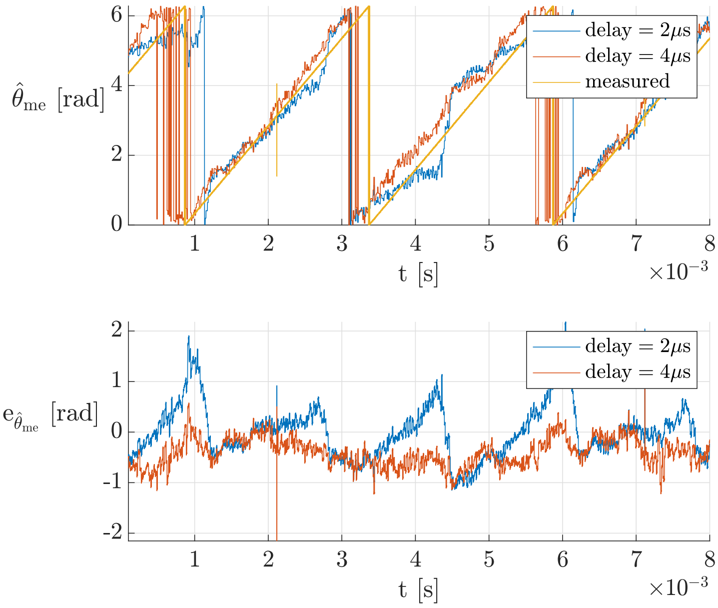

Figure 4.14: RLS enable delay effect: t_{wait} of $2\,\mu s$ and $4\,\mu s$.

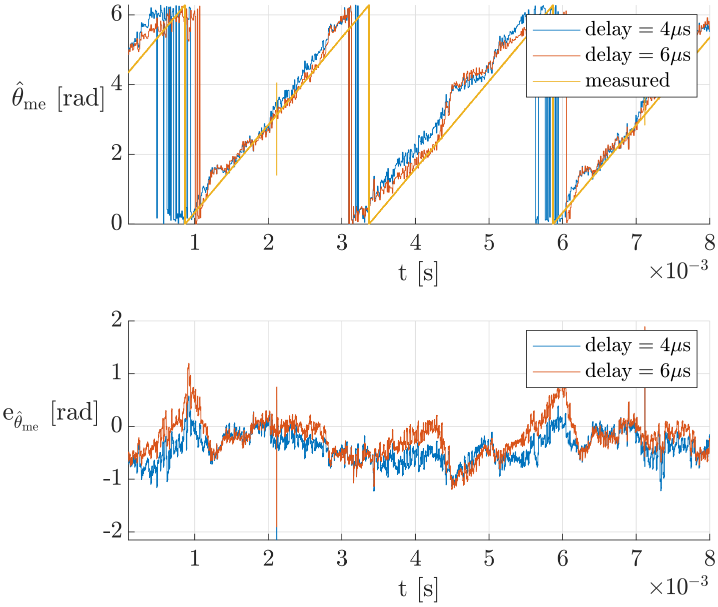

Figure 4.15: RLS enable delay effect: t_{wait} of $4\,\mu s$ and $6\,\mu s$.

4.4.4 *Sampled derivatives*

During the post-processing analysis it was observed that the main position estimation errors are due to current derivatives estimation errors. Figure 4.16 shows this position estimation distortion, which happens immediately after 0.04 s.

These distortions happen because the current RLS regression does not converge, due to the high frequency oscillations affecting the phase currents and a too short regression time. In particular, the wrong convergence of $\frac{di_b}{dt}$ estimation can be observed in figure 4.17.

This phenomenon happens when phase current $\mathrm{i_b}$ crosses the 0 A value with a negative trend, because in this region the current ripple is more affected by high frequency oscillation. It is found, indeed, that in this area, the oscillations due to the switching of leg *b* have a lower damping, amplifying then the current derivative regression error. The lower damping is probably due to the low value of $\mathrm{i_b}$, which slowly discharges the IGBT parasitic capacitances, which seem to be higher for phase *b*, and because the low frequency oscillation spike has a slope opposite to the current ripple. These oscillations will be described in detail in paragraph 5.1.1.

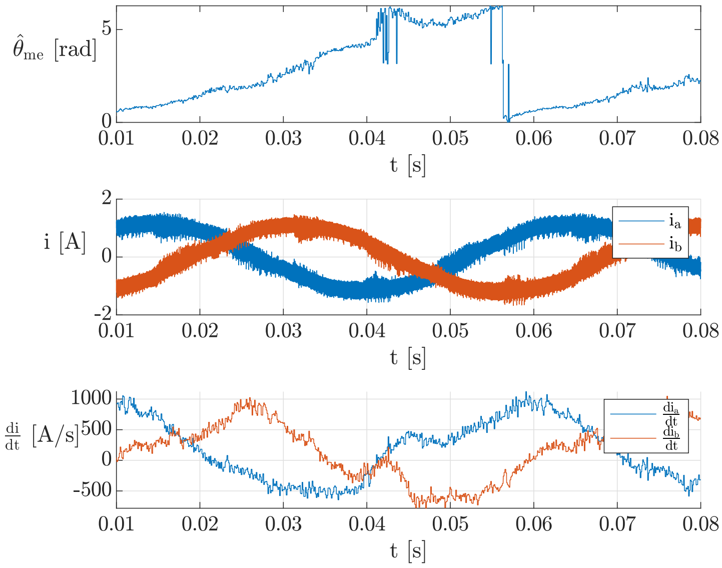

Figure 4.16: Estimated position obtained measuring only two currents, phase currents $\mathrm{i_a}$ and $\mathrm{i_b}$ and their estimated derivatives.

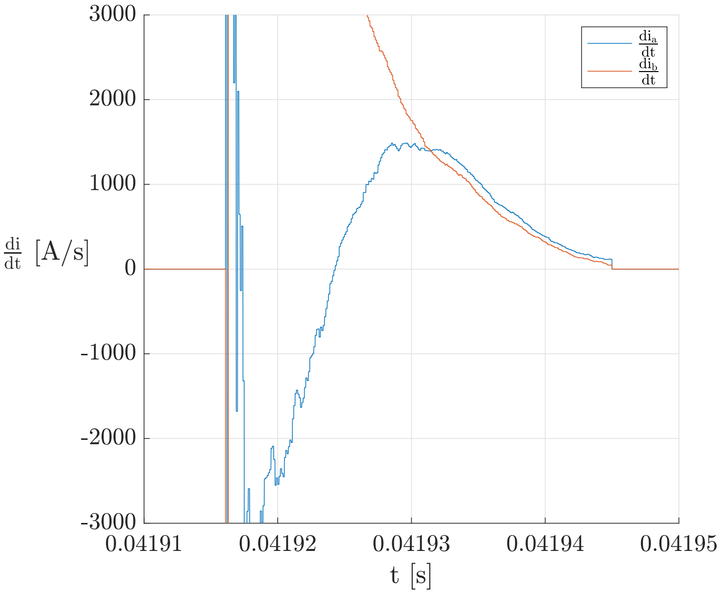

Figure 4.17: i_a and i_b derivatives estimation.

4.5 ONLINE RESULTS

The performances of both position observers (Longest Vector analysis based Observer and Resistance and Speed Independent Observer) have been analysed with experimental tests at different speeds, during either speed or torque reference step.
Before starting the observers testing, the RLS regression enable delay t_{wait} was tuned for the experimental setup: different values were tested, as reported in figures 4.18 and 4.19, finding an optimal value of $12\,\mu s$. The optimal value of t_{wait} found during online experiments is higher than the one obtained during the *post-processing estimation* due to the lower computational precision of the FPGA in comparison with the one of Matlab Simulink: in the former one, indeed, only fixed-point operations are allowed with a 64 bits precision.

Moreover, two tests were carried out in order to verify the improvement of position estimation precision due to the measurement of all three phase currents. The results of these tests are reported in figure 4.20: it can be noticed a position estimation error reduction, i.e. an improvement of observer's accuracy, as previously noticed during the *post-processing estimation*.

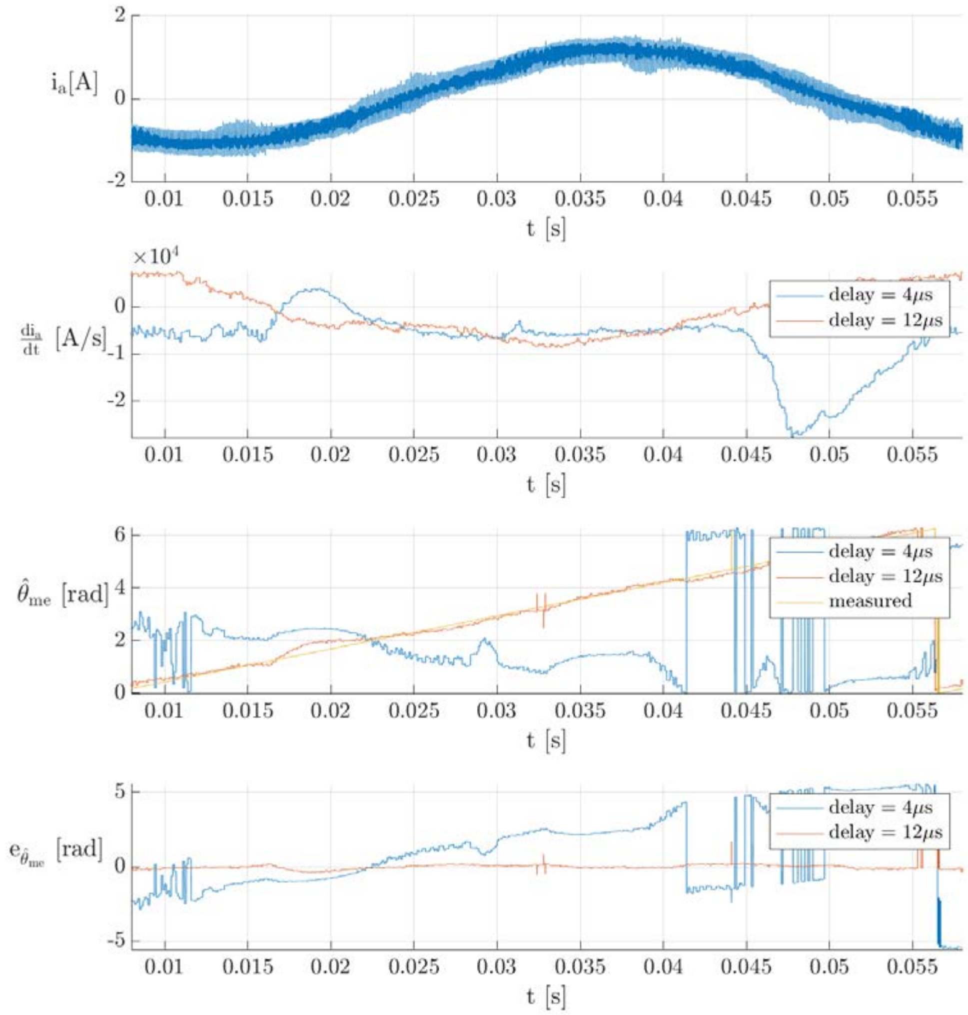

Figure 4.18: RLS enable delay effect: t_{wait} of $4\,\mu s$ and $12\,\mu s$.

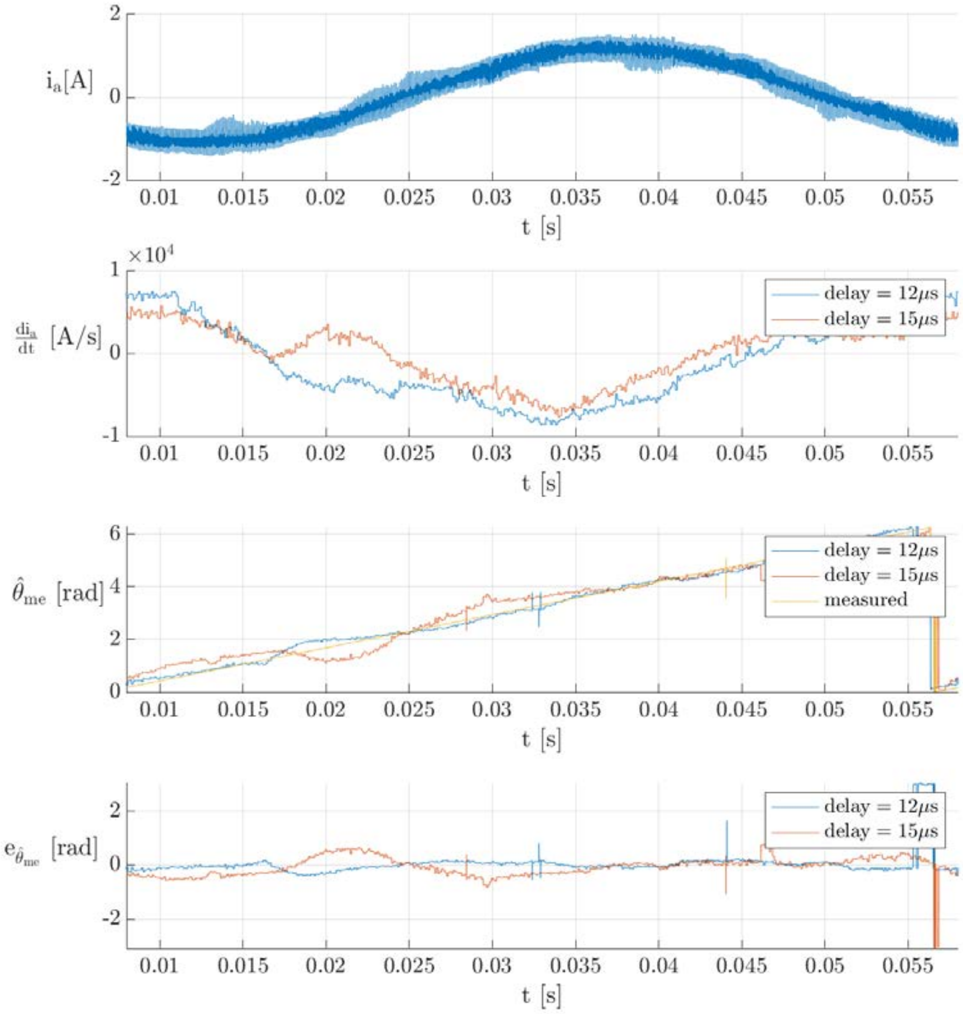

Figure 4.19: RLS enable delay effect: t_{wait} of $12\,\mu s$ and $15\,\mu s$.

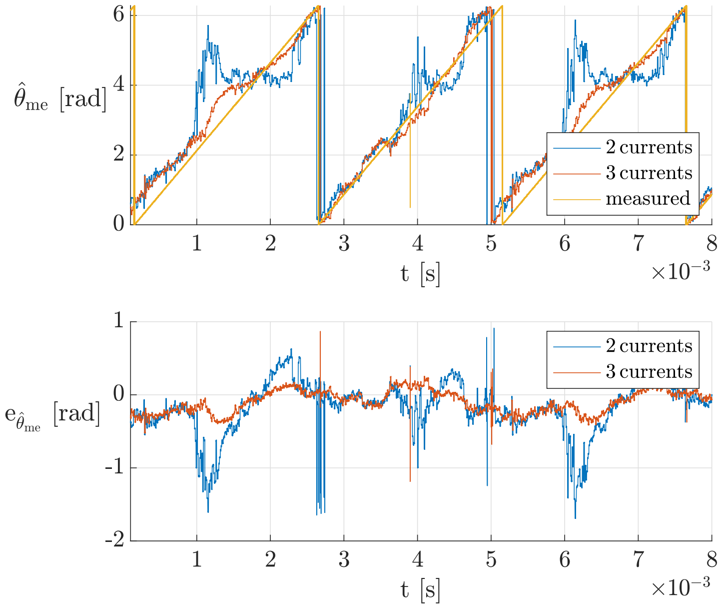

Figure 4.20: Estimated and measured rotor position, rotor position estimation error in steady state, measuring 2 or 3 phase currents.

4.5.1 *Longest Vector analysis based Observer and Resistance and Speed Independent Observer comparison*

The LVO and RSIO performances were then compared: the first test was performed at steady-state condition, with a 600 rpm reference rotor speed and a DC bus voltage of 540 V: the results are reported in figure 4.21.

It can be noticed that the LVO performs a good estimation, while the RSIO is not able to estimate the rotor position. The RSIO requires indeed to measure the current derivatives during two out of three SVPWM voltage vectors, but in this operating condition only the null vector is long enough to perform a correct current derivative estimation. The null vector is applied indeed for most of the PWM period, because, during the no-load operation, the reference voltage vector $\boldsymbol{u}^*_{\alpha\beta}$ generated by the current controller has a very low module.

Then, in order to increase the application time of the active voltage vectors, the DC bus voltage was decreased to 125 V: in this way the RLS regression time window increases, because, as the active vectors are increased, all the voltage vectors are applied for a long time, so the average duration of the two longest vectors is increased too. This concept is explained graphically in figure 4.22, considering two different measurements obtained with a DC bus voltage of 300 V and 500 V: in the bottom figure (obtained with 500 V) the null vector is applied for a longer time while the active vectors are applied for a shorter time. The same effect could be obtained even increasing the reference rotor speed, but the position estimation distortion is less evident.

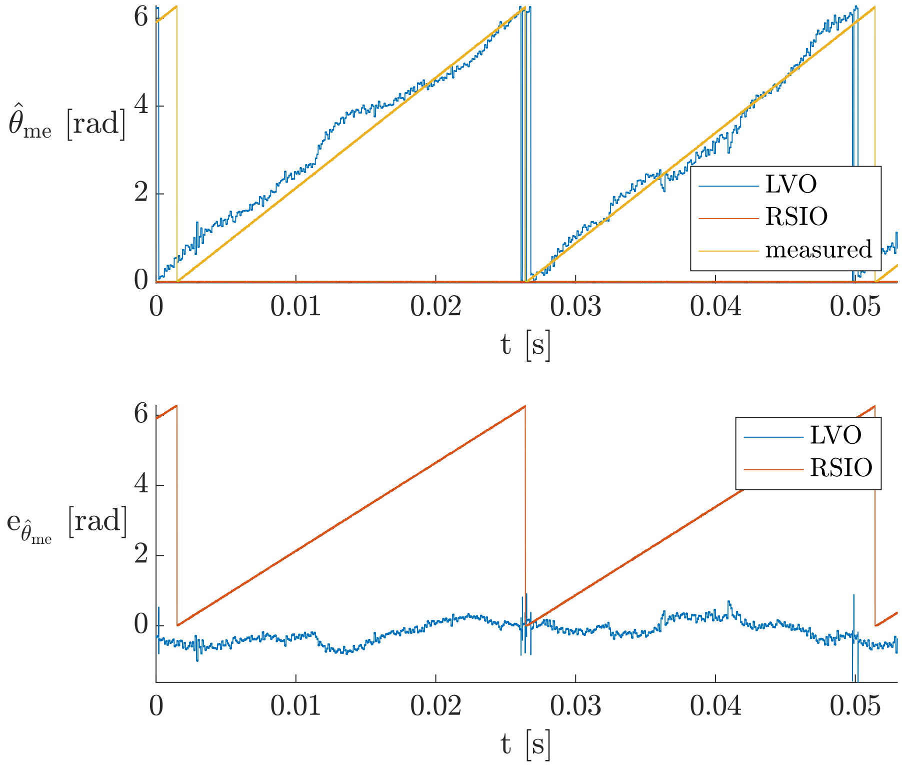

Figure 4.21: Estimated and measured rotor position, rotor position estimation error in steady state, obtained using LVO or RSIO, in inverter voltage no-saturation condition.

Thanks to this variation of the application times of voltage vectors, the RSIO performs a good estimation, but the LVO accuracy decreases. The LVO accuracy reduction happens because all the vectors are increased, thus the application time of the longest one is reduced.

Then, a possible future implementation of the sensorless control for SynRM, based on oversampling of current ripple due to standard PWM excitation, could consider a weighted average of LVO and RSIO estimations, depending on the drive's working conditions.
In the next paragraphs, due to the low precision of the RSIO in most of working conditions, only the LVO performances will be considered.

4.5.2 *Results at constant speed*

The estimated and measured positions, obtained at steady-state condition, along with the speed and estimation error, are reported in figure 4.24. The rotor speed during this test was around $400\,rpm$ at no-load and a DC bus voltage of 540 V. It can be noticed that the position estimation error is always less than $\pm 0.5\,rad$, i.e. a good estimation is performed.

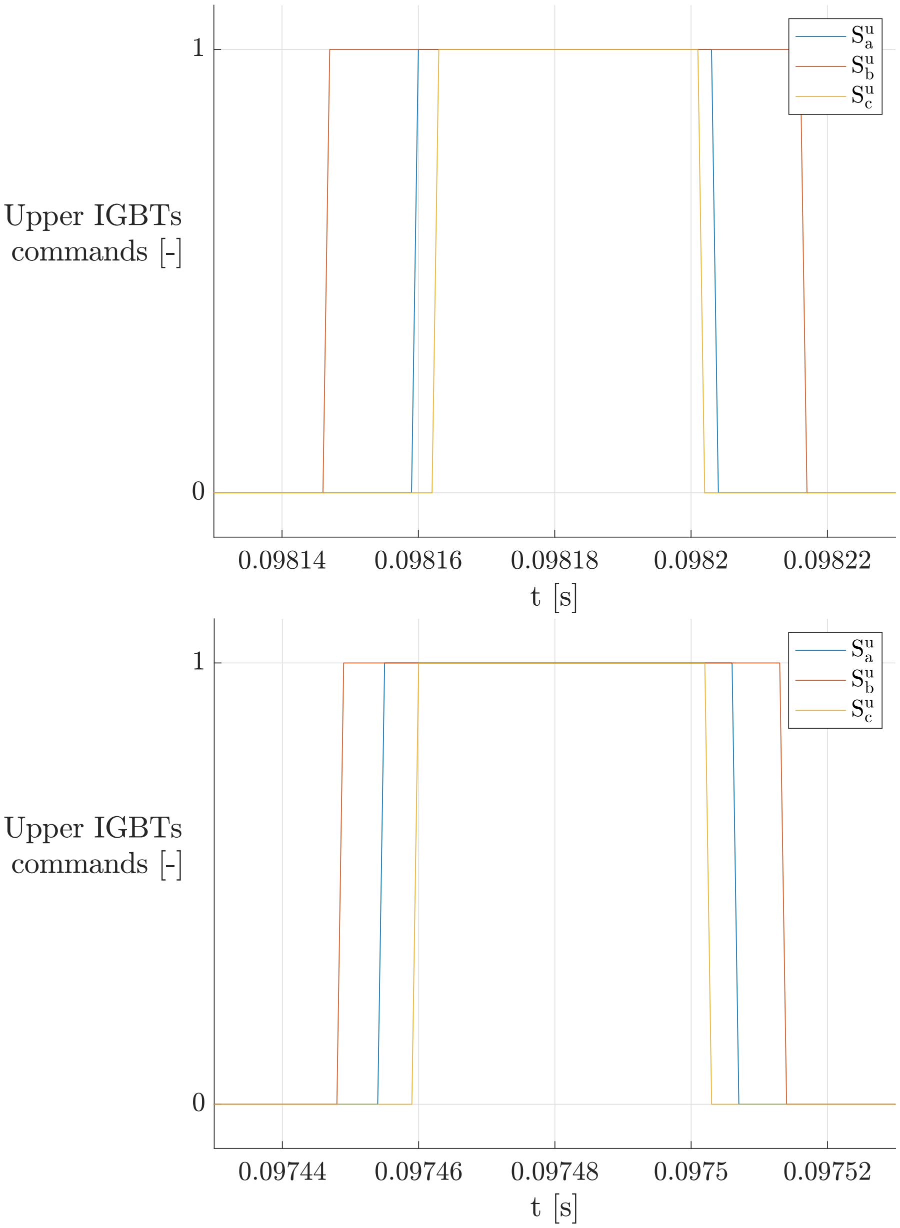

Figure 4.22: Upper IGBTs commands at a constant speed and with a DC bus voltage of 300 V (top) and 500 V (bottom).

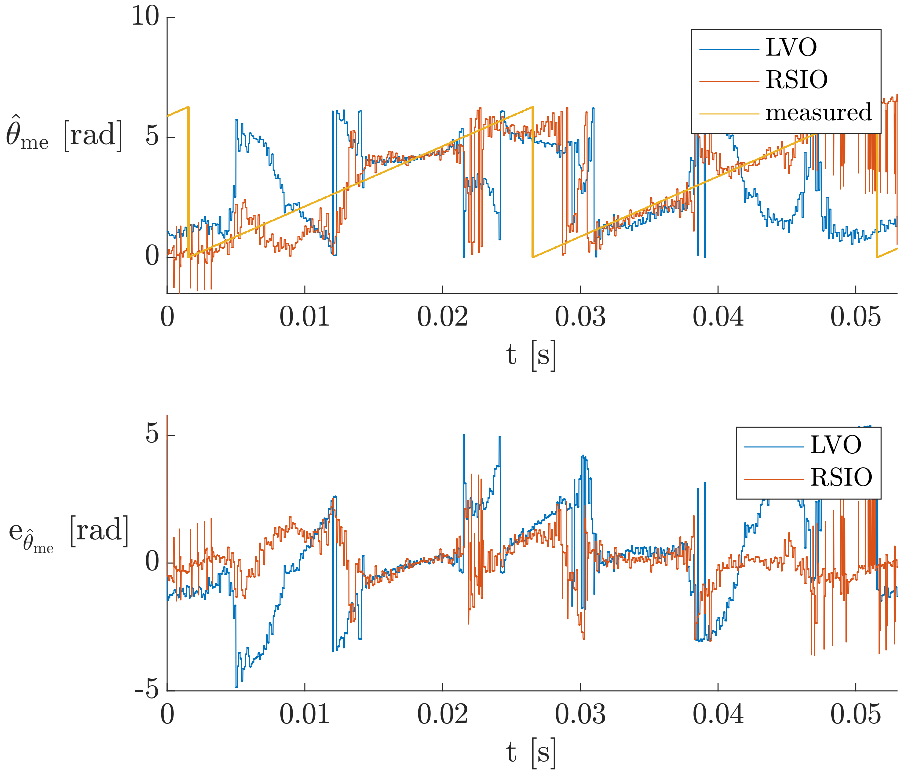

Figure 4.23: Estimated and measured rotor position, rotor position estimation error in steady state, obtained using LVO or RSIO, in inverter voltage saturation condition (i.e. $T_0 \simeq 0$).

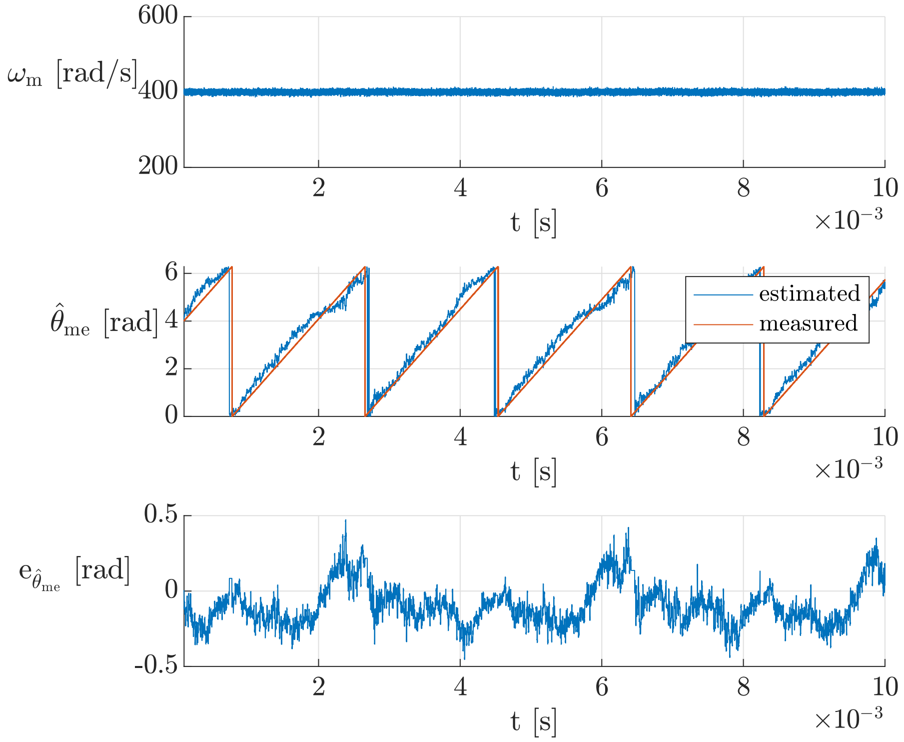

Figure 4.24: Measured rotor speed, estimated and measured rotor position, rotor position estimation error at steady state.

4.5.3 *Step variations of speed reference*

The experimental results obtained during step variations of the rotor speed reference from 375 to 750 *rpm* and from 750 to 375 *rpm* are reported in figures 4.25 and 4.26, respectively. These experimental tests validate the observer accuracy also during transients. They also show that the position estim ation error decreases as speed increases, as previously noticed in the simulations reported in paragraph 3.2.2.

The position estimation error during experimental tests is much higher than the simulations one, due to the current high-frequency oscillations, quantization errors and measurements disturbances.

This problem therefore requires further investigation and countermeasures on the accessible elements. For example, high frequency filtering or adaptive frequency tacking techniques could be used. Therefore, to identify the best technique for eliminating disturbances due to high frequency oscillations, an in-depth study was carried out into the causes of these oscillations, reported in chapter 5. The possible solutions and techniques that can be implemented in the future to improve observer's precision are reported in the conclusions.

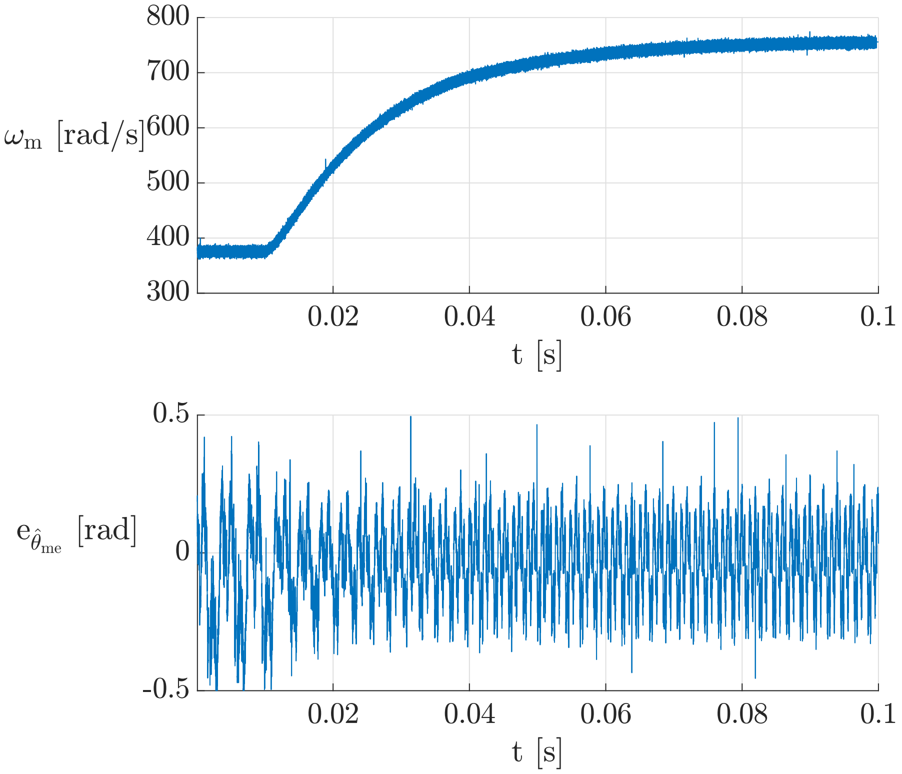

Figure 4.25: Measured rotor speed and rotor position estimation error during a step variation of the reference speed from 375 to 700 rpm.

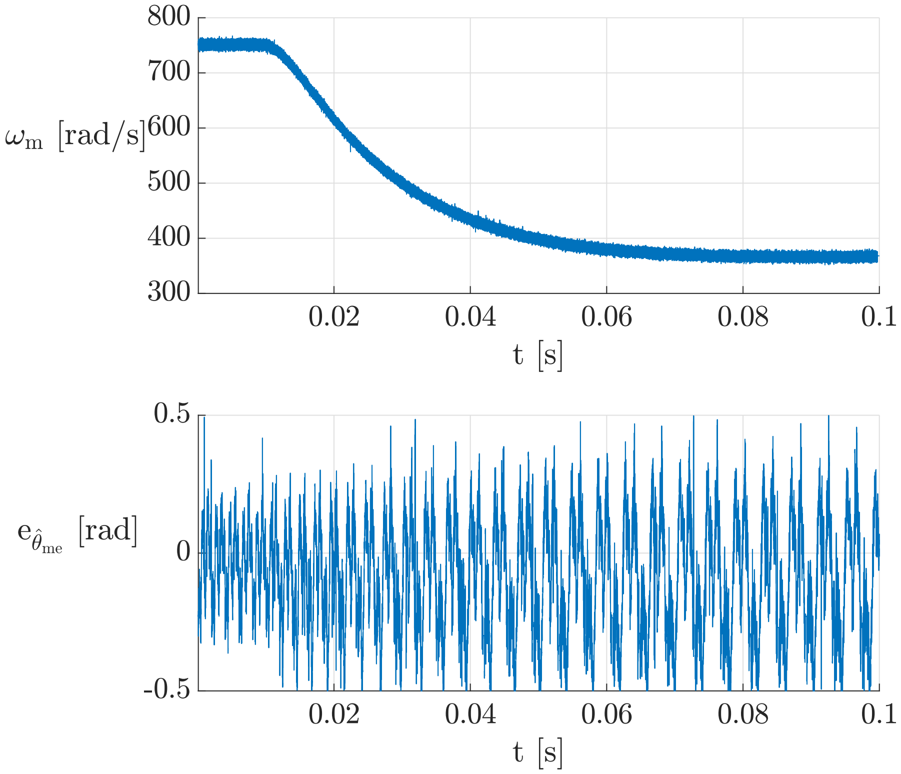

Figure 4.26: Measured rotor speed and rotor position estimation error during a step variation of the reference speed from 700 to 375 rpm.

4.5.4 *Step variation of torque reference*

In the end, the observer rejection capability to torque disturbances was tested, and the results are reported in figure 4.28. During these experimental tests, the SynRM was coupled with a PMSM which was used to maintain a constant speed during torque-step tests. An image of these motors is reported in figure 4.27.

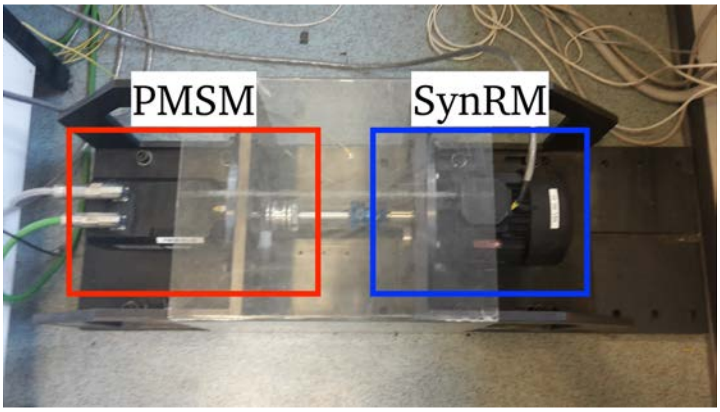

Figure 4.27: SynRM and PMSM used for the experimental tests.

At around $5\,ms$, as denoted by a red dotted line, a current trend variation can be noticed, following a torque reference step increase from

0 to 37% of τ_N. Anyway, even during this disturbance, the position estimation is still accurate, thus demonstrating the observer stability and proper functioning.

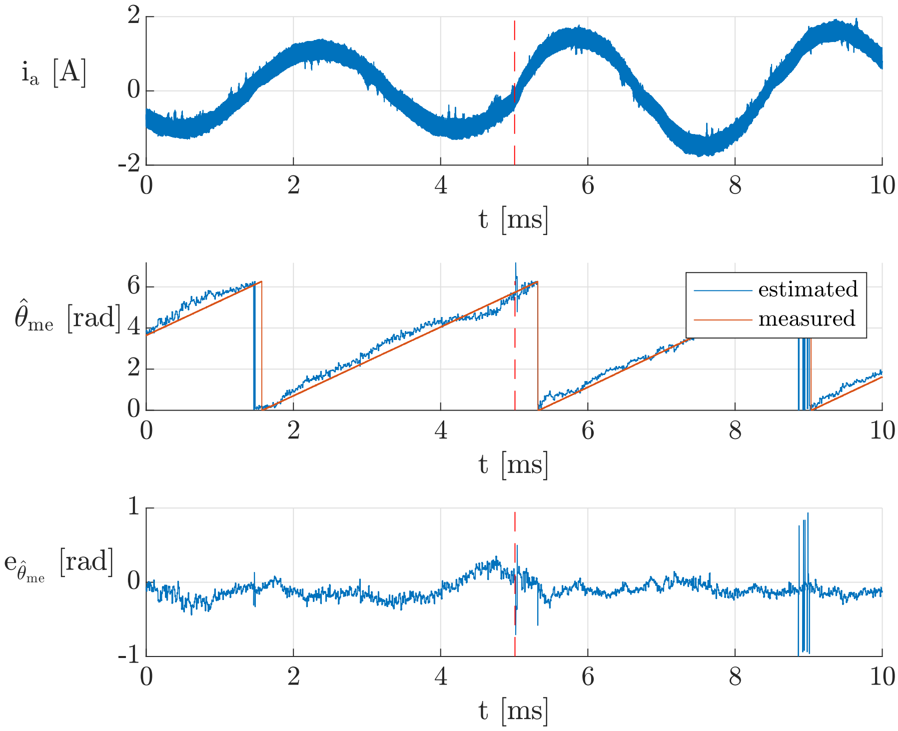

Figure 4.28: Phase current, estimated and measured rotor position and rotor position estimation error during a torque reference step variation.

5

HIGH-FREQUENCY OSCILLATIONS ANALYSIS

As described in the previous chapters, the phase currents high-frequency oscillations cause an incorrect current slope estimation, thus preventing a good position estimation. In this work, these disturbances have been reduced delaying the RLS enable signal. The main drawback of this technique is the RLS regression time window reduction, affecting the observer precision. Then, in order to develop a better technique which reduces this disturbance, a further investigation of oversampled current measurements was carried out. Moreover, to understand the high-frequency oscillations sources and effects, a model of the experimental setup including parasitic elements was developed using the tool *Simscape* for *Matlab Simulink*. In the future, this model could be used to simulate a sensorless control algorithm which filters the high frequency current oscillations.

5.1 SWITCHING TRANSIENTS ANALYSIS

Before trying to simulate the whole system, a focus on the oversampled current measurements was made, in order to identify the main phenomena affecting the current behaviour. Two different data sets were analysed, the former obtained using a SynRM and LEM current sensors, and the latter using an IM and both Rogowski coils and clamp meters.

5.1.1 *SynRM measurements*

The experimental results reported hereafter were collected using the motor used in the previous part of this thesis work, which parameters are reported in table 3.2, and using a LEM current sensor with a 150 kHz (-1 dB) bandwidth. From figures 5.1 and 5.2 many phenomena can be noticed:

- both low and high frequency oscillations affect phase currents;
- the high and low frequency oscillations have a frequency of around 2.5 MHz and 60 kHz, respectively;
- the low frequency ones appear on a phase current when the corresponding inverter leg switches;
- if the current is positive, the low-frequency oscillations start when the upper IGBT switches, while if the current is negative they start when the lower one switches;

- the first low-frequency peak is always a positive peak, while the second one is always a negative peak;
- when current is positive, high frequency oscillations are superimposed on the first low frequency peak, while when current is negative, they are superimposed on the second peak;
- when high frequency oscillations affect a phase current, after a commutation of its corresponding inverter leg, the same high frequency oscillations appear on the other phase currents, while the low frequency peaks appear with a very lower amplitude.

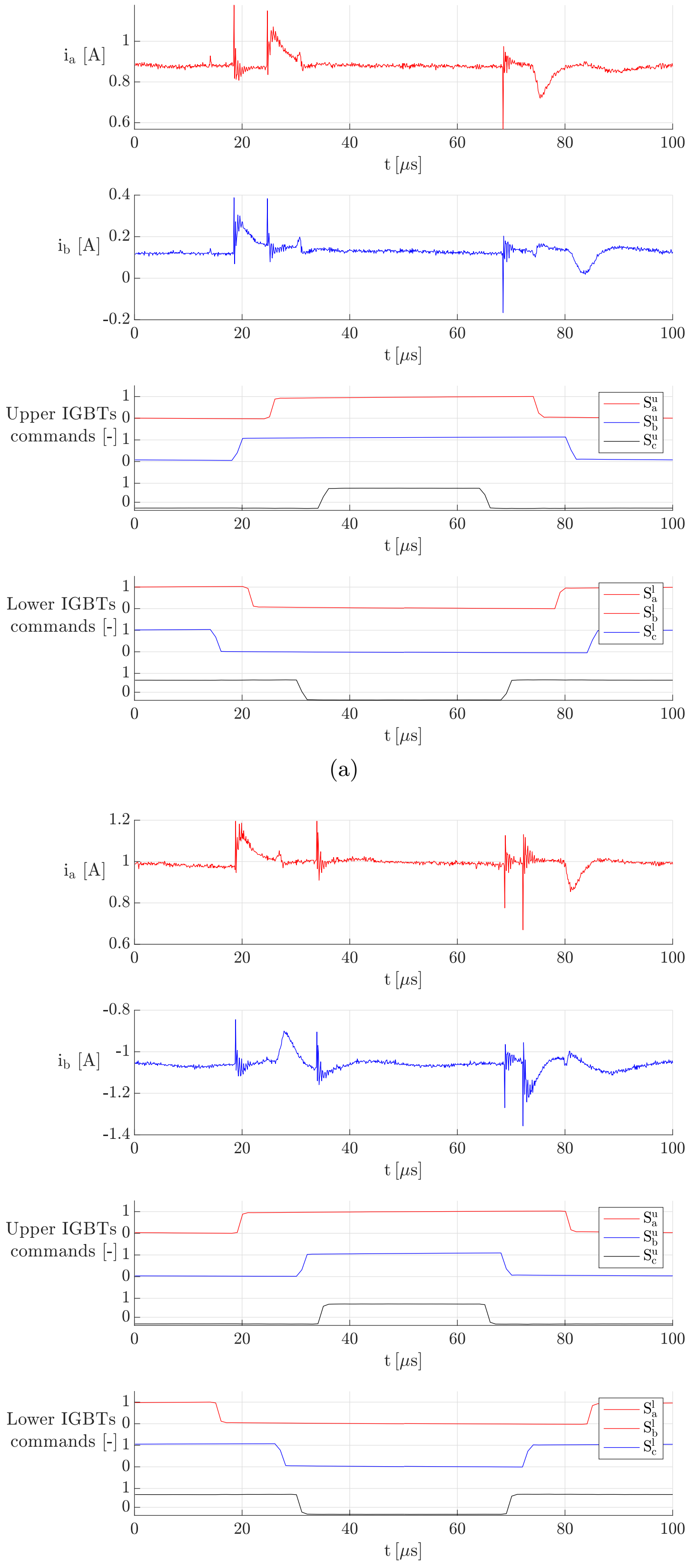

(a)

(b)

Figure 5.1: Oversampled currents i_a , i_b and IGBTs switching commands, when $i_a > 0$, $i_b > 0$ (5.1a) or when $i_a > 0$, $i_b < 0$ (5.1b).

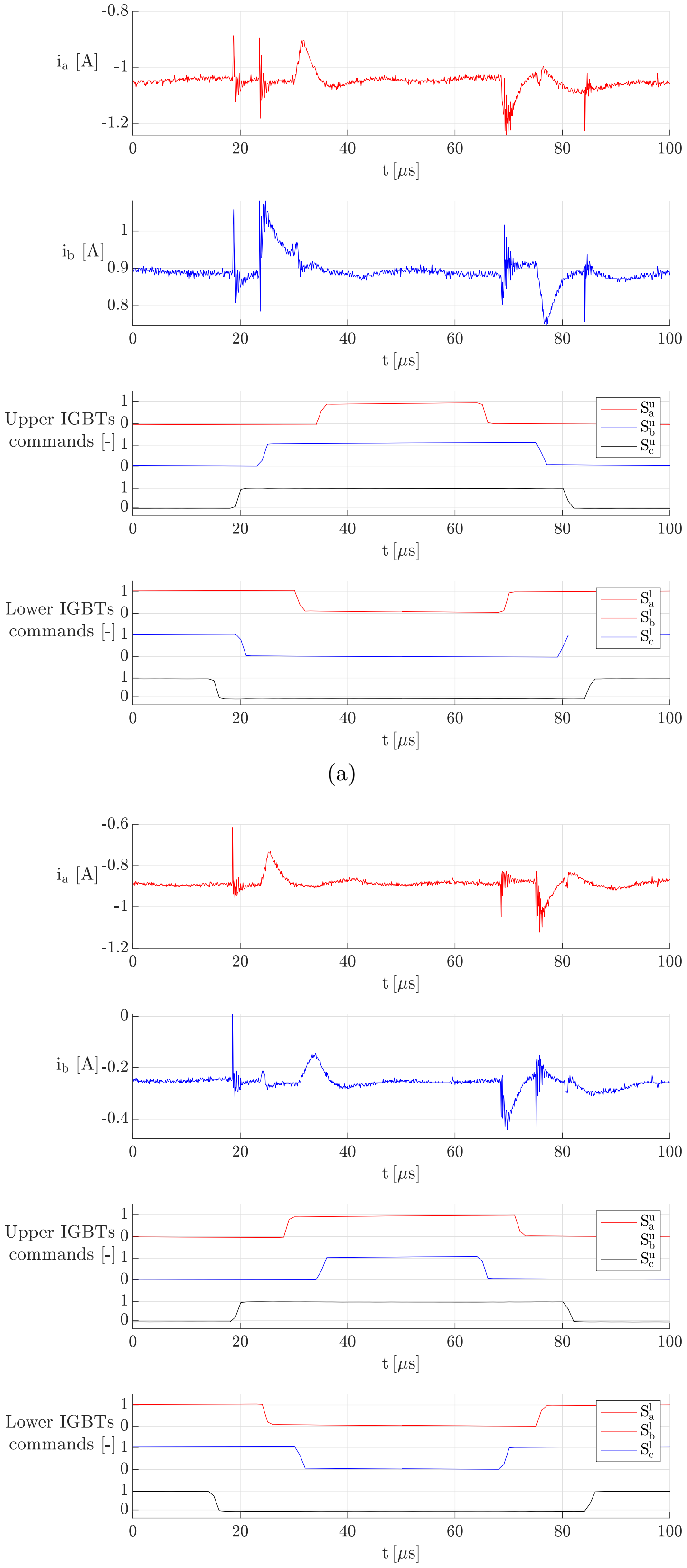

(a)

(b)

Figure 5.2: Oversampled currents i_a, i_b and IGBTs switching commands, when $i_a < 0$, $i_b > 0$ (5.2a) or when $i_a < 0$, $i_b < 0$ (5.2b).

5.1.2 *Induction motor*

5.1.2.1 *Experimental setup*

The Induction Motor (IM) parameters used for the following tests are reported in table 5.1, while the cable was 2 m long.

In these experiments, line current is measured in phase a, with two measurement devices namely clamp-meter (Ia_{TCP}) and Rogowski coil (Ia_{Rog}), in the few μs after the inverter leg a switches. The former sensor's bandwidth and sensitivity are DC-100 kHz and 100mV/s, while the latter's parameters are a bandwidth of 0.1 Hz - 16 MHz and a 20 mV/A sensitivity.

The analog signals obtained from the measurement devices are sampled using an oscilloscope, whose sampling frequency was 250MHz. The maximum number of points measured in a single data acquisition is defined by the storage memory of the oscilloscope used (*Agilent DSO1024*), which is 10240.

5.1.2.2 *Comparsion between clamp-meter and Rogowski coil measurements*

Figure 5.3 shows the experimental results obtained using both the clamp-meter and the Rogowski coil. It can be noticed that using the former one the high frequency oscillations are eliminated, but some low frequency oscillations are introduced. A number of 20 different measurements with different current levels are plotted in the same figure.

Moreover, they are very similar to the low frequency oscillations reported in figures 5.1 and 5.2 thus they may be due to the low bandwidth of the current sensors used in these experiments.

The frequency of the oscillations measured with the Rogowski coil is around 5.5 MHz, while the frequency of the oscillations measured with the clamp meter is around 200 kHz.

Table 5.1: IM parameters

Parameter	Value
Nominal current - Delta Δ	7.8 A
Nominal current - Wye Y	4.5 A
Nominal voltage - Delta Δ	220 V
Nominal voltage - Wye Y Δ	380 A
Nominal power	1.8 kW
Power factor	0.8

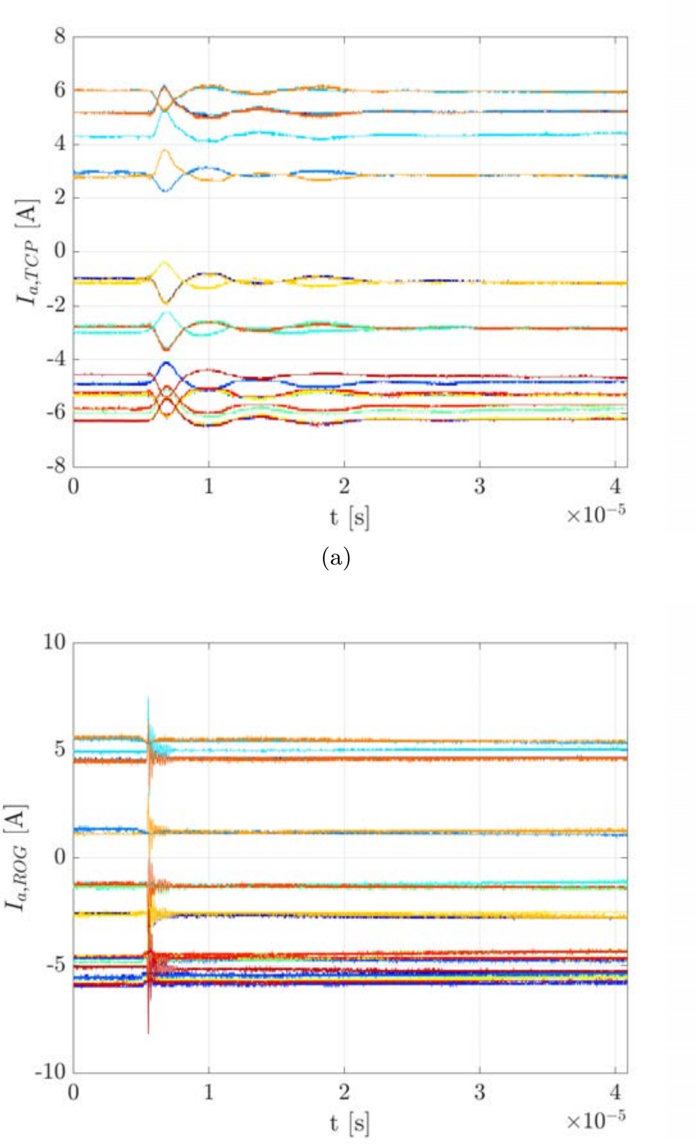

(a)

(b)

Figure 5.3: Oversampled current i_a using a clamp meter (5.3a) or a Rogowski-coil (5.3b). [17]

5.1.2.3 *Comparison between positive and negative switching*

In the results obtained using the IM and the Rogowski coils the high frequency current oscillations are different if the conductive element is the IGBT or the diode and it is influenced by the current sign. The phase voltage Uan with repect to the DC bus mid point and the current oscillations during positive and negative switching are reported in figures 5.4a and 5.4b, respectively.

These figures show that the oscillations behaviour is similar to the one observed in the previous experiments, reported in paragraph 5.1.1. These oscillations can be explained analysing the conductive elements of a single phase, both with positive and negative current.

When the line current is positive, as shown in figure 5.5, we observe current oscillations only during a positive switching that is when a positive voltage is applied after the switching transition. When the positive voltage is applied and when the current is positive, the IGBT of the upper leg conducts. Prior to the switching instant the applied voltage was negative and so the diode of the lower leg was conducting. Thus, only when the transition of the current occurs from the diode to the IGBT (5.5a) the oscillations are observed. The oscillations in the current are not observed during the transition of the current from the IGBT to the diode (5.5b).

When the line current is negative, we observe oscillations in the current only during negative switching. In this case, before the switching instant, the applied voltage is positive and the current is negative, which implies that the diode of the upper leg was conducting. After the switching instant, the applied voltage is negative and also the current is negative, so the conducting device is the IGBT of the lower leg. Thus, also in this case, it is only for the transition of the current from diode to IGBT (5.5c) that the oscillations are evident. For the other transition (IGBT to diode 5.5d), no oscillations are observed.

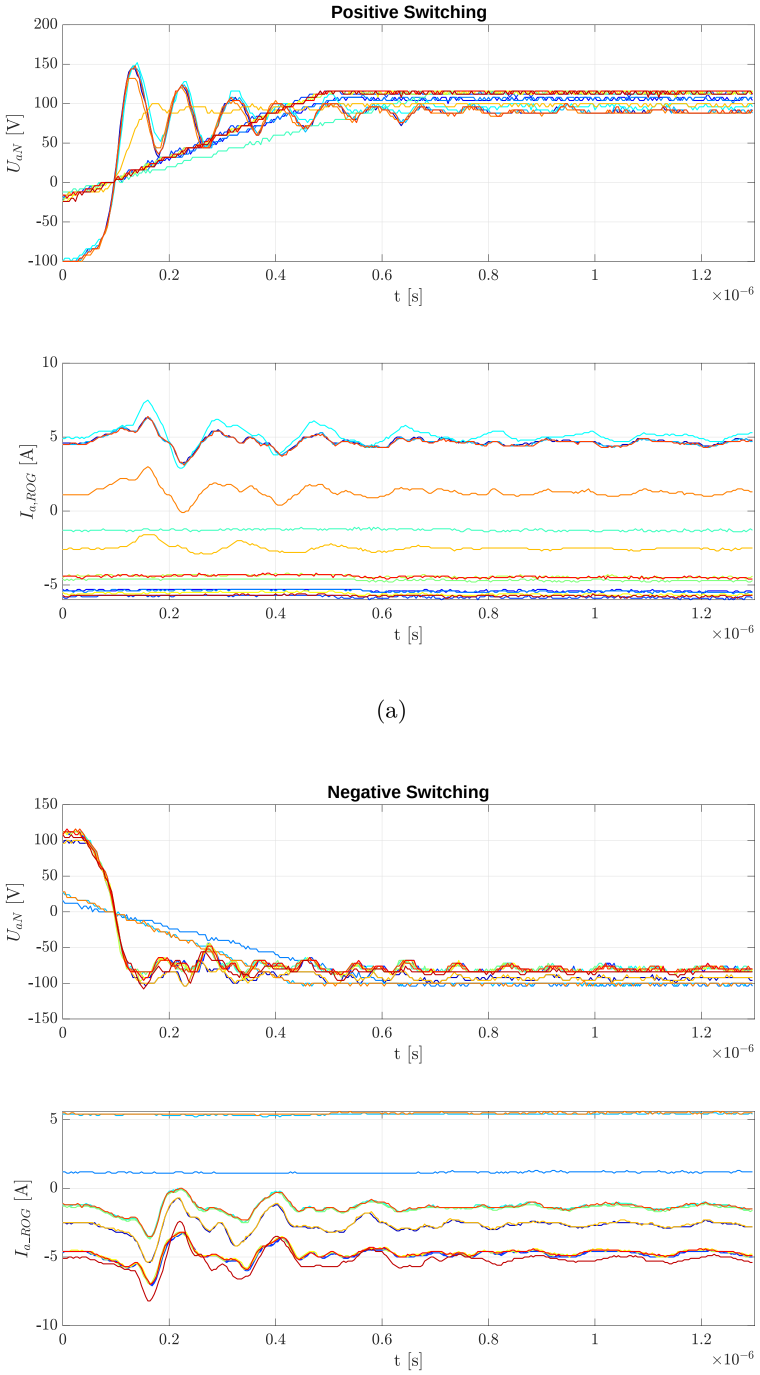

(a)

(b)

Figure 5.4: Oversampled current i_a and voltage v_a during positive (5.4a) or negative (5.4b) switching. [18]

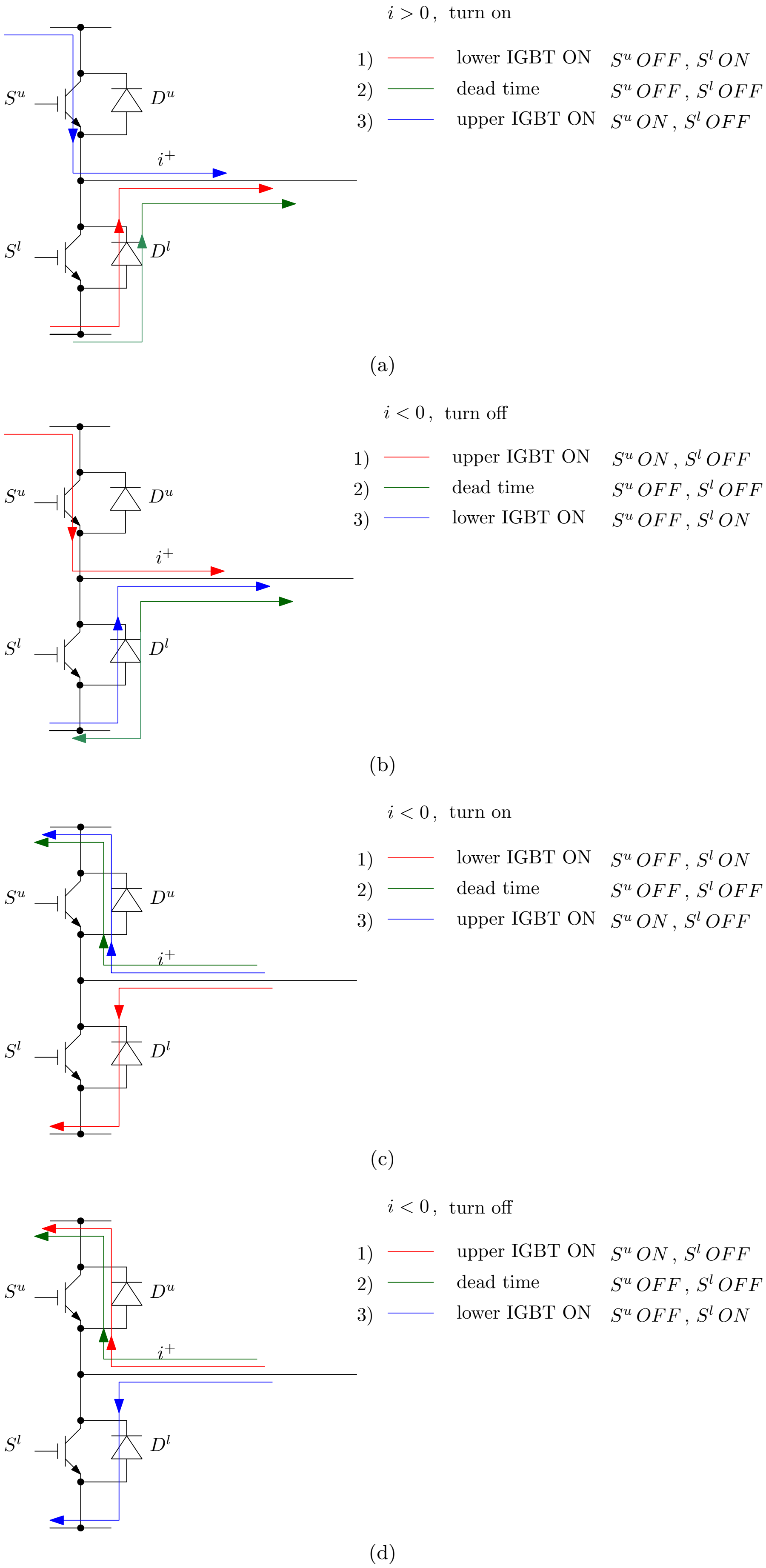

Figure 5.5: Inverter's leg currents, first commutation with i > 0 (5.5a), second commutation with i > 0 (5.5b), first commutation with i < 0 (5.5c), second commutation with i < 0 (5.5d).

5.1.2.4 *Comparison between short and long cable*

In order to understand whether the connecting cable length between inverter and the induction motor has some effect on the current transient, line current measurements were acquired for different cable lengths. Further, Fourier analysis were performed on the measurements to observe the effect of the cable length. The short cable was 2 m long, while the long one was 4 m long.

Figure 5.6 shows that using a longer cable, both the oscillations frequency and amplitude are reduced. This effect can be explained with the increase of parasitic resistances and capacitances, which are proportional to the cable length [11].

5.1.2.5 *Comparison with bibliographic results*

Figure 5.7 shows the currents, measured using Hall sensors, reported in [19]. The upper graphs display a snapshot of two phase currents, denoted as Y and R, while the bottom one reports an expanded view of these currents.

The oscillations reported in these figures are quite similar to the ones noticed in the experimental results obtained previously in 5.1 and 5.2. These waveforms, indeed, are both affected by high frequency oscillations, but only the phase which is switching (Y in the expanded view) is affected by low frequency oscillations.

Therefore, these results are consistent with those obtained in our experimental tests.

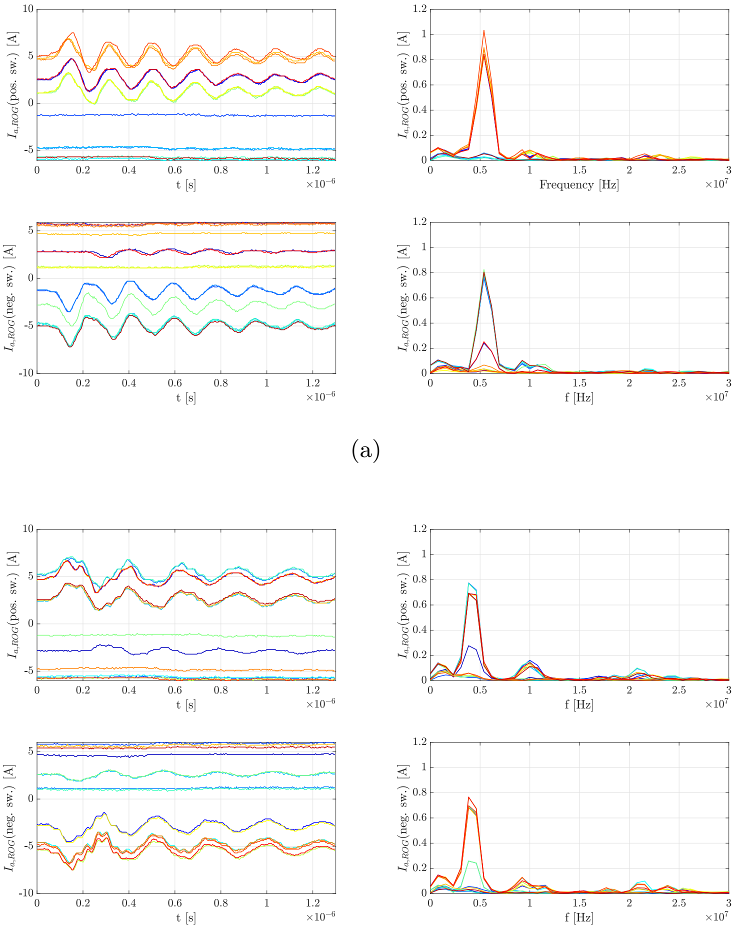

(a)

(b)

Figure 5.6: Oversampled current i_a and its frequency content, for a short (5.6a) or long (5.6b) cable length. [18]

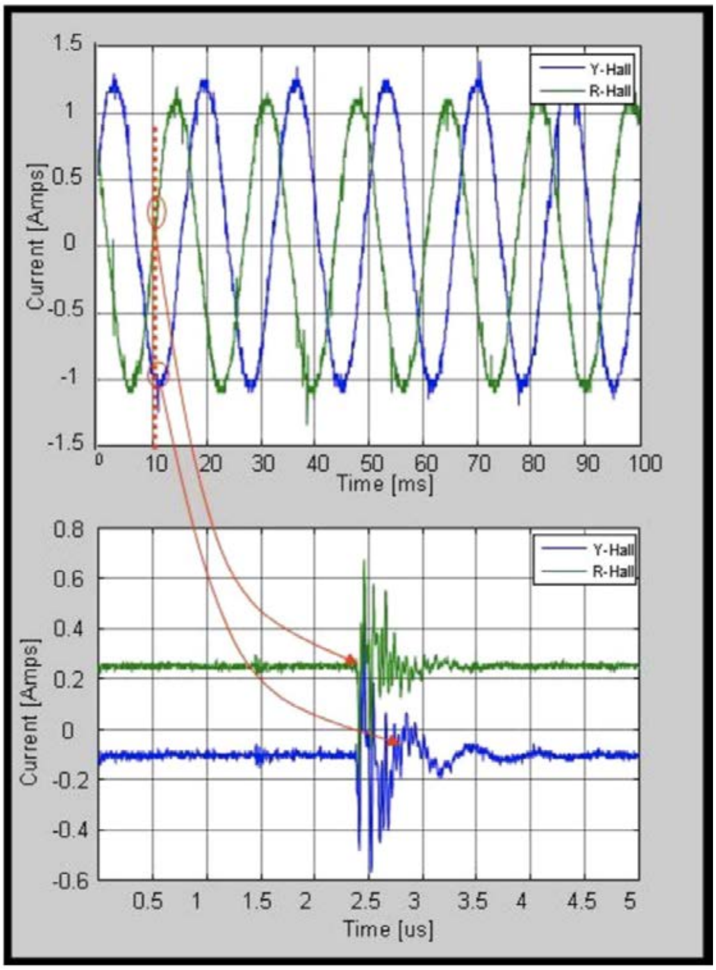

Figure 5.7: (Top) Phase motor current. (Bottom) Expanded view showing the current ringing oscillation produced during transistor switching. [19]

5.2 EXPERIMENTAL SETUP MODELLING

Thanks to the theoretical and experimental results analysis, a drive model was developed, in order to simulate the measured high and low frequency current oscillations, which affect the position estimation accuracy.

5.2.1 *Drive ideal model*

The ideal model of the experimental system used for this work is reported in figure 5.8: it consists of a three-phase inverter, three cables and the motor. Due to the ideality hypothesis no parasitic element is reported.

Anyway, every element of the described experimental system has parasitic elements, which are hereafter described.

5.2.2 *Drive real model*

The inverter consists of three legs, each composed of two power IGBTs with two free-wheeling power diodes. In the following paragraphs, the models of power diodes and IGBTs including parasitic elements are presented and their switching characteristics are described.

5.2.2.1 *Diode*

The switching properties of a diode are often given on specification sheets for diode currents with a specified time rate of change, $\frac{di}{dt}$. The reason for this selection is that power diodes are very often used in circuits containing inductances that control the rate of change of the current, or they are used as free-wheeling diodes where the turn-off of a solid-state device controls $\frac{di}{dt}$, as reported in [20].

The switching waveforms are reported in figure 5.9, whose accurate description can be found in [20].

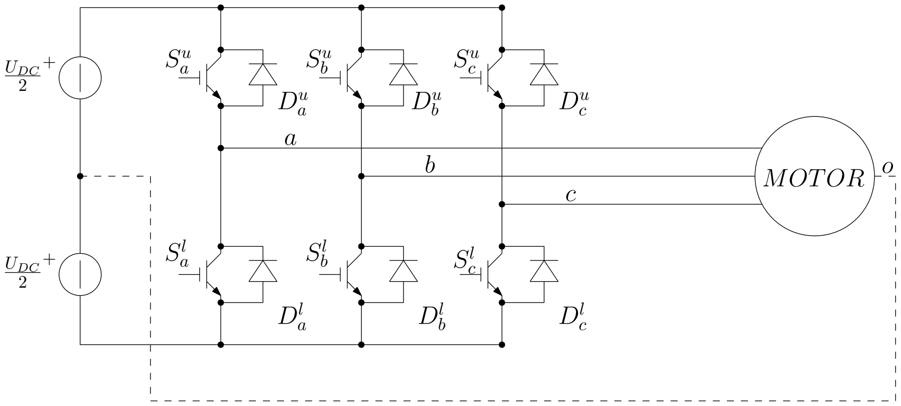

Figure 5.8: Ideal drive schematic.

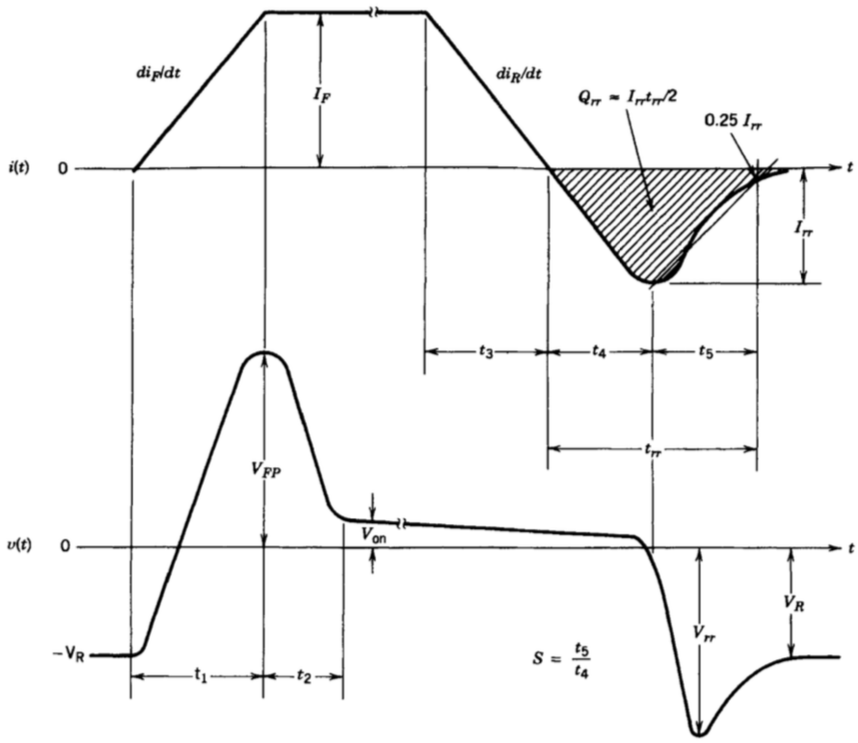

Figure 5.9: Voltage and current waveforms for a power diode driven by currents with a specified rate of rise during turn-on and a specified rate of fall during turn-off. [20]

For this component the main parasitic element is the reverse recovery charge Q_{rr}, which causes current and voltage spikes at diode turn-off. Moreover, a voltage spike can be noticed at diode turn-on, due to depletion region reduction time.

5.2.2.2 *IGBT*

The typical circuit used for IGBTs testing is reported in figure 5.10, where S is the IGBT to be tested, D_{ideal} is an ideal diode, L is an inductor whose current I_L is assumed to be constant, while V_{GG} is a voltage generator which generates a square-wave voltage.

The switching waveforms are reported in figure 5.11 and 5.12, and their accurate description can be found in [20].

For this component the main parasitic elements are three capacitances and three resistors: $C_{GE}, C_{GC}, C_{CE}, R_G, R_E, R_C$ reported in figure 5.13, which cause current and voltage spikes at IGBTs turn-on and turn-off.

5.2.2.3 *Cable*

The cable model, as reported in [21], consists of the cable series resistance R_{s1} and inductance L_{s1}, with in series a resistor R_{s2} and an inductor L_{s2}, in parallel, to consider the skin and proximity effects, as

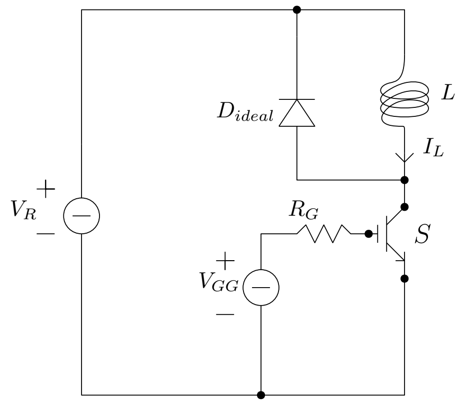

Figure 5.10: IGBT testing circuit.

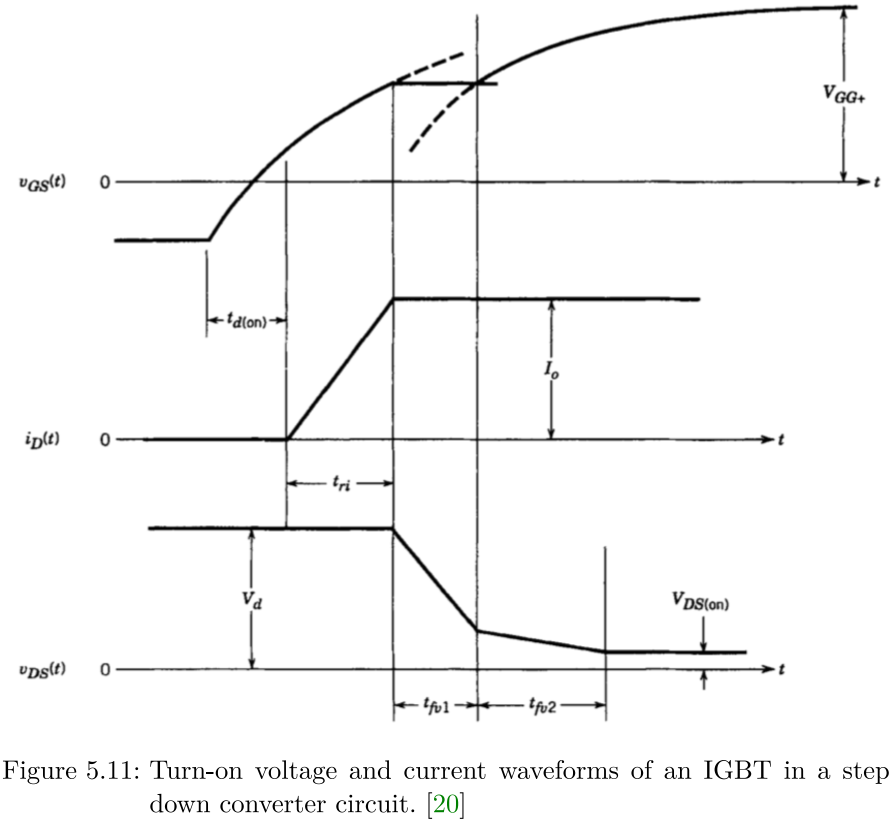

Figure 5.11: Turn-on voltage and current waveforms of an IGBT in a step-down converter circuit. [20]

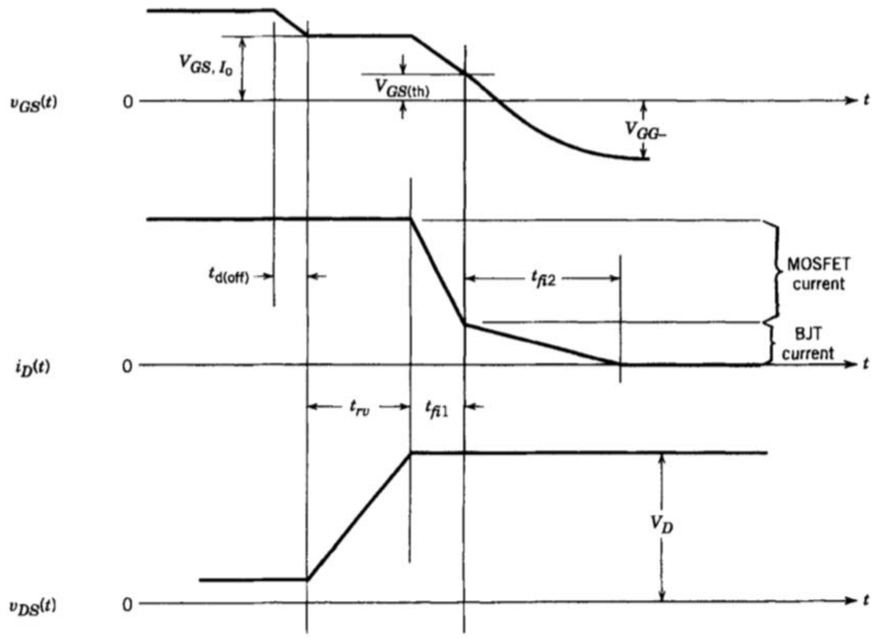

Figure 5.12: Turn-off voltage and current waveforms of an IGBT embedded in a step-down converter circuit. [20]

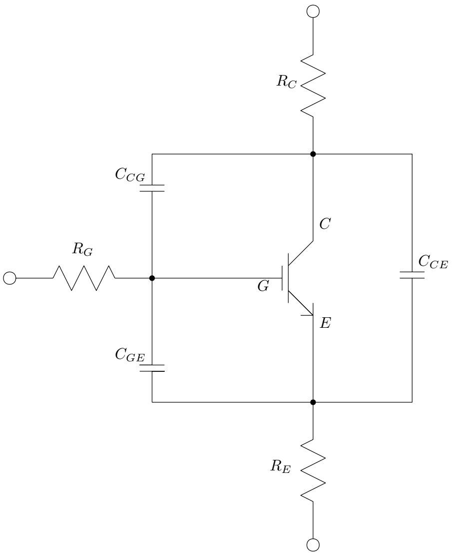

Figure 5.13: IGBT model with parasitic elements.

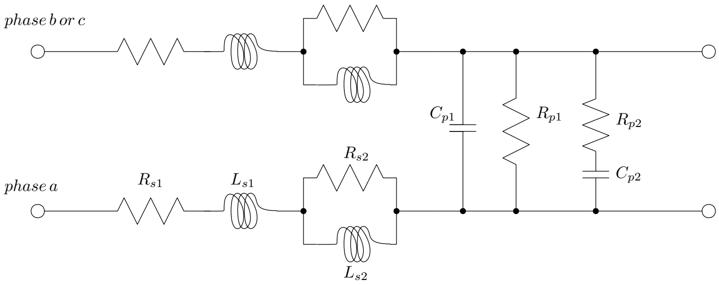

Figure 5.14: Cable model with parasitic elements.

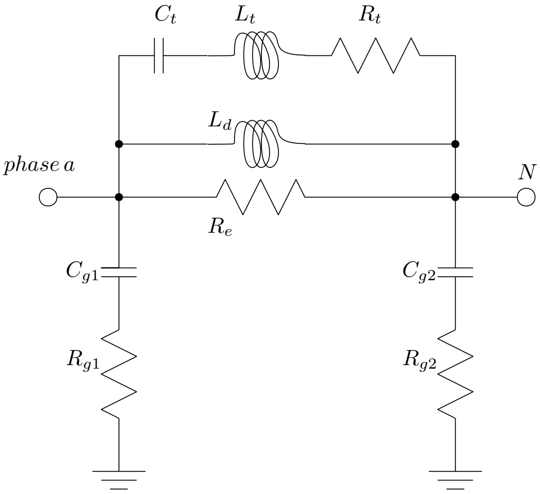

Figure 5.15: High frequency motor model with parasitic elements.

suggested in [11]. A parallel capacitance C_{p1} and resistance R_{p1} represent the coupling between the different wires.
Moreover, the series of a resistance R_{p2} and a capacitance C_{p2} are added between the different wires, in order to include dielectric effects. The cable model schematic obtained is reported in figure 5.14.

5.2.2.4 *Motor*

The main parasitic elements considered for the motor model, as reported in [11], are:

- R_e to consider the iron losses;
- $R_{g1,2}$ and $C_{g1,2}$ which represent the winding to ground coupling;
- L_d to consider the leakage magnetic flux;
- C_t, R_t, L_t, to consider the turn-to-turn impedance.

Then, this high-frequency motor model, reported in figure 5.15, is added in parallel to the low-frequency model.

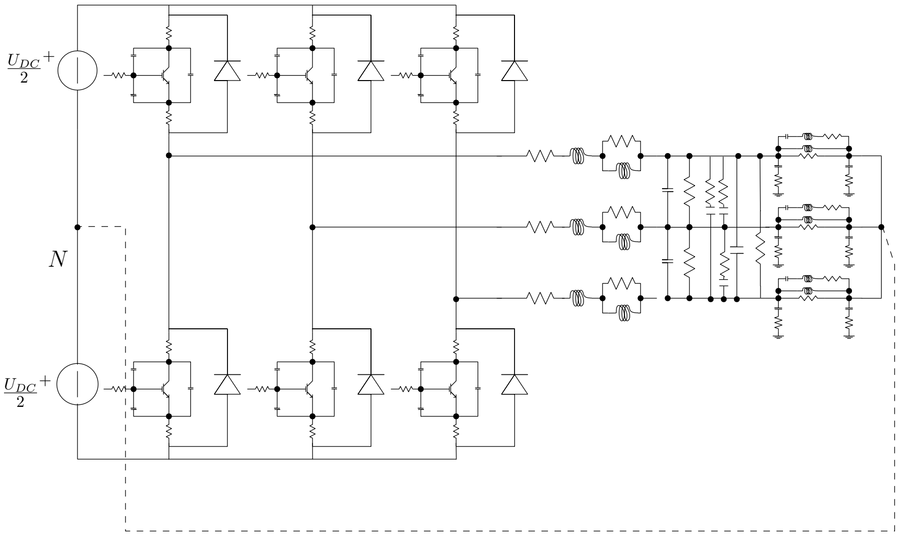

Figure 5.16: Inverter with parasitic elements.

5.2.2.5 *Final model*

The final model of the experimental setup, which considers all the parasitic elements described, is reported in 5.16.

5.3 DRIVE SIMULATIONS WITH PARASITIC EFFECT INCLUSION

Using the final model of the experimental setup for simulations, could allow, in future studies, to develop and test advanced techniques to eliminate the estimation disturbances, thus improving the observers accuracy. The Simulink schematic used for the simulations is reported in figure 5.17.

In this model both real and ideal elements are considered, in order to compare the results obtained with or without parasitic elements.

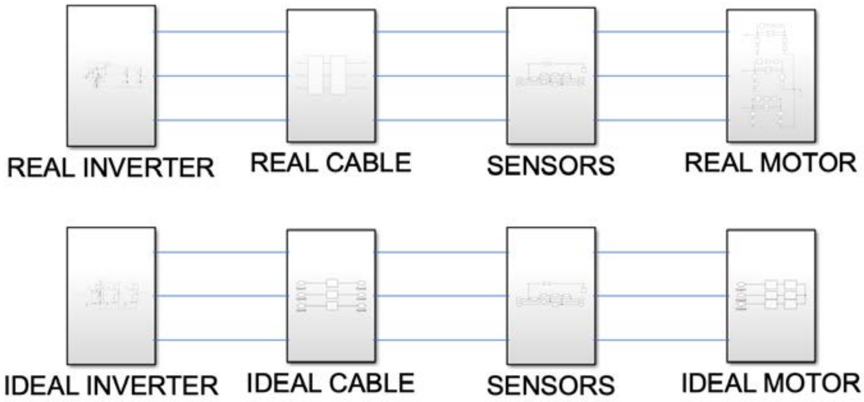

Figure 5.17: Simulink model used for parasitic elements simulations.

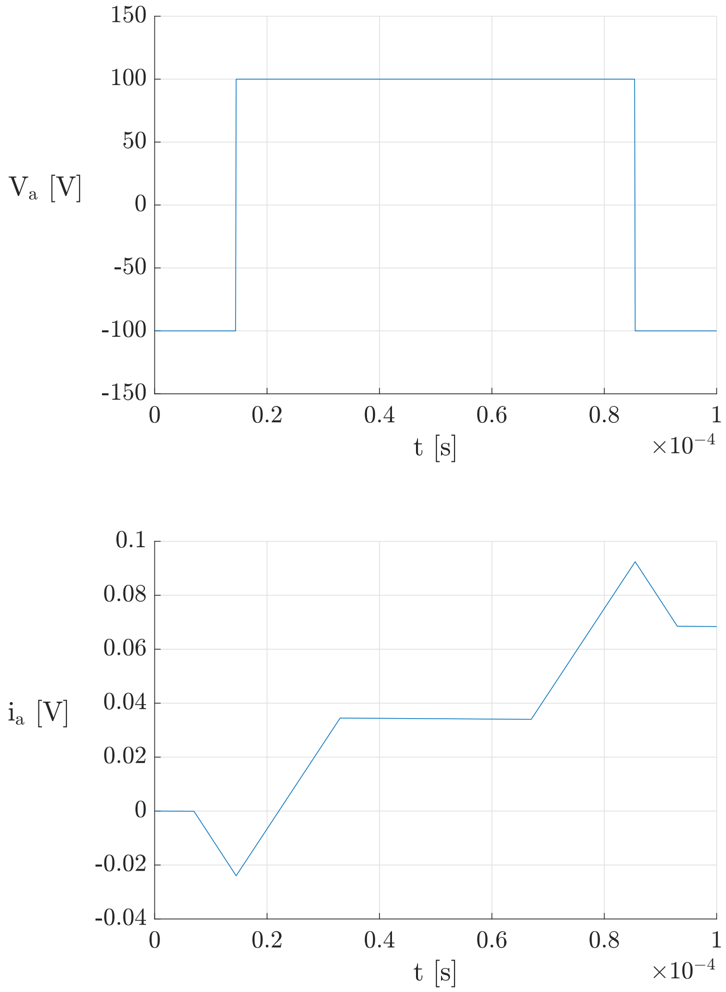

Figure 5.18: Phase voltage V_a with respect to the DC bus mid point and the phase current i_a obtained simulating the drive ideal model.

5.3.1 *Parasitic elements introduction*

The first simulation was realised using ideal components, in order to verify if the model is consistent with the theoretical formulas reported in chapter 2. This simulation was realised using the same PWM period of the experimental tests, i.e. $T_{PWM} = 10\mu s$, and the duty-cycles of the three phases were: $\delta_a = 90\%$, $\delta_b = 30\%$, $\delta_c = 75\%$. An R-L load was simulated, using the parameters R_s and L_s of the induction motor used in the second part of this thesis, which values are reported in table 5.6.

The results are reported in figure 5.18, and are in accordance with the theoretical analysis reported in 2.2.2.1, i.e. no high-frequency oscillations appear.

Then, different simulations were carried out, in order to introduce one at a time each component with parasitic elements and to analyse the different high frequency oscillations at switches turn-on and turn-off. When introducing the real inverter model, the commutations, indeed,

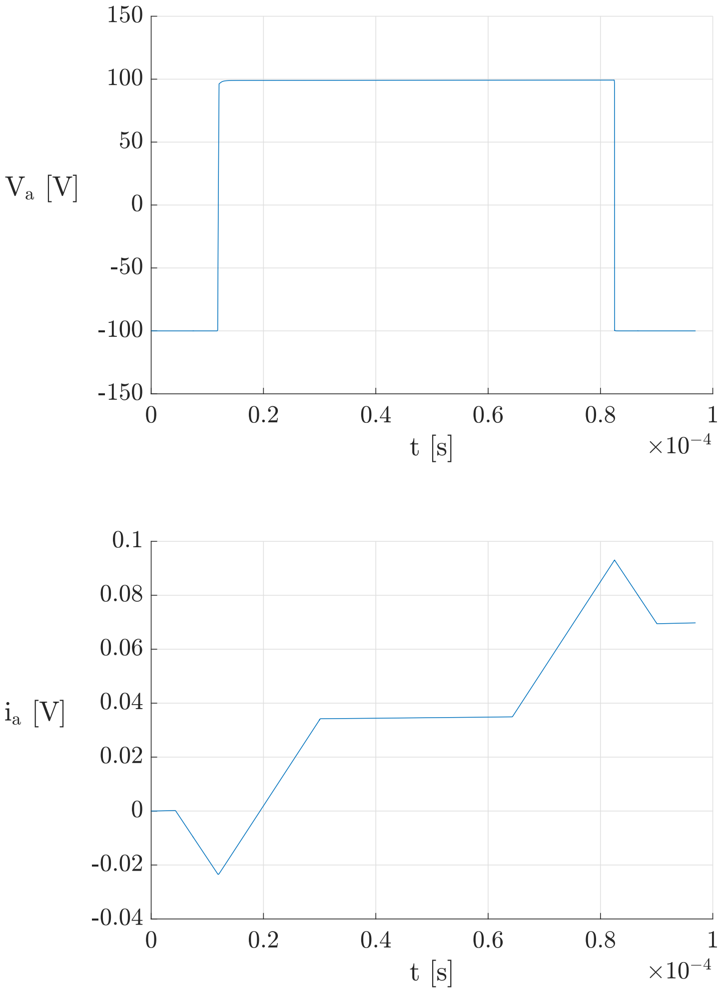

Figure 5.19: Phase voltage V_a with respect to the DC bus mid point and the phase current i_a obtained simulating the real inverter - ideal cable - ideal motor model.

occur less quickly, therefore the voltage variations are softer, especially at turn-on, as reported in 5.19. The difference between turn on and turn off is due to the different switching behaviour of IGBT and diode.

Figure 5.20 shows that when the real cable model is introduced, the inductances and capacitances in the system cause a resonance, and voltage oscillations are noticed. In the end, by introducing the high frequency motor model, current oscillations are also introduced, as reported in figures 5.21 and 5.22. Also the mutual coupling between phases can be noticed and it can be seen that the introduction of the high frequency motor model introduces a higher frequency harmonic component. Moreover it can be noticed that the high frequency oscillations are much lower at turn off, because the switching element is the diode.

These initial simulations were carried out using the cable and motor parasitic elements values reported in [3], because it was not possible to measure them on our experimental setup. The motor used in [3] was a

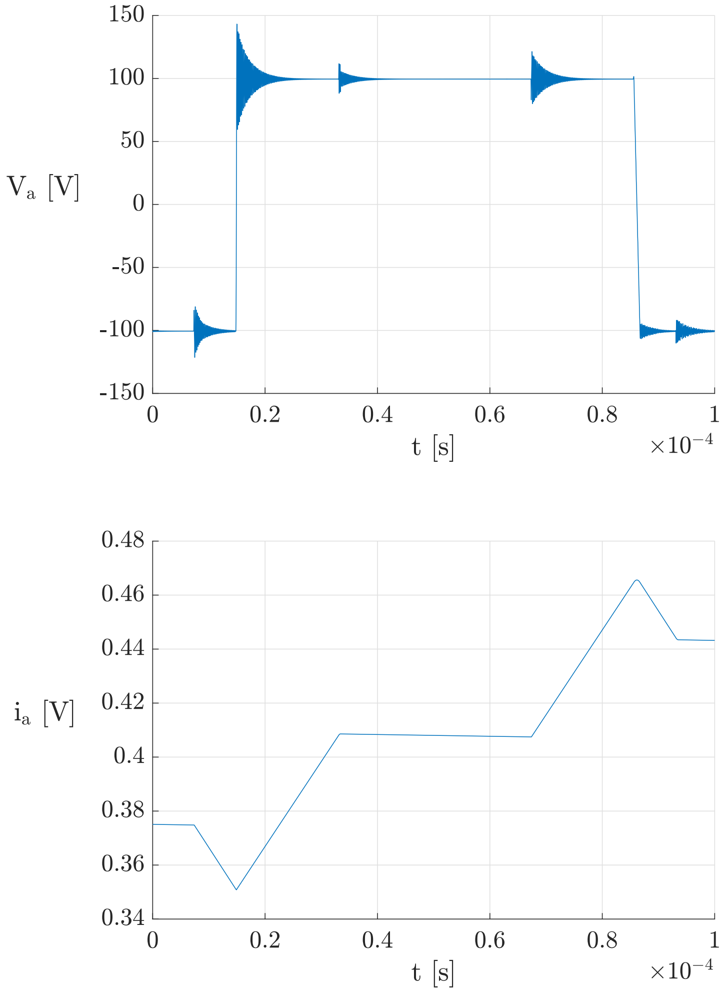

Figure 5.20: Phase voltage V_a with respect to the DC bus mid point and the phase current i_a obtained simulating the real inverter and real cable and ideal motor model.

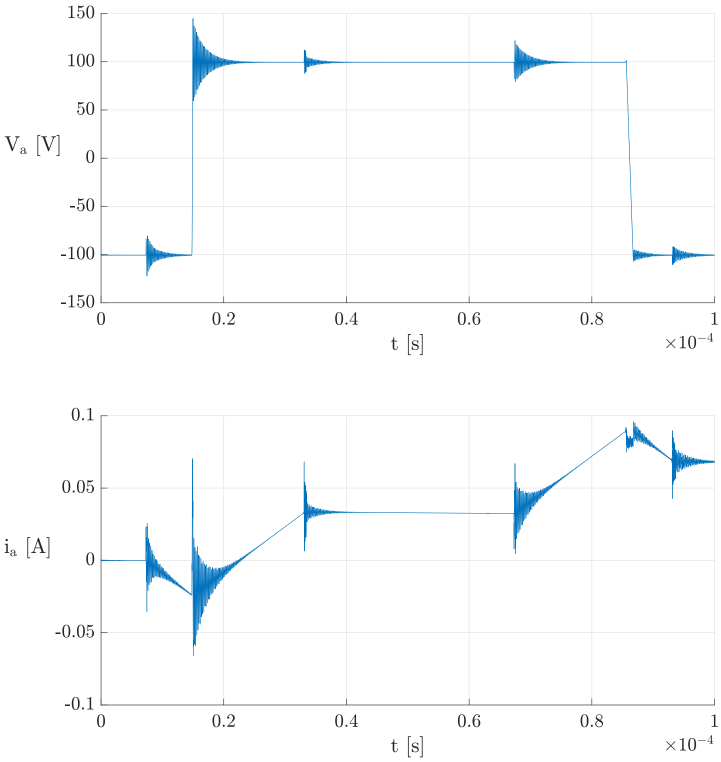

Figure 5.21: Phase voltage V_a with respect to the DC bus mid point and the phase current i_a obtained simulating the real inverter, cable and motor model.

PMSM with a rated power of 3.82 kW.
Using these model two different main oscillations frequencies are observed: one at 4.4 Mhz, which affects both current and voltage, and a current oscillation at 39.5 MHz.

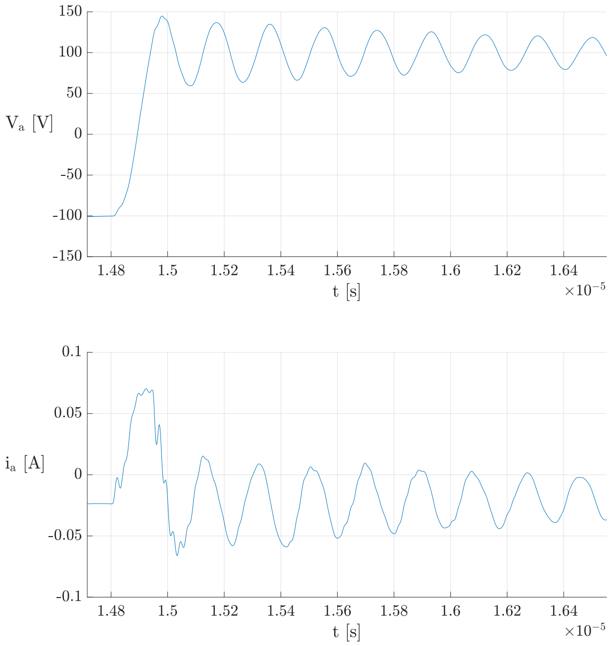

Figure 5.22: Zoom of phase voltage $\mathrm{V_a}$ with respect to the DC bus mid point and the phase current $\mathrm{i_a}$ obtained simulating the real inverter, cable and motor model.

5.3.2 *Parameters variations effects*

Different simulations were carried out, in which the most significant model parameters have been changed one at a time (multiplying them for a gain of 10, 1 or 0.1), in order to observe their effect on high frequency oscillations.

Figure 5.23 shows that increasing the cable length the voltage and current oscillations frequency decreases, as in the experimental results. Moreover, the voltage oscillations amplitude increases with the cable length, while the current amplitude has a maximum with a 4 m cable length.

From figures 5.24 and 5.25, it can be observed that by varying C_{g1} the voltage oscillations amplitude does not change a lot, while the currents oscillations amplitude increases with the C_{G1} capacitance value. Also C_{g2} influences the current oscillation frequency, and it generates a low frequency oscillation when it has a big value. However, C_t has almost no effect on voltage or current oscillations.

All the other model parameters influence the oscillations waveforms, but, for sake of clarity, instead of the simulations obtained varying these parameters, tables 5.2 and 5.3 are reported, which describe their effects on voltage and current oscillations.

The tables legend is the following:

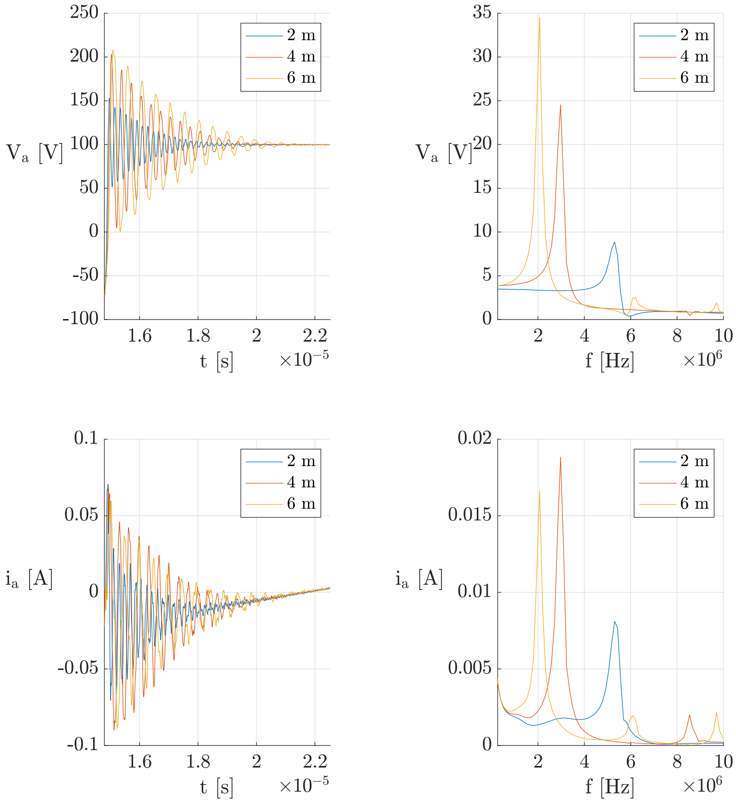

Figure 5.23: Simulations results with different cable lengths.

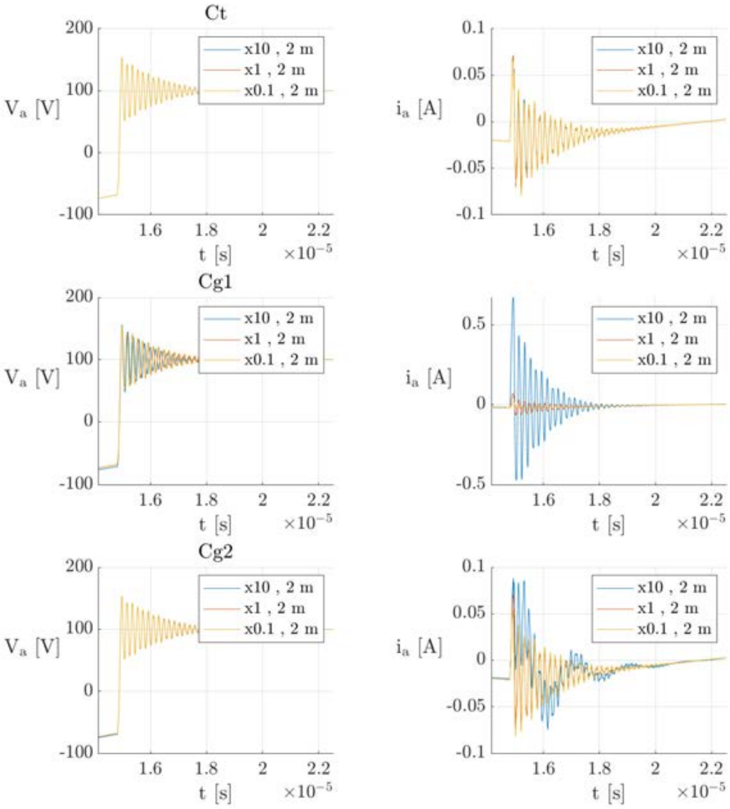

Figure 5.24: Simulations results changing the values of C_t, C_{g1}, C_{g2}.

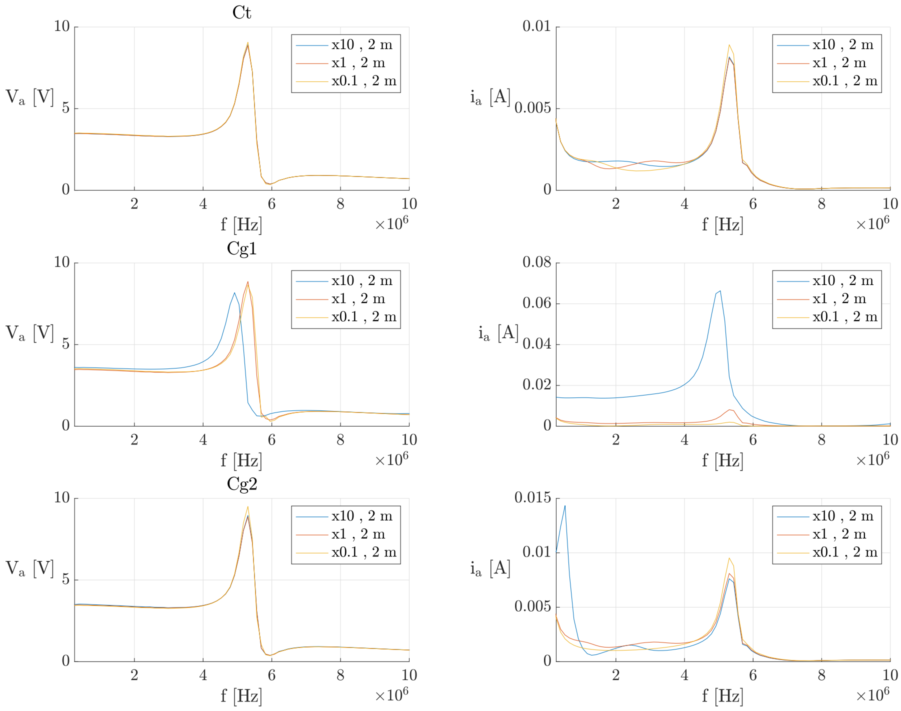

Figure 5.25: FFT of the simulations results obtained changing the values of C_t, C_{g1}, C_{g2}.

- negligible effect: n
- considerable influence (less than 50%) : yellow coloured
- great influence (more than 50%): red coloured

Moreover, the percentages reported in the tables represent the difference between voltage (or current) amplitude (or frequency), measured with the nominal value and the one measured using the nominal value divided (or multiplied) by 10.

In order to find the parameters needed for the simulations, a trial-and-error method was used, comparing the simulations with the experimental results obtained using the Induction Motor, reported in 5.1.2.

The final simulation, which waveform is close to the experimental results, is reported in figure 5.27.

The experimental measured oscillations are of ±50 V at around 10 MHz and ±2.35 A at 5.56 MHz, while the simulated ones are of ±48 V at around 4 MHz and ±2.3 A at 3.76 MHz, so it can be considered that these oscillations closely reproduced with respect to the magnitude and the resulting oscillation frequencies have still a considerable degree of inaccuracy.

However, the main goal is not to perfectly reproduce the experimental data, but to find a valid model of the experimental setup, which qualitatively reproduces the measurements, as a first step for future studies. Moreover, it was noticed that the simulated oscillations frequency with

Table 5.2: Motor parameters effects

Parameter	Voltage		Current	
	Amplitude	Frequency	Amplitude	Frequency
L_d	n	n	94%	n
R_t	n	n	n	n
C_t	n	n	10%	n
L_t	n	n	n	n
R_{g1}	n	n	n	n
R_{g2}	n	n	n	n
R_e	n	n	58%	n
C_{g1}	7.3%	7.7%	750%	7.2%
C_{g2}	n	n	17.6%	n

Table 5.3: Cable parameters effects

Parameter	Voltage		Current	
	Amplitude	Frequency	Amplitude	Frequency
C_{p1}	317%	68%	75%	68%
C_{p2}	n	n	n	n
R_{p1}	n	n	n	n
R_{p2}	n	n	n	n
L_{s1}	650%	68%	260%	68%
L_{s2}	n	n	n	n
R_{s1}	n	n	n	n
R_{s2}	43%	n	47%	n

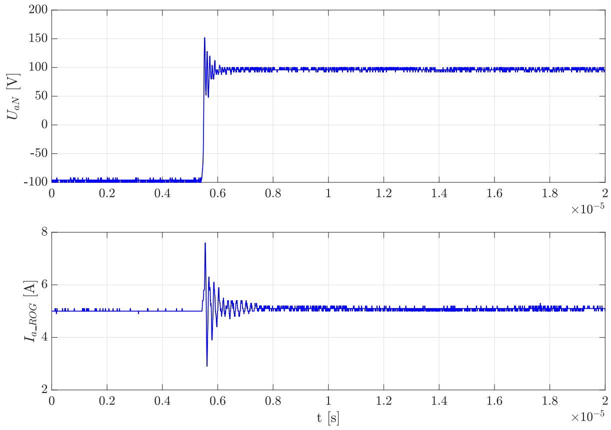

Figure 5.26: Experimental results obtained using the Induction Motor.

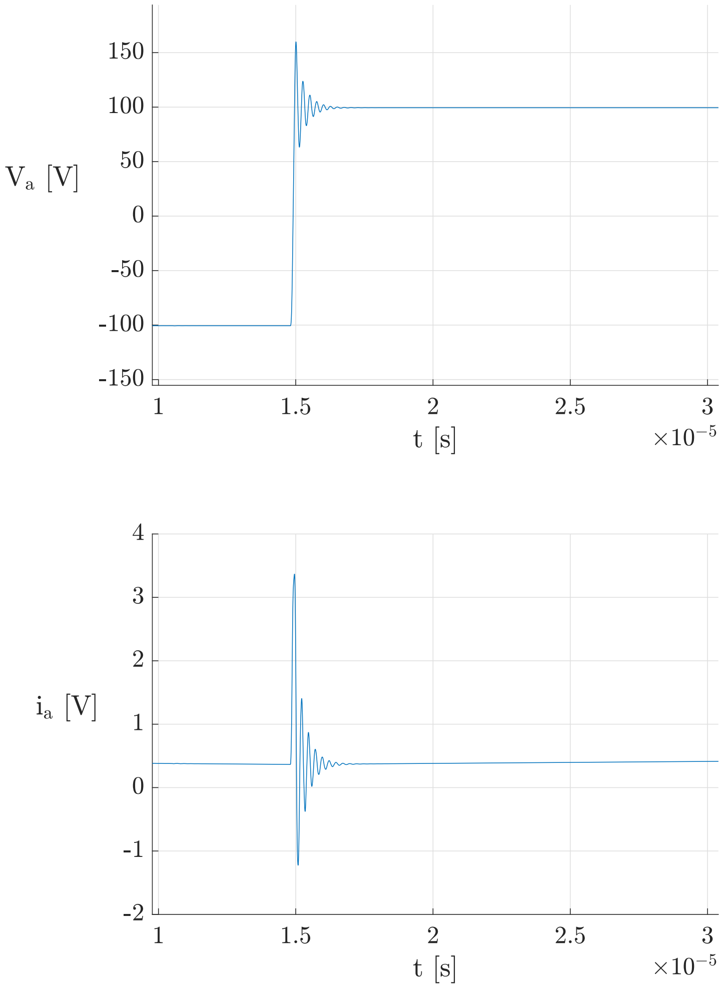

Figure 5.27: Zoom of simulations results close to experimental tests.

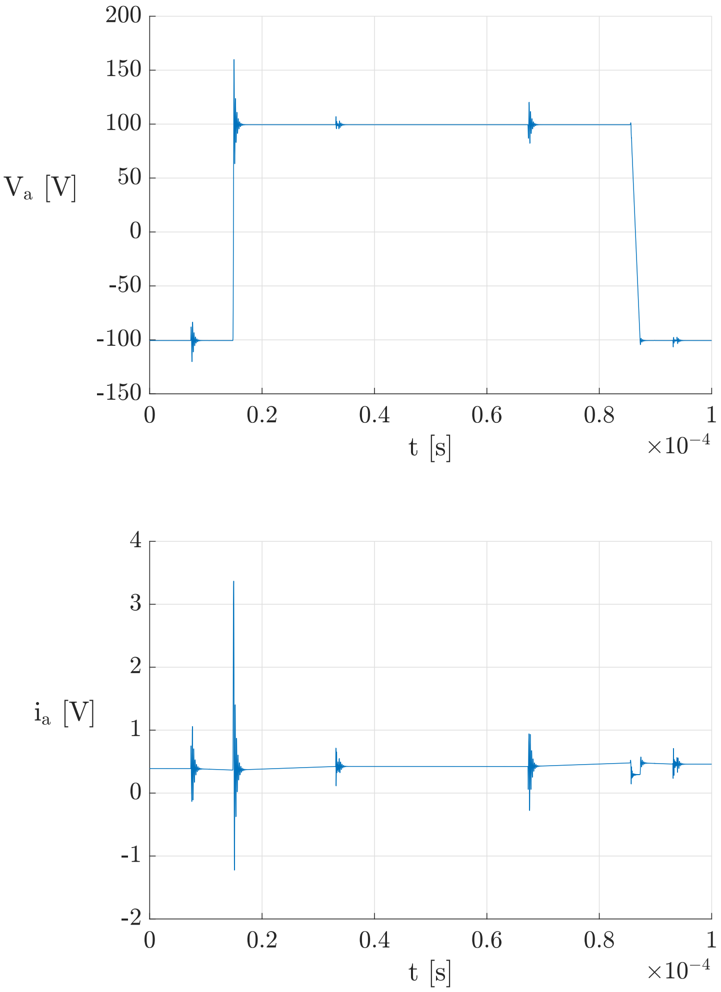

Figure 5.28: Simulations results close to experimental tests.

2 and 4 m cable length, reported in figure 5.23 are similar to the one of the experimental tests with the same lengths, reported in figures 5.6. Figure 5.28 also shows that the turn-off oscillations are much lower than the turn-on ones: this phenomenon is due to the different switching times and parasitic elements of the IGBT and of the diode.

Tables 5.4, 5.5, 5.6 report the parameters values which were used to obtain the final simulations similar to the experimental results.

Table 5.4: Inverter elements

Component	Value	[-]
Q_{rr}	1500	μC
C_{GE}	10.309	nF
C_{GC}	0.215	nF
C_{CE}	0.17	nF
R_G	0.001	Ω
R_C	0.001	Ω
R_E	0.001	Ω

Table 5.5: Cable elements

Component	Value	[-]
C_{p1}	461	pF
C_{p2}	85.2	pF
R_{p1}	79.77	$k\Omega$
R_{p2}	88.46	$k\Omega$
R_{s1}	0.0163	Ω
R_{s2}	0.1456	Ω
L_{s1}	250	nH
L_{s2}	53	nH

Table 5.6: Motor elements

Component	Value	[-]
R_s	0.742	Ω
L_s	21	mH
C_{g1}	1.52	nF
C_{g2}	16.5	pF
R_e	6.47	$k\Omega$
R_{g1}	11.66	Ω
R_{g2}	399	Ω
C_t	7.83	pF
R_t	2.88	$k\Omega$
L_t	504	μF
L_d	487	μF

This work has presented two different position observers based on current oversampling for a SynRM. In the first one were used the current derivatives estimated during the longest vector applied in a SVPWM period, while in the second one were used the current derivatives estimated during two voltage vectors, but it was independent on the electrical resistance.
The distinctive features of this work were the absence of any high-frequency current injection or PWM modification, the use of a recursive least square algorithm on data obtained using standard current sensors and the use of the current oversampling technique for a SynRM. As an implementation hint, all of the three phase currents have been measured, in order to increase the accuracy of the position estimation. The observers feasibility and precision has been proven by simulations and with experimental tests on a laboratory prototype.
In order to reduce the disturbances due to high frequency current oscillations, generated by the IGBTS switching and parasitic elements, the current derivative regression have been delayed of a few μs after the switching instant.
The regression delay has avoided a correct Resistance and Speed Independent Observer position estimation in many working conditions, because it required two voltage vectors to be long enough to allow the high frequency oscillations to decay.
However, the experimental tests has shown that the Longest Vector analysis Observer estimations were very accurate in the whole speed range and also during transients, but some estimation errors were noticed in voltage saturations working conditions.
In the end, high frequency oscillations sources have been identified and their behaviour analysed in detail, finding a correlation between tests carried out with different experimental setups. Moreover, current oscillations waveforms have been correctly reproduced using a *Simscape* model, which parameters were found using a trial-and-error method.
The paper [22], about the Longest Vector analysis based Observer presented in this work, has been accepted for publication at the IET International Conference on Power Electronics, Machines and Drives 2020.

5.4 FUTURE STUDIES

In future studies, the observers performances could be improved, for example developing a high-frequency filter, based on an adaptive frequency tracking technique. This method uses a band-pass filter to extract the frequency component and an algorithm to calculate the amplitude [23]. Moreover, the knowledge of the IGBT switching could be used to determine which current will be the most affected by high frequency oscillations in the next SVPWM period and thus calculating this phase current using the other two phase currents measurements. In this way, the Recursive Least Squares regression delay t_{wait} could be reduced, in order to increase the regression time window and then the observer precision and accuracy. Thanks to this reduction also the RSIO could be used, thus the estimated position could be calculated as a weighted average of LVO and RSIO estimations, depending on the motor's working conditions.

Another future possibility is to develop a closed-loop observer, as a Model Reference Adaptive System, and to consider also the cross-coupling inductances and iron saturation in the observer model, in order to obtain a higher estimation precision. After these improvements, a closed-loop control based on this sensorless technique could be implemented.

The clamp meter and the LEM sensors, used in the first part of this work, have a 100 kHz and a 150kHz (at -1dB) bandwidth, respectively, but further studies could be carried out to investigate if they have a non-linear behaviour. Moreover, the high-frequency model developed in *Matlab Simscape* could be used in the future to develop and test more advanced techniques to reduce the position estimation error due to high frequency oscillations.

APPENDIX

A

MATHEMATICAL STEPS

A.1 FROM 2.34 TO 2.38

We have:

$$e^2 = \sum_{k=1}^{N} (y_k - f(x_k))^2 = \sum_{k=1}^{N} (y_k - \alpha_1 x_k - \alpha_0) \tag{A.1}$$

Imposing the conditions

$$\begin{aligned} \tfrac{\partial e^2}{\partial \alpha_1} &= 0 \\ \tfrac{\partial e^2}{\partial \alpha_0} &= 0 \end{aligned} \tag{A.2}$$

we obtain:

$$\begin{aligned} \tfrac{\partial e^2}{\partial \alpha_1} &= \textstyle\sum_{=1}^{N} -2(y_k - \alpha_1 x_k - \alpha_0) x_k = 0 \\ \tfrac{\partial e^2}{\partial \alpha_0} &= \textstyle\sum_{=1}^{N} -2(y_k - \alpha_1 x_k - \alpha_0) = 0 \end{aligned} \tag{A.3}$$

which can be rewritten in the following way:

$$\begin{aligned} 0 &= \alpha_1 \textstyle\sum_{=1}^{N} x_k^2 + \alpha_0 \sum_{=1}^{N} x_k - \sum_{=1}^{N} y_k x_k \\ 0 &= \alpha_1 \textstyle\sum_{=1}^{N} x_k + \alpha_0 N - \sum_{=1}^{N} y_k \end{aligned} \tag{A.4}$$

In the end we obtain:

$$\alpha_1 = \frac{\sum_{k=1}^{N} (x_k y_k - \overline{xy})}{\sum_{k=1}^{N} (x_k^2 - \bar{x}^2)} \tag{A.5}$$

$$\alpha_0 = \bar{y} - \alpha_1 \bar{x} \tag{A.6}$$

where $\bar{x} = \frac{1}{N} \sum_{=1}^{N} x_k$

Replacing the generic variable y with the current i in the equation 2.29, we can write:

$$i = \alpha_1 \cdot t + \alpha_0 = \frac{di}{dt} \cdot t + i_0 \tag{A.7}$$

and equation 2.30 becomes:

$$i_k = \frac{di_k}{dt} \cdot t + i_{0,k} + e_k \tag{A.8}$$

Therefore, the initial current offset is:

$$\hat{i}_0 = \bar{i} - \frac{\widehat{di}}{dt} \bar{t} \tag{A.9}$$

while the estimated current derivative is

$$
\begin{aligned}
\frac{\hat{di}}{dt} &= \frac{\sum_{k=1}^{N}(t_k i_k - \overline{i\cdot t})}{\sum_{k=1}^{N}(t_k^2 - \bar{t}^2)} && \text{(A.10)}\\
&= \frac{\sum_{k=1}^{N}(t_k i_k) - \sum_{k=1}^{N}(\overline{i\cdot t})}{\sum_{k=1}^{N}(t_k^2) - \sum_{k=1}^{N}(\bar{t}^2)} && \text{(A.11)}\\
&= \frac{\sum_{k=1}^{N}(t_k i_k) - N(\overline{i\cdot t})}{\sum_{k=1}^{N}(t_k^2) - N(\bar{t}^2)} && \text{(A.12)}\\
&= \frac{\frac{1}{N}\sum_{k=1}^{N}(t_k i_k) - \overline{i\cdot t}}{\frac{1}{N}\sum_{k=1}^{N}(t_k^2) - \bar{t}^2} && \text{(A.13)}\\
&= \frac{\overline{i\cdot t} - \bar{i}\cdot\bar{t}}{\overline{t^2} - \bar{t}^{\,2}} && \text{(A.14)}
\end{aligned}
$$

In this way we have obtained the current derivative estimation formula:

$$
\frac{\hat{di}}{dt} = \frac{\overline{i\cdot t} - \bar{i}\cdot\bar{t}}{\overline{t^2} - \bar{t}^{\,2}} \tag{A.15}
$$

A.2 FROM 2.45 TO 2.48

$$
\begin{cases}
u_\alpha = R\,i_\alpha + \dfrac{di_\alpha}{dt}\,(L_\Sigma - L_\Delta\,c) - L_\Delta\,\dfrac{di_\beta}{dt}\,s - 2\,L_\Delta\,c\,i_\beta\,w_{me} + 2\,L_\Delta\,i_\alpha\,s\,w_{me}\\
u_\beta = R\,i_\beta + \dfrac{di_\beta}{dt}\,(L_\Sigma + L_\Delta\,c) - L_\Delta\,\dfrac{di_\alpha}{dt}\,s - 2\,L_\Delta\,c\,i_\alpha\,w_{me} - 2\,L_\Delta\,i_\beta\,s\,w_{me}
\end{cases} \tag{A.16}
$$

$$
\begin{cases}
u_\alpha = R\,i_\alpha + \dfrac{di_\alpha}{dt}\,L_\Sigma - \dfrac{di_\alpha}{dt}L_\Delta\,c - L_\Delta\,\dfrac{di_\beta}{dt}\,s - 2\,L_\Delta\,c\,i_\beta\,w_{me} + 2\,L_\Delta\,i_\alpha\,s\,w_{me}\\
u_\beta = R\,i_\beta + \dfrac{di_\beta}{dt}\,L_\Sigma + \dfrac{di_\beta}{dt}L_\Delta\,c - L_\Delta\,\dfrac{di_\alpha}{dt}\,s - 2\,L_\Delta\,c\,i_\alpha\,w_{me} - 2\,L_\Delta\,i_\beta\,s\,w_{me}
\end{cases} \tag{A.17}
$$

$$
\begin{cases}
(u_\alpha - R\,i_\alpha - \dfrac{di_\alpha}{dt}\,L_\Sigma) = (-\dfrac{di_\alpha}{dt}L_\Delta\, - 2\,L_\Delta\,i_\beta\,w_{me})c + (-L_\Delta\,\dfrac{di_\beta}{dt}\, + 2\,L_\Delta\,i_\alpha\,w_{me})s\\
(u_\beta - R\,i_\beta - \dfrac{di_\beta}{dt}\,L_\Sigma) = (+\dfrac{di_\beta}{dt}L_\Delta\, - 2\,L_\Delta\,i_\alpha\,w_{me})c + (-L_\Delta\,\dfrac{di_\alpha}{dt}2\,L_\Delta\,i_\beta\,w_{me})s
\end{cases} \tag{A.18}
$$

$$
\begin{cases}
A = B\,c + C\,s\\
D = E\,c + F\,s
\end{cases} \tag{A.19}
$$

$$\begin{cases} c = \dfrac{A}{B} - \dfrac{C}{B}s \\ D = E\dfrac{A}{B} - E\dfrac{C}{B}s + F\,s \end{cases} \tag{A.20}$$

$$\begin{cases} c = \dfrac{A}{B} - \dfrac{C}{B}s \\ \dfrac{EC - FB}{B}s = E\dfrac{EA - DB}{B} \end{cases} \tag{A.21}$$

$$\begin{cases} c = \dfrac{A}{B} - \dfrac{C}{B}s \\ s = \dfrac{EA - DB}{EC - FB} \end{cases} \tag{A.22}$$

$$\begin{cases} c = \dfrac{A}{B} - \dfrac{C}{B}\dfrac{EA - DB}{EC - FB} \\ s = \dfrac{EA - DB}{EC - FB} \end{cases} \tag{A.23}$$

$$\begin{cases} c = \dfrac{-FA + DC}{EC - FB} \\ s = \dfrac{EA - DB}{EC - FB} \end{cases} \tag{A.24}$$

$$\hat{\theta}_{me} = \frac{1}{2}\mathrm{atan2}\left(\frac{s}{c}\right) \tag{A.25}$$

$$= \frac{1}{2}\mathrm{atan2}\left(\frac{EA - DB}{-FA + DC}\right) \tag{A.26}$$

$$= \frac{1}{2}\mathrm{atan2}\left(\frac{\hat{\sin}(2\theta_{me})}{\hat{\cos}(2\theta_{me})}\right) \tag{A.27}$$

A.3 FROM 2.51 TO 2.52

$$\boldsymbol{u}_{\alpha\beta,m} - \boldsymbol{u}_{\alpha\beta,m1} = \boldsymbol{L}_{\alpha\beta}(\frac{d\boldsymbol{i}_{\alpha\beta,m}}{dt} - \frac{d\boldsymbol{i}_{\alpha\beta,m1}}{dt}) \tag{A.28}$$

which can be rewritten in a more compact form:

$$\boldsymbol{u}_{\alpha\beta,m-m1} = \boldsymbol{L}_{\alpha\beta}\frac{d\boldsymbol{i}_{\alpha\beta,m-m1}}{dt} \tag{A.29}$$

$$\begin{bmatrix} \boldsymbol{u}_{\alpha,m-m1} \\ \boldsymbol{u}_{\beta,m-m1} \end{bmatrix} = \begin{bmatrix} L_\Sigma - L_\Delta\,c & -L_\Delta\,s \\ -L_\Delta\,s & L_\Sigma + L_\Delta\,c \end{bmatrix} \begin{bmatrix} \frac{d\boldsymbol{i}_{\alpha,m-m1}}{dt} \\ \frac{d\boldsymbol{i}_{\beta,m-m1}}{dt} \end{bmatrix} \tag{A.30}$$

$$\begin{cases} (u_{\alpha,m-m1} - \dfrac{di_{\alpha,m-m1}}{dt}\,L_\Sigma) = (-\dfrac{di_{\alpha,m-m1}}{dt}L_\Delta)c + (-L_\Delta\,\dfrac{di_{\beta,m-m1}}{dt})s \\ (u_{\beta,m-m1} - \dfrac{di_{\beta,m-m1}}{dt}\,L_\Sigma) = (+\dfrac{di_{\beta,m-m1}}{dt}L_\Delta)c + (-L_\Delta\,\dfrac{di_{\alpha,m-m1}}{dt})s \end{cases} \tag{A.31}$$

Then, repeating the same mathematical steps from A.19 to A.24, we obtain:

$$\hat{\theta}_{\text{me}} = \frac{1}{2}\text{atan2}\left(\frac{num}{den}\right) \tag{A.32}$$

where:

$$\begin{aligned} num = {} & \frac{di_{\beta,m-m1}}{dt}\,u_{\alpha,m-m1} + \frac{di_{\alpha,m-m1}}{dt}\,u_{\beta,m-m1} + \\ & - 2\,L_\Sigma\,\frac{di_{\beta,m-m1}}{dt}\,\frac{di_{\alpha,m-m1}}{dt} \end{aligned} \tag{A.33}$$

$$\begin{aligned} den = {} & L_\Sigma\,\frac{di_{\beta,m-m1}}{dt}^2 - u_{\beta,m-m1}\,\frac{di_{\beta,m-m1}}{dt} - L_\Sigma\,\frac{di_{\alpha,m-m1}}{dt}^2 + \\ & + u_{\alpha,m-m1}\,\frac{di_{\alpha,m-m1}}{dt} \end{aligned} \tag{A.34}$$

BIBLIOGRAPHY

[1] M. Zigliotto. *Electrical AC Drives.* Lecture notes for Mechatronichs. Vicenza,Italy, 2018.

[2] F. Tinazzi. *Electrical AC Drives Laboratory.* Lecture notes for Mechatronichs. Vicenza,Italy, 2019.

[3] P. Landsmann. *Sensorless control of synchronous machines by linear approximation of oversampled current.* Ph.D. Thesis. Munich, 2014.

[4] P. Nussbaumer and T. M. Wolbank. "Saliency tracking based sensorless control of AC machines exploiting inverter switching transients". In: (July 2010), pp. 114–119. DOI: 10.1109/SLED.2010.5542793.

[5] P. Nussbaumer and T. M. Wolbank. "Using oversampling techniques to extract ac machine saliency information". In: (Nov. 2010), pp. 1035–1040. DOI: 10.1109/IECON.2010.5675510.

[6] P. Nussbaumer and T. M. Wolbank. "Using switching transients to exploit sensorless control information for electric machines". In: (Sept. 2011), pp. 35–40. DOI: 10.1109/SLED.2011.6051542.

[7] S. Bolognani, S. Calligaro, R. Petrella, and M. Sterpellone. "Sensorless control for IPMSM using PWM excitation: Analytical developments and implementation issues". In: (Sept. 2011), pp. 64–73. DOI: 10.1109/SLED.2011.6051546.

[8] Yu Duan and M. Sumner. "A novel current derivative measurement using recursive least square algorithms for sensorless control of permanent magnet synchronous machine". In: 2 (June 2012), pp. 1193–1200. DOI: 10.1109/IPEMC.2012.6259005.

[9] D. Q. Guan, D. Xiao, and M. F. Rahman. "A new high-bandwidth sensorless direct torque controlled IPM synchronous machine drive using a hybrid sliding mode observer". In: (May 2014), pp. 1–8. DOI: 10.1109/SLED.2014.6844965.

[10] D. Hind, M. Sumner, and C. Gerada. "Use of an artificial neural network for current derivative estimation". In: (Sept. 2013), pp. 1–10. DOI: 10.1109/EPE.2013.6634327.

[11] David Hind. *Current Derivative Estimation for Sensorless Motor Drives.* Ph.D Thesis. Nottingham, 2015.

[12] B. Weber, G. Lindemann, and A. Mertens. "Reduced observer for anisotropy-based position estimation of PM synchronous machines using current oversampling". In: (Sept. 2017), pp. 121–126. DOI: 10.1109/SLED.2017.8078441.

[13] M. Zigliotto. *Fundamentals Of Electrical Machines And Drives.* Lecture notes for Mechatronichs. Vicenza,Italy, 2018.

[14] N. Bianchi. "Synchronous reluctance and interior permanent magnet motors". In: *2013 IEEE Workshop on Electrical Machines Design, Control and Diagnosis (WEMDCD).* Mar. 2013, pp. 75–84. DOI: `10.1109/WEMDCD.2013.6525167`.

[15] R. Antonello, L. Ortombina, F. Tinazzi, and M. Zigliotto. "Online Stator Resistance Tracking for Reluctance and Interior Permanent Magnet Synchronous Motors". In: *IEEE Transactions on Industry Applications* 54.4 (July 2018), pp. 3405–3414. DOI: `10.1109/TIA.2018.2819961`.

[16] dSpace website. *`https://www.dspace.com/en/pub/home/products/hw/microlabbox.cfm`*.

[17] H. Babu. *Test-bench development and post-processing method for the analysis of transient currents in an inverter-fed motor.* Report of the Individual Project Course in Electric Power and Energy Systems. KTH, Stockholm, Sweden, June, 2018.

[18] S. L. Senthil Kumar. *Analysis of transient currents in two different inverter-fed motors.* Report of the Individual Project Course in Electric Power and Energy Systems. KTH, Stockholm, Sweden, June, 2018.

[19] A. E. Ginart, D. W. Brown, P. W. Kalgren, and M. J. Roemer. "Online Ringing Characterization as a Diagnostic Technique for IGBTs in Power Drives". In: *IEEE Transactions on Instrumentation and Measurement* 58.7 (July 2009), pp. 2290–2299. DOI: `10.1109/TIM.2009.2013920`.

[20] N. Mohan, T.M. Undeland, and W. P. Robbins. *Power Electronics.* USA, 2003.

[21] A. Sona. *Interferenze Elettromagnetiche.* Sept., 2018.

[22] M. Giuliato, L. Peretti, F. Tinazzi, and M. Zigliotto. "Sensorless control for a synchronous reluctance motor based on current oversampling using standard PWM excitation". In: (2020).

[23] S. Neusus. *Analysis of algorithms for on-line direct frequency estimation.* Technical Report for ABB Corporate Research. ABB, Vasteras, Sweden, August, 2014.